2008

Prospects of lean ignition with the quarter wave coaxial cavity igniter

Franz Andreas Johannes Pertl
West Virginia University

PROSPECTS OF LEAN IGNITION WITH THE QUARTER WAVE COAXIAL CAVITY IGNITER

Franz Andreas Johannes Pertl

Dissertation submitted to the
College of Engineering and Mineral Resources
at West Virginia University
in partial fulfillment of the requirements
for the degree of

Doctor of Philosophy
in
Mechanical Engineering

James E. Smith, Ph.D., Chair
Gregory J. Thompson, Ph.D.
Roy S. Nutter, Ph.D.
Nigel Clark, Ph.D.
Mary Ann Clarke, Ph.D.

Department of Mechanical and Aerospace Engineering
Morgantown, West Virginia
2008

Keywords: Plasma, RF, Microwave, Ignition, Combustion, Quarter Wave Coaxial Cavity Resonator

ABSTRACT

PROSPECTS OF LEAN IGNITION WITH THE QUARTER WAVE COAXIAL CAVITY IGNITER

Franz Andreas Johannes Pertl

New ignition sources are needed to operate the next generation of lean high efficiency internal combustion engines. A significant environmental and economic benefit could be obtained from these lean engines. Toward this goal, the quarter wave coaxial cavity resonator, QWCCR, igniter was examined. A detailed theoretical analysis of the resonator was performed relating geometric and material parameters to performance characteristics, such as resonator quality factor and developed tip electric field. The analysis provided for the construction and evaluation of a resonator for ignition testing.

The evaluation consisted of ignition tests with liquefied-petroleum-gas (LPG) air mixtures of varying composition. The combustion of these mixtures was contained in a closed steel vessel with a precombustion pressure near one atmosphere. The resonator igniter was fired in this vessel with a nominal 150 W microwave pulse of varying duration, to determine ignition energy limits for various mixtures. The mixture compositions were determined by partial pressure measurement and the ideal gas law. Successful ignition was determined through observation of the combustion through a view port. The pulse and reflected microwave power were captured in real time with a high-speed digital storage oscilloscope. Ignition energies and power levels were calculated from these measurements. As a comparison, these ignition experiments were also carried out with a standard non-resistive spark plug, where gap voltage and current were captured for energy calculations.

The results show that easily ignitable mixtures around stoichiometric and slightly rich compositions are ignitable with the QWCCR using the similar kinds of energies as the conventional spark plug in the low milli-Joule range. Energies for very lean mixtures could not be determined reliably for the QWCCR for this prototype test, but could be lower than that for a conventional spark. Given the capability of high power, high energy delivery, and opportunity for optimization, the QWCCR has the potential to deliver more energy per unit time than a conventional spark plug and thus should be considered be as a lean ignition source.

ACKNOWLEDGEMENTS

The author wishes to thank the members of my committee: Dr. Nigel Clark, Dr. Mary Ann Clarke, Dr. Roy Nutter, Dr. James Smith and Dr. Gregory Thompson for their assistance, encouragement and critical comments.

I thank Dr. Smith for his support in providing the necessary laboratory space, equipment and environment to conduct this research, for his encouragement and for his unwavering confidence and support.

I thank the department of Mechanical and Aerospace Engineering staff for their assistance and support, especially, Chuck Coleman, Linda Cox, Cliff Judy, Jean Kopasko, Marilyn Host and Debora Willis.

I thank the WVU Engine and Emissions Research Center staff, Wayne Hildebrand and Richard Atkinson for letting me borrows various components, calibrators and for their advice.

In general I also thank all the CIRA graduate and undergraduate students, especially Jon Kweder, Pat Wildfire and Jay Wilhelm for their assistance and support with moving and assembling hardware.

Lastly, I thank my wife Emily for her support, understanding and patience, as well as for taking on more than her share of the day-to-day little things, which allowed me to focus my studies and research.

TABLE OF CONTENTS

LIST OF FIGURES

LIST OF TABLES

NOMENCLATURE

μ	Magnetic permeability of medium
a	QWCCR center conductor radius
AC	Alternating current
b	QWCCR outer conductor radius
B_r	Shunt radiation susceptance of flanged coaxial cable aperture
D	Electron diffusion coefficient
DC	Direct current
E	Electric field intensity phasor
E(x)	Complete elliptical integral of the second kind
E_0	Electric field strength
E_a	Electric field at radius *a* on surface of QWCCR tip
E_b	Root mean square electric field breakdown threshold
ECR	Electron cyclotron resonance
E_{eff}	Frequency compensated effective electric field
E_{rms}	Root mean square electric field
$\overline{far}$	Molar fuel air ratio
G_r	Shunt radiation conductance of flanged coaxial cable aperture
H	Magnetic field intensity phasor
$\mathbf{H}_{//}$	Component of magnetic field intensity parallel to surface
I_0	Assumed peak RF current
IC	Internal combustion
I_s	Sparkplug spark current
ISM	Industrial scientific medical
J	Surface current phasor
l	Electron mean free path
m	Electron mass
M	Particle mass >> *m*
n_e	Electron population
n_{e0}	Initial electron population
p	Absolute pressure
p^*	Temperature adjusted equivalent pressure
P_{air}	Absolute pressure of air in combustion vessel prior to mixing with fuel

P_b	Power dissipated in QWCCR base conductor
P_{ctr}	Power dissipated by QWCCR center conductor
P_L	Dissipated power, load power
P_{mix}	Absolute pressure of air fuel mixture in combustion vessel prior to ignition
P_{out}	Power dissipated by QWCCR outer conductor
P_{rad}	Power dissipated as radiation
$p_{\sigma e}$	Dielectric volume power density
Q	Quality factor
Q_b	Q of QWCCR base conductor
Q_{ctr}	Q of QWCCR center conductor
Q_{int}	Q of QWCCR interior
Q_{out}	Q of QWCCR outer conductor
QWCCR	Quarter wave coaxial cavity resonator
$Q_{\Gamma=0}$	Loaded Q of QWCCR with 0 reflected power, perfect coupling, or 1:1 SWR
$Q_{\sigma e}$	Q of QWCCR dielectric
r	Radial distance from QWCCR center
RF	Radio frequency
R_s	Conductor surface resistance
s	Complex frequency-domain or s-plane variable
SI	Spark ignited
T	Absolute temperature
T_{air}	Absolute temperature of air in combustion vessel prior to mixing with fuel
$\tan(\delta_e)$	Dielectric medium loss tangent
TEM	Transverse electromagnetic
T_{mix}	Absolute temperature of air fuel mixture in combustion vessel prior to ignition
U	Stored energy
U_a	Energy absorbed by an electron between collisions
U_m	Time average stored magnetic energy
U_{rad}	Energy stored in radiative near field
U_s	Sparkplug spark energy
V_{ab}	Potential difference between QWCCR outer and inner conductor
V_i	Gas ionization potential
V_o	Assumed peak RF electric potential
V_s	Sparkplug spark potential

X_s	Conductor surface reactance
Y_0	Characteristic conductance of a coaxial cable
z	Distance along the axis of the QWCCR from the base
Z_s	Conductor surface impedance
α	Real part of propagation constant, attenuation constant
β	Imaginary part of electromagnetic propagation constant, phase constant
Γ	Voltage reflection coefficient
ε	Electric permittivity of medium
ε'	Real part of dielectric complex permittivity
ε''	Imaginary part of dielectric complex permittivity
$\boldsymbol{\varepsilon_c}$	Dielectric complex permittivity
ζ	Damping coefficient of a second order system
η	Intrinsic impedance of medium
λ	Electromagnetic wavelength
Λ	Characteristic diffusion length
μ_c	Conductor magnetic permeability
ν_a	Electron loss attachment frequency
$\boldsymbol{\nu_c}$	Effective momentum collision frequency of the electrons and neutral particles
ν_i	Electron production ionization frequency
σ_c	Conductor conductivity
σ_e	Dielectric medium effective conductivity
ω	Angular frequency
ω_n	Angular natural frequency of a second order system
τ_p	Ignition pulse duration
U_{qw}	Energy of microwave pulse accepted by QWCCR
P_{pls}	Microwave pulse power as measured by spectrum analyzer
P_{ref}	Microwave pulse power reflected by QWCCR

CHAPTER 1: Introduction

1.1 Motivation

Since the invention of the modern internal combustion (IC) engine over a hundred years ago, two basic methods have been used to ignite the combustion mixtures. Auto ignition of the air-fuel mixture through compression, as in the Diesel engine as invented by Rudolf Diesel in 1892, and spark ignition as is used in four stroke Otto-Cycle engines, as first developed by Nikolaus Otto in 1876. Today a very large number of spark ignited (SI) engines are in use, consuming the planet's limited fossil fuel energy supply. A significant environmental and economic benefit could be obtained if these engines could be made more efficient. Higher thermal efficiencies for SI engines could be obtained through operation with leaner fuel air mixtures and through operations at higher power densities and pressures (Dale 1997). Unfortunately, experience has shown that as fuel-air mixtures are leaned or as cylinder pressure is increased, these mixtures become more difficult to ignite. More energetic sparks can be used to ignite these mixtures, however, their overall ignition energy efficiency is reduced, and more energetic sparks with larger surfaces are required for reliable ignition (Maly et al. 1983). These higher energy levels are detrimental to the spark plug lifetime, especially to the electrodes, and may also contribute to the formation of undesirable pollutants. Alternatives to the traditional ignition spark could open the door to more efficient, leaner and cleaner combustion resulting in associated economic and environmental benefits.

Such alternative ignition systems include unconventional electrical discharges as opposed to a direct current (DC) spark. These discharges form various plasmas. Research into plasma assisted ignition and combustion includes a frequency range from DC sparks to laser light. The various methods and devices each have their own peculiarities and complexities. For example, laser ignition requires optical transparency of the combustion chamber and complicated laser equipment (Starikovskaia 2006).

One particularly simple plasma device is the quarter wave coaxial cavity resonator (QWCCR). This device has been studied by researchers at the West Virginia University's Mechanical and Aerospace Engineering Department for a number of years (Nash 1988, Bonazza 1992, Stiles 1997, McIntyre 2000). The QWCCR consists of a quarter wavelength resonant coaxial cavity into which electromagnetic energy is

coupled resulting in a standing electromagnetic field. This large field induces a break-down to occur in the gaseous medium surrounding the center electrode, creating a plasma discharge that has been demonstrated to have potential as an ignition source (McIntyre 2000). Theoretical analysis of the QWCCR in the context of transmission line theory was performed by Nash, but experimental performance data has not been fully explained by this analysis.

1.2 Objective

The objective of this work is to investigate the microwave QWCCR as an ignition source relative to a conventional DC spark plug and to determine if the quarter wave coaxial cavity resonator can ignite a leaner fuel-air mixture than a conventional spark plug given a similar amount of input energy. A secondary objective is to clarify the influences of geometry and materials on the design of a QWCCR. This will be accomplished through a theoretical analysis with emphasis on electrical efficiency, as represented by the quality factor of the QWCCR device, and the peak electric field generated.

1.3 Approach

For experimental purposes, a coaxial cavity resonator, which can consistently produce microwave discharge, needed to be designed and constructed. The design phase of this work examined, in detail, the quality factor, *Q*, of the coaxial cavity resonator through analysis using radio frequency (RF) cavity methods. The quality factor is a measure of a resonator's electrical efficiency and can also be related to the generated peak microwave electric field.

A microwave coaxial cavity igniter was constructed out of brass; the quality factor was measured on a microwave network analyzer, and the igniter was coupled to a suitable microwave amplifier with associated power and control circuitry to generate a microwave pulse of the desired frequency and power.

Following the design and construction, testing in a combustion bomb was performed, using a standard spark plug as a reference. The performance of the coaxial resonator for igniting lean charges will be evaluated by varying the fuel-air mixture to determine the lean ignition threshold for a given amount of input energy.

CHAPTER 2: **Literature Review**

2.1 Scope

There are numerous alternative ignition systems, including multiple spark plugs per cylinder systems, rail-plug igniters and corona spark plugs (Dale 1997). Most of these systems use plasma of one type or another. The conventional spark, as described in detail by Maly (Maly 1984), is essentially a plasma. There are numerous ignition methods that can be classified as plasma ignition systems. Some examples that have been investigated by various researchers include: laser plasma ignition (McMillian 2004), pulsed nanosecond discharges (Pancheshnyi 2005), dielectric barrier discharges (Anikin 2003), radio frequency (RF) (Chintala 2006) and microwave discharges (Berezhetskaya 2005, Leonov 2006). There is a great variety of plasmas, often categorized by their temperature and electron density as shown in Fig. 1.

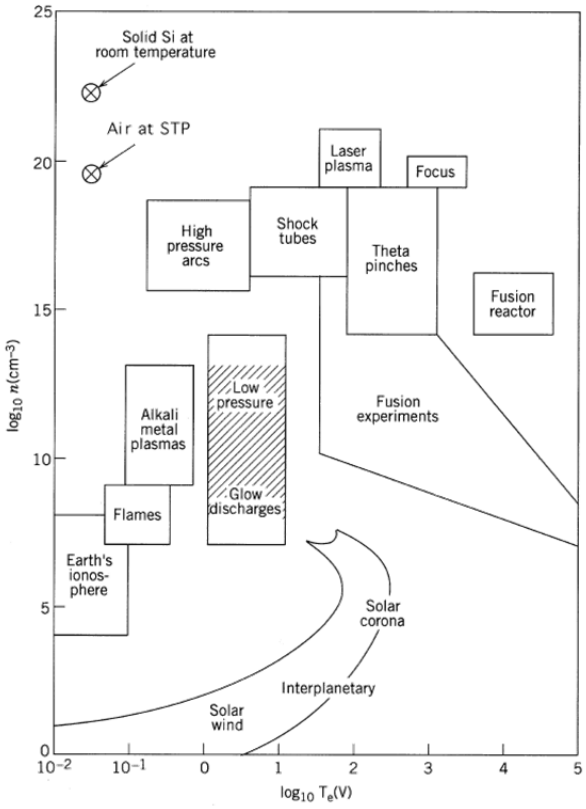

Fig. 1 Illustration of plasma variety (Lieberman 2005)

Since operation of the QWCCR occurs at frequencies in the GHz (10^9 Hz) range, and at atmospheric or above pressures, the plasma generated by it is considered a high pressure microwave plasma similar to the plasmas of high pressure arcs, shock tubes and laser plasmas. This literature review will therefore place emphasis specifically on high pressure microwave induced plasmas, the conventional DC spark and the prior work concerned specifically with the QWCCR. A broader scope of plasma assisted ignition which considers other types of plasma can be found in a recent review paper (Starikovskaia 2006).

2.2 History of the QWCCR Igniter

The QWCCR was studied by Nash as an RF power processing element under the guidance of Dr. James Corum and Dr. James Smith at West Virginia University's College of Engineering (Nash 1988). In his thesis, Nash analyzed the resonator using a transmission line analogy and presented a lumped series resonant circuit model, the parameters of which were not worked out in detail, or in terms of the geometric variables. His work was focused on RF power processing by building up a high voltage, oscillating, charge reservoir and not on combustion ignition. Using 200 W of power, an RF plasma was produced by Nash with two 0.75m tall, 100 MHz cavities. His expression for the cavity quality factor, Q, given in (1), is the well known expression for the Q of a resonant quarter wave section of transmission line, where $\alpha + j\beta$ is the complex electromagnetic propagation constant.

$$Q = \frac{\beta}{2 \cdot \alpha} \tag{1}$$

In his conclusions Nash states that prediction of the performance measures based on his analysis are not entirely in agreement with experimental results, even for such key values as the cavity quality factor, and the resonant frequency.

In 1992, the QWCCR was proposed as an ignition source for internal combustion engines in two Society of Automotive Engineers (SAE) technical publications (Bonazza 1992, VanVoorhies 1992). Bonazza proposes that an implementation of the QWCCR replacing a spark plug would have to operate at about 2 GHz and be capable of ignition at pressures up to 10 bar. He speculated that an increase in ignition volume over the traditional DC spark would result in an advantage for igniting leaner fuel-air mixtures. VanVoorhies performed a theoretical rough-order-of-magnitude analysis of the QWCCR discharge at 2

GHz. His analysis indicated the formation of thermal plasma through electron impacts on a stationary gas ion background and the electrode, and that no plasma resonance effects would take place. His analysis was based on an assumed maximum electric field strength of 30 kV/cm attained by the resonator, which is sufficient for DC breakdown of air at 1 atm, and that an electron density of 10^{23} m^{-3} (Baretto 1979) is sufficient to cause ignition. VanVoorhies' analysis identifies a delay time on the order of 10 ns for imparting sufficient energy to the electrons undergoing multiple collisions to induce breakdown. He concluded that experimental verification of the ignition characteristics of the QWCCR was needed.

By 1998, experimental devices had been constructed in the 440 and 900 MHz ranges (Stiles 1997, 1998). In this work, the operation of the cavities in a vessel pressurized up to nearly 7 atmospheres was confirmed at a power level near 150 W. Experimental cavities whose center electrode consisted of a thermocouple showed electrode tip temperatures in excess of 900°C capable of vaporizing Teflon™ for sustained discharges. Stiles' experiments indicate a slight drop in electrode tip temperature with increasing pressure. Numerical modeling using the finite difference time domain method and experimental measurements confirmed a strong electromagnetic field concentration about the QWCCR's center electrode tip. For input power levels of 1 mW, field strengths near 40 V/m were measured at approximately 3 mm from the center electrode tip of a prototype plasma igniter mounted in a Briggs and Stratton engine cylinder. Stiles also reported modulation of the RF signal at kHz frequencies (10^3 Hz) resulting in plasmas with modulation frequency in the audible range.

Continuation of these experiments by McIntyre's thesis work led to consecutive ignition events in a Briggs and Stratton engine cylinder by a Teflon™ filled coaxial cavity igniter, while the engine was motored by a dynamometer (McIntyre 2000). The microwave power levels used were approximately 100 W at frequencies in the 900 MHz range. Unfortunately, the Teflon™ filling used to keep the harsh combustion gases out of the resonator did not survive past a few ignitions.

To address this shortcoming of the igniter, Lowery investigated several alternate dielectric filling materials and their effects on quality factor and efficiency through experimentation and numerical simulation. Lowery's results show significant degradation of the quality factor by filling the cavity with a 98% pure alumina powder mix that could withstand the harsh in-cylinder conditions (Lowery 2006).

Although apparently disconnected from the research performed at West Virginia University, 2.45 GHz QWCCRs were constructed and pressure tested in Germany (Von Hagen 2001, Linkenheil 2004). Their results confirmed formation of plasma at various pressures up to 6 atmospheres with power levels of 30 to 300 W. The data shows a trend requiring an increase in power with an increase in pressure.

While considerable progress has been made in the experimental construction and testing of QWCCR, very little theoretical work has been performed since Nash's transmission line analysis. Also, an experimental study of how the QWCCR performs as an igniter of a combustible mixture, such as in comparison to a spark plug, has not been performed.

2.3 Traditional DC Spark Ignition

The modern spark plug first appeared in the late 1800s. Various people could be credited with its invention, including Tesla, Simms, Bosch and Benz. Little has changed in the basic design of the spark plug since that time. Its modern configuration, as it is used in IC engines today, is shown in Fig. 2.

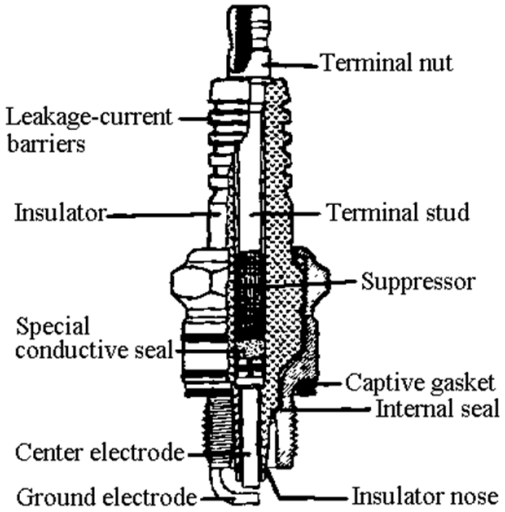

Fig. 2 Sketch of spark plug anatomy (Heywood 1988)

The basic operation consists of applying a voltage spike, generated by an electric circuit (eg. ignition coil circuit), to the plug which, if breakdown conditions are met, causes a spark to form in the spark gap. This spark, provided it has enough energy, will then ignite the combustible mixture in an engine cylinder. However, the exact sequence of events and the mechanism which leads to a propagating flame front are

highly complex, and depend on many parameters that are still topics of active research. The necessary condition for breakdown of dry air at one atmosphere is often quoted to be an electric field strength of 30kV/cm. The well-known Paschen Law is often used to determine gas breakdown voltages at different pressures, however in high pressure breakdowns, the formation of initial streamers and a corona often occur at voltages before the breakdown voltage is reached. Under these conditions, the Paschen Law is not strictly obeyed (Roth 1995). Classic experimental data on spark ignition energies of several hydrocarbon fuels are shown in Fig. 3 - 6 (Mullins and Penner 1959, Heywood 1988, Bone and Townend 1927). These illustrate that the minimum spark ignition energy required to ignite a mixture is dependent on many factors. One factor is the mixture composition. When lean or rich, substantially more energy is required for ignition, as shown in Fig. 3. Similarly, ignition is dependent on the mixture pressure. There even exists a minimum pressure below which ignition seems to not occur. Fig. 4 illustrates such a minimum pressure for the ignition of a particular methane-air mixture by a very large spark energy of 8640 mJ. Fig. 5 shows that the minimum required spark ignition energy also depends on the mixture flow velocity. Ignition characteristics are also affected by temperature. There exists a temperature above which a fuel-air mixture will spontaneously ignite. This is known as the autoignition temperature and is the basis of compression ignition, as opposed to spark ignition. The autoignition temperature is generally related to the molecular complexity of the fuel (molecular degrees of freedom). The autoignition temperature for various hydrocarbon fuels is shown in Fig. 6. Minimum igniting currents in a particular induction coil's primary circuit are shown in Fig. 7 for various gaseous hydrocarbons including propane. All these various characteristics underscore the complex nature of combustion ignition.

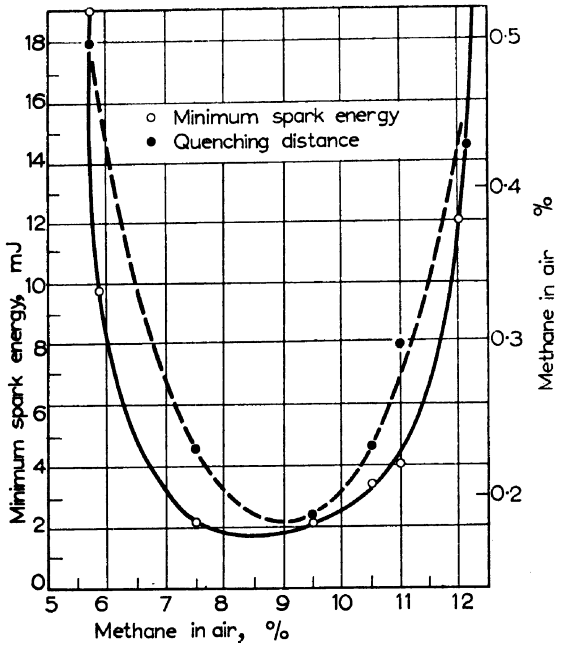

Fig. 3 Minimum energy at 1/3 bar (Lewis and von Elbe 1948)

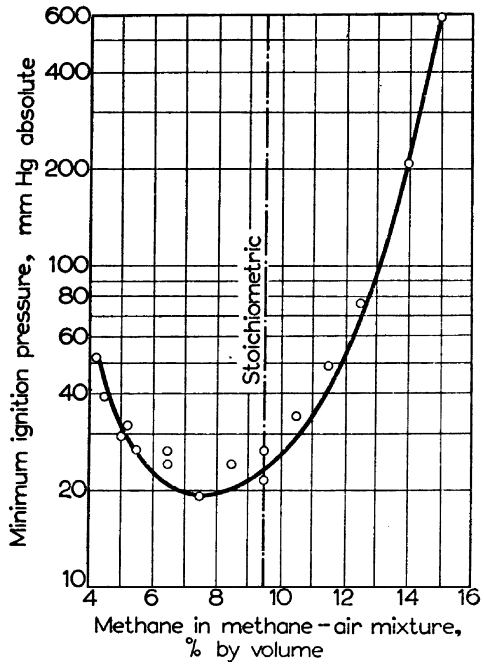

Fig. 4 Minimum pressure with 8640 mJ of energy (Lankin et al. 1948)

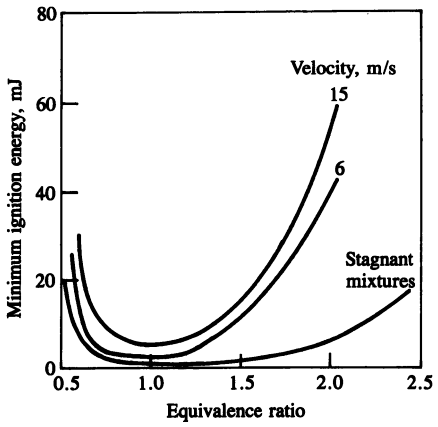

Fig. 5 Minimum energy of propane at 0.17 bar (Ballal et al. 1974)

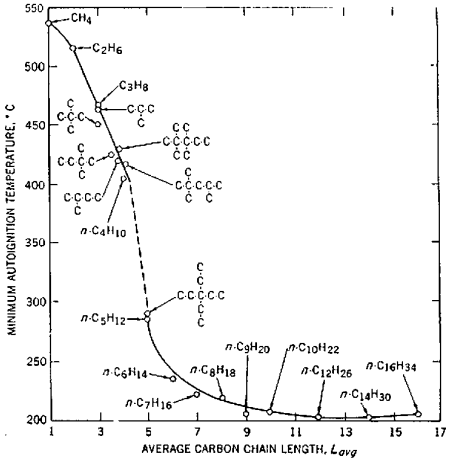

Fig. 6 Autoignition temperatures of hydrocarbons (Coward and Jones 1952)

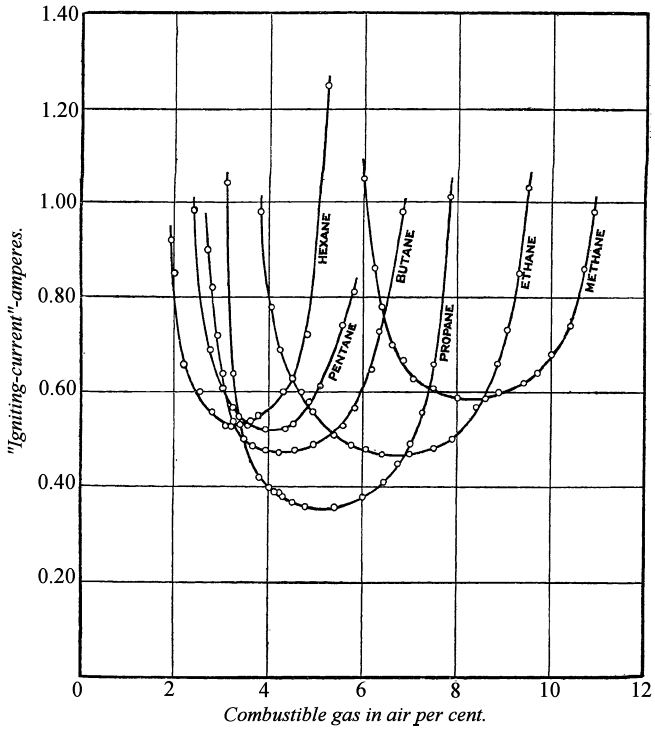

Fig. 7 Least igniting currents of paraffin hydrocarbon-air mixtures
(Bone and Townend 1927)

2.3.1 Details of a DC Spark Discharge

A very informative overview of the spark discharge ignition process is given by Heywood (1988), a portion of which is summarized below. This overview mainly refers to work done by Maly (Maly 1976, 1983, 1984). Fig. 8 shows typical voltage and current waveforms of a conventional spark ignition system which delivers roughly 30 - 50 mJ of energy to the spark. Just 0.25 mJ of energy is required to ignite a quiescent, stoichiometric fuel-air mixture (Wolf 1972). However, leaner or richer mixtures at high or low pressures may require an order of magnitude more energy. Generally, the ignition energy of a spark can be broken into three phases: (1) a breakdown phase with about 1 mJ, (2) an arc phase with about 1 mJ and (3) a glow phase with about 30 mJ, based on the voltage and current waveforms of a typical ignition spark. Fig.7 illustrates these waveforms, that when multiplied with each other give spark power as a function of time. Integration of the power will give the spark's ignition energy.

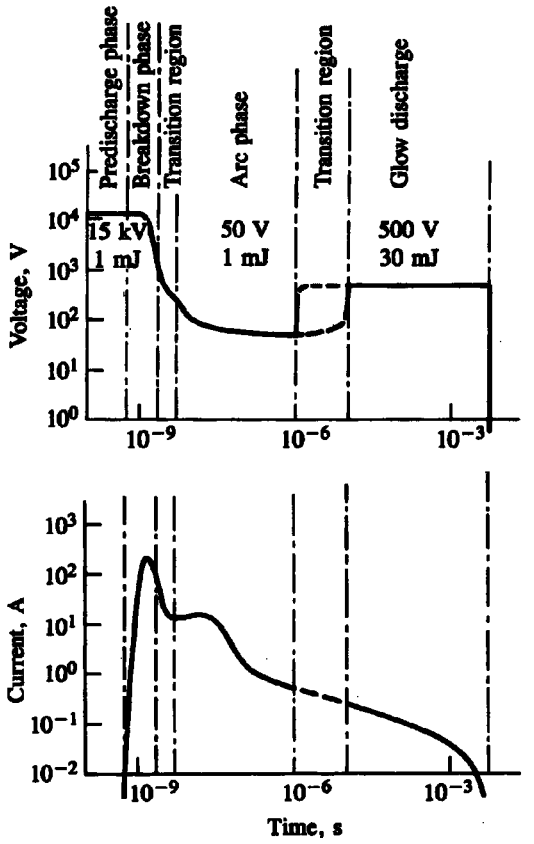

Fig. 8 Voltage and current variations of conventional coil spark ignition (Maly 1976).

2.3.2 The Breakdown phase

During the breakdown phase, streamers form between the electrodes. As the gaseous mixture undergoes electrical breakdown, ionization and dissociation occur because of the high electric field. This field is created by the applied voltage (~10 - 30 kV). This ionization then causes the electrical impedance of the gap to fall rapidly. An explosive pressure shockwave (~100 bar), which will later expand to a plasma kernel of about 2 mm, uses nearly 30% of the energy in this phase. The duration of this breakdown phase is extremely short, on the order of 1 ns. During this brief time, the created free charges establish a thin (~40 μm) cylindrical plasma channel which subsequently conducts a large current (~200 A) between the electrodes. High power densities (~1 MW) and particle temperatures (60,000 K for electrons, Starikovskaia 2006) exist in this initial plasma channel. During the end of the breakdown phase, hot spots develop on the cathode (from heavy ion impacts) turning the discharge into an arc. These hot spots consist of molten pools of metal capable of providing thermally generated electrons for arc formation. These pools are postulated to

be significant contributors to electrode erosion (Soldera 2004), although more recent work has shown that electrode erosion is more likely caused by blasting through oxidation layers to establish a DC conduction path (Rager 2006). Electrode heating and radiation losses consume about 6% of the ignition energy, while about 94% of the energy is delivered to the gas mixture, making this brief phase highly efficient.

2.3.3 The Arc Phase

The arc phase is the conduction phase of the spark. It lasts for about 1 microsecond, during which the established plasma channel allows large currents to flow. The degree of gas ionization decreases rapidly. At the boundary of the plasma channel it may drop to 1% or lower. However, reactive radicals remain as a store of chemical energy. The conduction channel temperature drops to near 6000 K, and the total energy loss is almost 50%. Most of this loss can be attributed to heat conducted away by the electrodes.

2.3.4 The Glow Phase

As mass diffusion and expansion take place, the spark enters the glow phase with temperatures near 3000 K. The power levels drop to approximately 10 W with currents on the order of 100 mA. Most of the energy delivered to a spark is consumed in this phase. The long duration of this phase (~1 ms) is responsible for this, despite the low power levels. Up to 70% of this energy in this phase goes toward heating the electrodes. In order to obtain more ignition energy, the duration or energy level of the spark can be increased, but this will lead to a less efficient energy transfer to the gas and to more severe electrode erosion.

The onset of chemical reactions can be detected spectroscopically a few nanoseconds after spark initiation, but the core spark plasma temperatures are much too large for normal combustion products to exist, so combustion reactions primarily occur on the outer surface of the plasma. The energy stored in the radicals formed in the kernel is later released to the unreacted mixture through molecular collisions of species by diffusion out of the kernel. After about 10 μs the temperature of the plasma surface has fallen to conventional flame temperatures and combustion reactions can occur. After about 20 μs of expansion, the reactions must be self-sustaining and overcome heat loss by diffusion and conduction.

Note that the minimum energy required to ignite a premixed fuel-air mixture is highly dependant on the properties of the mixture, such as composition, pressure and velocity. The leaner a mixture becomes, the

slower a flame front will propagate. Therefore, to overcome heat losses, a larger initial inflamed volume with more energy is required to successfully start combustion.

Mixture flow velocity (~1 - 10 m/s in engines) is another critical ignition parameter. In mixtures with higher velocity, energy is spread over a larger volume, but heat losses to the electrodes are reduced. So, the required ignition energy may be higher or lower, depending on the specifics of the ignition system. Maly gives the following summary of the fundamental aspects of spark ignitions (Maly 1984):

- *"Of the total electrical energy supplied to the spark, only that fraction contained within the outer surface layer of the plasma is available for initiating the flame propagation process. The energy density and the temperature gradient in this layer depend on the discharge mode. Highest energy densities and temperature gradients are achieved if the ignition energy is supplied in the shortest time interval."*
- *"A minimum radius of the spark plasma is required for inflammation of fuel-air mixture to occur. This radius increases rapidly as the mixture is leaned out; it decreases with increasing pressure and increasing plasma expansion velocity."*
- *"After inflammation, burning rates are proportional to flame surface area. Thus discharges and plasma geometries that produce the largest inflammation zone surfaces, most rapidly, are advantageous."*
- *"The time over which the ignition energy can be used effectively for inflammation decreases as the initial flame velocity increases. Ignition energy supplied after inflammation has occurred will have only modest impact on flame propagation."*

From the above, it is apparent that ignition by a spark is a highly complex process, with dependence on spark time profiles, spark energy, spark plasma temperature, electrode configurations and combustion mixture properties.

2.4 High Pressure Microwave Breakdown and Ignition

In contrast to a DC spark, the QWCCR creates microwave plasma by inducing electrical breakdown of a gas mixture surrounding the tip of the center electrode using a microwave electric field. The microwave electric field strength required to induce breakdown is therefore a key ignition parameter. Previous analysis of the discharge of the QWCCR has assumed an atmospheric air breakdown potential of 30 kV/cm from DC breakdown theory (Van Voorhies 1992). Since the microwave breakdown process of a gas is different from DC breakdown, this assumed breakdown field strength may not necessarily be appropriate.

Microwave breakdown of gas mixtures for ignition purposes has only recently been considered and is not as well studied as DC spark ignition. Ignition systems using microwaves are sparse in the literature, and each system is uniquely different. For example, one system focuses a microwave beam pulse onto a target containing metallic particles which in turn emit photons and sparks initiating combustion (Berezhetskaya 2005). Initiation of combustion with extremely short electrical pulses has been studied (Wang 2005). Note that while such short pulses may have frequency components in the microwave range, they cannot be considered to be a microwave pulse, and as such are closer to a DC corona type discharge.

A 13.4 MHz, 500 W RF discharge was used to ignite a gas mixture flowing at Mach 0.8 and at a relatively low pressure of ~100 torr (Chintala 2005). This research was looking toward applications for jet engine ignition at high altitudes. While advantages with respect to leaner ignition were found, this type of ignition does not use microwaves at atmospheric or high pressures. Others have observed 30% combustion flame speed enhancements under the influence of kW range 2.45 GHz microwaves (Zaidi 2006), but field strengths were below breakdown strength and ignition was not performed by the microwaves. As very little literature exists on microwave ignition, particularly of the atmospheric to high pressure type, an overview of high pressure microwave breakdown will be presented.

2.4.1 Characteristics of Microwave Plasmas

The following summary of microwave plasma characteristics is adapted from Roth (Roth 1995). Microwave generated plasmas generally are more energetic (5 - 15 eV electron temperature) than DC and RF generated plasmas (1 - 2 eV electron temperatures). Unmagnetized, atmospheric pressure microwave plasmas can provide higher ionization and dissociation than DC or RF discharges due to their higher electron kinetic energy.

2.4.2 Microwave Breakdown in Gases

Gas electron dynamics govern the behavior of microwave frequency breakdowns. Factors that play key roles in this process are the initial free electron population, electron diffusion, drift, electron attachment and recombination (Woo 1970). The initial electron population, created by cosmic rays, photo ionization, radioactivity or other mechanisms, is required to seed the exponential increase in electrons during the breakdown process. Unfortunately, this initial population is usually unknown, but according to MacDonald,

the nature of the exponential breakdown is not very different for wide ranges of initial population densities (MacDonald 1963).

During ionization, collisions of sufficiently energetic electrons with neutral particles or ions free additional electrons. For example, electron energies required for ionization of N_2 and O_2 particles are 15.6 eV and 12.1 eV, respectively. Additional free electrons can also be generated through electron impacts on solids, such as container walls or electrodes. This process is known as "multipacting" and in a uniform field is favored by lower pressures where electrons can impact on the surface of the solids before being deflected through collisions with other gas particles (Woo 1970).

Diffusion is an electron loss mechanism by which electron concentration gradients are reduced. This process is pressure dependent. At high pressures, electrons encounter many obstacles in their path which inhibit their ability to diffuse, so attachment is often considered the dominant loss mechanism at higher pressures where plasmas are mainly collisional (Tomala 2005).

The electron loss by attachment occurs when an electron becomes joined with a neutral particle to form an ion. The reactions involved with this process may involve other particles as well. Attachment can easily create ions such as O_2^- with minimal energy input as shown by reactions (2) and (3).

$$e^- + O_2 + 3.6\text{eV} \rightarrow O_2^+ \text{, and} \tag{2}$$

$$e^- + O_2 + M \rightarrow O_2^+ + M \text{ .} \tag{3}$$

The second lower energy reaction will be favored in weaker electric fields. A pressure increase will make the attachment effect more prevalent as particles come closer together (Quiles 2005). Many additional plasma induced reactions are possible and can be found in the literature (Wightman 1974).

Recombination occurs when an electron is captured by an ion, neutralizing the ion. This can lead to the dissociation of molecules, multi-atomic ions, and photon emissions. Recombination becomes relevant when significant concentration of ions and electrons are present, such as already established discharges, so the influence on the initial breakdown is limited (Quiles 2005).

The fact that an electron has to absorb energy from an alternating electric field can be compensated for by defining an effective electric field, E_{eff} , that is approximately frequency independent. The compensation removes the phase lag effects of the applied frequency, ω, from the rms field E_{rms}, according to

$$E_{eff}^2 = E_{rms}^2 \frac{\nu_c^2}{\omega^2 + \nu_c^2}, \tag{4}$$

where ν_c is the effective momentum collision frequency of the electrons and neutral particles. An AC-field, E_{rms}, transfers the same energy to an electron as a stead field of magnitude E_{eff}, provided that the interactions are dominated by collisions (many collisions per AC-cycle) (Brown 1950). This effective field can be used to relate well known DC breakdown voltages for various gases to AC breakdown values for uniform fields. A good approximation for air is $\nu_c \approx 5 \cdot 10^9 \, p$, where p is the pressure in torr (MacDonald, 1966). At atmospheric pressures of 760 torr and above, excitations below 3,000 GHz will fall in the collision dominated domain. This justifies the well known approximation to the rms breakdown threshold, E_b, in V/cm of a uniform microwave field in the collisonal regime given in (5):

$$E_b \approx 30 \cdot p, \tag{5}$$

where the pressure p has units of torr and is a representation of particle density. An increase in gas temperature at constant pressure will lower the breakdown voltage. This can be taken into account by substituting $p^*(T)$ for p, as given in (6), where T is the temperature in K (Anderson 1987, Tomala 2005), or

$$p^* = \frac{298}{T} \cdot p. \tag{6}$$

2.4.3 Linear Breakdown Relationship

Considering high pressure breakdown in more detail, the microwave breakdown field can be expressed as a function of the free space wavelength, λ, the ionization potential of the gas, V_i, the electron mean free path, l, and the characteristic diffusion length, Λ. The mean free path of the electrons in a neutral gas is inversely proportional to the gas pressure, p, (actually number density) and the ionization potential is approximately constant. This leads to the usual variables found in microwave breakdown literature: $E\lambda$, E/p, and λ/Λ.

If electrons are lost with an attachment frequency, ν_a, and produced with an ionization frequency, ν_i, the continuity equation for the electron population, n_e, can be written as follows using Fick's Law of diffusion with an electron diffusion coefficient, D:

$$\frac{\partial n_e}{\partial t} = n_e \cdot \left(\nu_i - \nu_a\right) + D \cdot \nabla^2 n_e \text{ or} \tag{7}$$

$$\frac{1}{n_e}\frac{\partial n_e}{\partial t} - \left(\nu_i - \nu_a\right) = \frac{D \cdot \nabla^2 n_e}{n_e} = -\frac{D}{\Lambda^2}, \tag{8}$$

where appropriate values for air can be found in Woo (Woo 1984). This equation can be solved through separation of variables assuming the time derivative term is independent of spatial position and the attachment and ionization frequencies are independent of time or,

$$\nabla^2 n_e + \frac{n_e}{\Lambda^2} = 0. \tag{9}$$

Substituting yields

$$\frac{\partial n_e}{\partial t} = n_e \cdot \left(\nu_i - \nu_a - \frac{D}{\Lambda^2}\right), \tag{10}$$

which for steady state becomes

$$\left(\nu_i - \nu_a\right) = \frac{D}{\Lambda^2}, \tag{11}$$

or during the breakdown process when n_e is a function of time the solution then becomes

$$n_e = n_{e0} \cdot e^{\left(\nu_i - \nu_a - \frac{D}{\Lambda^2}\right) \cdot t}. \tag{12}$$

Exponential breakdown will occur if the argument of the exponent is positive and an initial population, n_{e0}, of electrons exists, so the condition for breakdown can be expressed as

$$\nu_i - \nu_a = \frac{D}{\Lambda^2}. \tag{13}$$

In the high pressure case, the collision frequency, ν_c, is much greater than the electromagnetic driving frequency, ω, so an electron will lose its kinetic energy in the direction of the forcing electric field in one collision. In order to generate additional electrons through ionization of the background gas, sufficient energy between collisions must be absorbed. The energy, U_a, absorbed by a single electron between collisions is given by

$$U_a = \frac{e^2 \cdot E_{rms}^2}{2 \cdot m \cdot \nu_c^2} \left(\frac{\nu_c^2}{\nu_c^2 - \omega^2} \right), \tag{14}$$

which reduces in the high pressure case to

$$U_a \approx \frac{e^2 \cdot E_{rms}^2}{2 \cdot m \cdot \nu_c^2}. \tag{15}$$

Due to the large mass difference between electrons and the background gas particles, energy transfer between them is very inefficient. The fraction of ionization energy transferred through collision by an electron of mass, m, to a much heavier particle of mass, M, is given by (McDaniel 1964):

$$U_c = \frac{2 \cdot m \cdot M \cdot e \cdot V_i}{(m + M)^2} \approx \frac{2 \cdot m \cdot e \cdot V_i}{M}. \tag{16}$$

In order to obtain a steady discharge, the electron must obtain at least this energy from the electric field between collisions in order to cause ionization, or

$$U_a \approx \frac{e^2 \cdot E_b^2}{2 \cdot m \cdot \nu_c^2} = \frac{2 \cdot m \cdot e \cdot V_i}{M} \approx U_c. \tag{17}$$

The solution for the rms breakdown electric field strength value, E_b, is

$$E_b = 2 \cdot m \cdot \nu_c \cdot \sqrt{\frac{V_i}{e \cdot M}} \approx C_1 \cdot p. \tag{18}$$

Since the collision frequency, ν_c, is directly proportional to the number density of the gas, the high pressure microwave breakdown voltage is a linear function of pressure for most gases. The energy not applied toward ionization goes into raising the temperature of the electrons and eventually the temperature of quasi stationary heavy gas ions and neutral particles. A typical microwave discharge has ion and background gas temperatures significantly below electron temperatures due to the large mass difference, but for high pressures, interaction between particle species leading to equilibrium will be stronger, as particles are in closer proximity.

For low pressures (<0.001 bar), the relationship reverses, and the breakdown voltage becomes inversely proportional to pressure (Roth 1995). Experimental data on the microwave breakdown of various gases is given in the literature (MacDonald 1966, and MacDonald & Tetenbaum 1978).

Note that some loss mechanisms have been neglected, but the argument suffices to justify the linear dependence of the breakdown field on pressure. It is interesting to note that once a gas has broken down, and a discharge has formed, the electron diffusion losses become even smaller due to electrostatic confinement. This reduces the electric field required to sustain the discharge as compared to the breakdown field by a factor of 3-4 for hydrogen (Brown 1966).

The introduction of a steady state magnetic field can also be used to reduce the electric field required for breakdown in the vicinity of the magnetic field dependant electron gyro-frequency. This is often employed in electron cyclotron resonant (ECR) microwave plasmas. The required magnetic field to establish electrons resonance at 2.45 GHz is only 87.5 mTesla. This concept could be applied to the QWCCR to reduce the breakdown field strengths and improve microwave energy transfer to the gas through spiral resonance of the free electrons in the magnetic field.

2.4.4 Relevance to Plasma Ignition

Given the above, air in an engine cylinder with a compression ratio of about 10 will have a number density 10 times greater than at atmospheric conditions and should therefore undergo microwave breakdown due to a uniform microwave field of field strengths of approximately 300 kV/cm. This is very similar to the DC field strength established in a conventional spark plug gap. However, the microwave field created by the QWCCR at the tip is not a uniform field, and therefore the ionization rate is a function of position. This can lead to rapid local heating lowering the breakdown field strength (Platzman 1960). A discharge formed in this manner will establish itself based on a balance between thermal losses and absorbed microwave power (Anderson 1987). The microwave power absorbed depends on the non-uniform electron density of the discharge and the non-uniform microwave field. Given this rapid local heating, the thermally induced lowering of the breakdown conditions and the initial deposit of energy into chemically reactive species (ions and radicals), this type of plasma may prove to have advantages over a traditional DC spark with respect to ignition of leaner mixtures. Also, since the formation of the microwave discharge does not require a plasma channel to blast a conduction path through any previously established oxide layer, erosion of the electrodes may be significantly reduced, paving the way to higher ignition

energies and higher pressure mixtures. Typical electrode erosion rates for spark plugs are on the order of 1-10 cubic microns per spark (Rager 2006).

2.4.5 Summary

According to the surveyed literature, the QWCCR has been studied for some time, but a rigorous analysis allowing geometric design, general performance prediction and experimental work verifying its ignition characteristics are not available. The review of microwave gas breakdown indicates that discharges should be formed at field strengths comparable to conventional sparks at atmospheric and higher pressures. For reference, a brief review of conventional spark ignition and ignition energy was also presented.

CHAPTER 3: Design and Experimental Approach

3.1 Design of a high performance resonator

A theoretical analysis of the coaxial resonator's quality factor is now presented to obtain engineering relationships for the resonator's performance. This theoretical analysis will clarify the important design variables of the resonator and extend the work performed by Nash (1988). Previous analysis of the resonator quality factor, Q, was based on the propagation constant where $\alpha + j\beta$, of a wave transmission line section is given in (1). This neglects the losses in the ends of the resonator, namely the conduction losses in the closed base, and the radiation losses of the open end and does not provide the needed insight for design. The following analysis begins with describing a standing quarter wave electromagnetic field inside the resonator. This standing wave oscillates at a resonant frequency, ω, contains a stored energy, U, and dissipates a power, P_L. The coaxial geometry used for the analysis of the resonator is given in Fig. 9. The relationships of interest are how the geometry and the material properties relate to the quality factor, the input power and the maximum electromagnetic field developed.

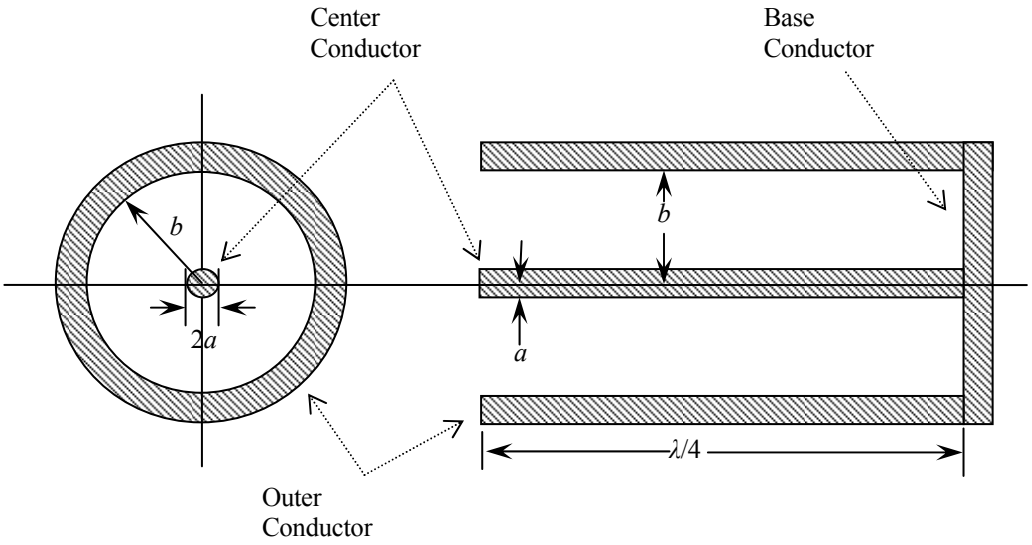

Fig. 9 Basic QWCCR coaxial structure

3.2 Electromagnetic Field in the QWCCR

The fields at the lowest ¼ wave resonance in the cavity are transverse electromagnetic (TEM) fields as they exist inside coaxial cables. The magnetic field is purely circumferential and falls off inversely with the radius, r, from the center. The electric field is purely radial and also falls off inversely with the radius. The magnetic field intensity phasor, $\mathbf{H}$, and the electric field phasor, $\mathbf{E}$, of the standing quarter wave inside the resonator can therefore be expressed as

$$\vec{\mathbf{H}} = H_\phi \cdot \hat{a}_\phi = \frac{I_0}{2 \cdot \pi \cdot r} \cdot \cos(\beta \cdot z) \cdot \hat{a}_\phi , \tag{19}$$

$$\text{and } \vec{\mathbf{E}} = E_r \cdot \hat{a}_r = \frac{V_0}{2 \cdot \pi \cdot r} \cdot \sin(\beta \cdot z) \cdot \hat{a}_r . \tag{20}$$

I_0 is the peak current at the base of the cavity, V_o is the magnitude of peak potential, r is the radial distance from the center, z is the axial distance from the base taken positive toward the open end of the cavity and $\beta = 2\pi/\lambda$ is the wavenumber or phase constant.

3.3 The Quality Factor, Relation to Tip Electric Field, Energy Storage and Losses.

By definition, the quality factor, Q, is given by

$$Q = \frac{\omega \cdot U}{P_L} , \tag{21}$$

where ω is the angular frequency, U is the time average energy and P_L is the time average power lost. Note that after an extremely brief initial cavity ringup (see 3.3.3), P_L is also the power delivered to the QWCCR as the fields will build up until the losses equal the power delivered to the device. What follows will show that the square of V_0 is directly proportional to the energy stored, so (21) will give a relation for the developed tip potential and electric field through

$$U = \frac{Q \cdot P_L}{\omega} \propto V_0^2 . \tag{22}$$

At resonance, the total energy is traded back and forth between the electric field and the magnetic field. The time average magnetic energy (or half of the peak energy) stored in the cavity volume, U_m, is given by integrating the magnetic field volume energy density resulting in

$$U_m = \tfrac{1}{4}\mu \cdot \int_{vol} \left|\vec{\mathbf{H}}\right|^2 \cdot dV \text{ , or} \tag{23}$$

$$U_m = \tfrac{1}{4}\mu \cdot \frac{I_0^2}{(2\cdot\pi)^2} \int_0^{z_0} \int_a^b \int_0^{2\pi} \frac{\cos^2(\beta\cdot z)}{r^2} \cdot r d\phi \cdot dr \cdot dz \text{ , and} \tag{24}$$

$$U_m = \tfrac{1}{4}\frac{\mu\cdot I_0^2 \cdot \ln\left(\frac{b}{a}\right)}{2\cdot\pi}\left[\frac{-z_0\cdot\sin(2\cdot\beta\cdot z)}{2\cdot\pi} + \frac{z}{2}\right]_{z=0}^{z=\frac{\lambda}{4}} = \frac{\mu\cdot I_0^2\cdot\ln\left(\frac{b}{a}\right)\cdot\lambda/4}{16\cdot\pi}, \tag{25}$$

where μ is the magnetic permeability.

The time average electric energy stored is given by integrating the electric field volume energy density resulting in

$$U_e = \tfrac{1}{4}\varepsilon \cdot \int_{vol} \left|\vec{\mathbf{E}}\right|^2 \cdot dV = \frac{\varepsilon\cdot V_0^2\cdot\ln\left(\frac{b}{a}\right)\cdot\lambda/4}{16\cdot\pi}, \tag{26}$$

where ε is the electric permittivity.

The total time average stored energy at resonance, U, is then given by

$$U = U_m + U_e = 2\cdot U_m = 2\cdot U_e = \frac{\mu\cdot I_0^2\cdot\ln\left(\frac{b}{a}\right)\cdot\lambda}{32\cdot\pi} = \frac{\varepsilon\cdot V_0^2\cdot\ln\left(\frac{b}{a}\right)\cdot\lambda}{32\cdot\pi} \quad . \tag{27}$$

This shows that the electric and magnetic field amplitudes, I_0 and V_0, are related by η, the intrinsic impedance of the space in the cavity as is expected for TEM waves. The relation is given by

$$\eta = \sqrt{\frac{\mu}{\varepsilon}} = \frac{V_0}{I_0}. \tag{28}$$

Substitution of equation (27) into (21) gives an approximate relation for the center conductor peak tip potential, V_0, as

$$V_0 = \sqrt{\frac{32\cdot\pi\cdot Q\cdot P_L}{\omega\cdot\varepsilon\cdot\ln(\frac{b}{a})\cdot\lambda}} = 4\sqrt{\frac{\eta\cdot Q\cdot P_L}{\ln\left(\frac{b}{a}\right)}}. \tag{29}$$

The corresponding peak value of the electric field at radius a, E_a, given by (20) is then

$$E_a = \frac{V_0}{2\cdot\pi\cdot a}. \tag{30}$$

The root mean square of this electric field will have to exceed the breakdown strength given by (18). It is clear from (30) that to increase the field strength, a should be made as small as is practical. A lower

dielectric constant, ε, more input power, P_L, and a higher Q will also increase the field strength, but only in the square root. Since Q is a function of the geometry, it will be examined in more detail. Towards this, the power losses in the cavity need to be examined.

3.3.1 Conductor and Dielectric Losses

The time-averaged power loss is composed of ohmic losses on the conductor surfaces, losses to any dielectric occupying the cavity volume, and losses to radiation from the open cavity end. The ohmic losses depend on the surface impedances, Z_s, of the conductors. For good conductors this impedance can be approximated by the complex quantity

$$Z_s = R_s + j \cdot X_s \approx (1+j) \cdot \sqrt{\frac{\omega \cdot \mu_c}{2 \cdot \sigma_c}} \quad , \tag{31}$$

where μ_c and σ_c are the magnetic permeability of the conductor and the conductivity of the conductor respectively. The time-averaged surface power density can be found from the surface current density, $\mathbf{J}$, and is given by

$$\tfrac{1}{2} R_s \cdot \vec{\mathbf{J}} \cdot \vec{\mathbf{J}}^* = \tfrac{1}{2} R_s \cdot \left|\vec{\mathbf{J}}\right|^2 = \tfrac{1}{2} R_s \cdot \left|\vec{\mathbf{H}}_{//}\right|^2 . \tag{32}$$

The surface current density is equal to $\mathbf{H}_{//}$, the local magnetic field intensity parallel to the surface. The ohmic losses for the center conductor, P_{ctr}, can then be computed by integrating the time-averaged power density over its surface, and is given by

$$P_{ctr} = \tfrac{1}{2} R_s \cdot \int_A \left|\vec{\mathbf{H}}_{//}\right|^2 \cdot dA = \tfrac{1}{2} R_s \cdot \int_0^{\frac{\lambda}{4}} 2 \cdot \pi \cdot a \cdot \frac{I_0^2 \cdot \cos^2(\beta \cdot z)}{(2 \cdot \pi \cdot a)^2} \cdot dz \text{ or} \tag{33}$$

$$P_{ctr} = \tfrac{1}{2} \frac{R_s \cdot I_0^2}{2 \cdot \pi \cdot a} \cdot \left[\frac{-z_0 \cdot \sin(2 \cdot \beta \cdot z)}{2 \cdot \pi} + \frac{z}{2} \right]_{z=0}^{z=\frac{\lambda}{4}} = \frac{R_s \cdot I_0^2 \cdot \lambda}{32 \cdot \pi \cdot a} . \tag{34}$$

Similarly, moving out to radius, b, the time-averaged power dissipated by the outer conductor, P_{out}, is given by

$$P_{out} = \frac{R_s \cdot I_0^2 \cdot \lambda}{32 \cdot \pi \cdot b} . \tag{35}$$

The time-averaged power dissipated in the base, P_b, is given by integration over the surface of the base, where the magnetic field intensity is a maximum. It is given by

$$P_b = \tfrac{1}{2} R_s \cdot \int_A \left|\vec{\mathbf{H}}_{//}\right|^2 \cdot dA = \tfrac{1}{2} R_s \cdot \int_a^b \int_0^{2\pi} \frac{I_0^2 \cdot \cos^2(\beta \cdot z)\big|_{z=0}}{(2 \cdot \pi \cdot r)^2} \cdot r d\phi \cdot dr \text{ or} \tag{36}$$

$$P_b = \frac{R_s \cdot I_0^2 \cdot \ln\left(\frac{b}{a}\right)}{4 \cdot \pi}. \tag{37}$$

Interaction of matter with the electromagnetic fields can be very complicated, anisotropic, plus frequency and temperature dependent. By assuming a simple isotropic dielectric medium fills the cavity, then the interaction can be characterized reasonably well through its dielectric permittivity, ε, and its effective loss tangent, $\tan(\delta_e)$. The effective loss tangent represents any conductivity and any alternating molecular dipole losses and can be used to calculate an effective conductivity, σ_e, for the dielectric. Alternatively, a simple lossy dielectric can be modeled as having a complex permittivity, ε_c. These material parameters are usually frequency dependant (Balanis 1989). More complicated models sometimes treat the alternating molecular dipoles as mass spring systems driven by the alternating electric field, and anisotropic media can be represented through a permittivity tensor (Balanis 1989). However, the simple relations for a dielectric are

$$\varepsilon_c = \varepsilon' - j \cdot \varepsilon'', \tag{38}$$

$$\tan(\delta_e) = \frac{\varepsilon''}{\varepsilon'}, \tag{39}$$

$$\text{and } \sigma_e = \omega \cdot \varepsilon'' = \omega \cdot \varepsilon' \cdot \tan(\delta_e). \tag{40}$$

If a low loss dielectric is assumed ($\varepsilon'' \ll \varepsilon'$) then

$$\sigma_e \approx \omega \cdot \varepsilon \cdot \tan(\delta_e), \tag{41}$$

The time-averaged power density dissipated due to an alternating electric field in such a simple low loss dielectric medium can then be expressed as

$$p_{\sigma_e} = \tfrac{1}{2} \cdot \sigma_e \cdot \vec{\mathbf{E}} \cdot \vec{\mathbf{E}}^* = \tfrac{1}{2} \cdot \sigma_e \cdot \left|\vec{\mathbf{E}}\right|^2. \tag{42}$$

Integrating over the volume of the dielectric filling the cavity, the power absorbed by the dielectric, $P_{\sigma e}$ is

$$P_{\sigma_e} = \tfrac{1}{2} \sigma_e \cdot \int_{vol} \left|\vec{\mathbf{E}}\right|^2 \cdot dV \text{ or} \tag{43}$$

$$P_{\sigma_e} = \frac{\sigma_e \cdot V_0^2 \cdot \ln\left(\frac{b}{a}\right) \cdot \lambda}{32 \cdot \pi} = \frac{\sigma_e \cdot \eta^2 \cdot I_0^2 \cdot \ln\left(\frac{b}{a}\right) \cdot \lambda}{32 \cdot \pi}. \tag{44}$$

At this point, the distribution of power or losses in the cavity can be compared by examining Q_{ctr}, Q_{out}, Q_b and $Q_{\sigma e}$, the quality factor of the dielectric, the center, the outer, and the base conductors, respectively. The equations are

$$Q_{ctr} = \frac{\omega \cdot U}{P_{ctr}} = \left(\frac{2 \cdot \pi \cdot \eta}{R_s}\right) \cdot \frac{a}{\lambda} \cdot \ln\left(\frac{b}{a}\right), \tag{45}$$

$$Q_{out} = \frac{\omega \cdot U}{P_{out}} = \left(\frac{2 \cdot \pi \cdot \eta}{R_s}\right) \cdot \frac{b}{\lambda} \cdot \ln\left(\frac{b}{a}\right), \tag{46}$$

$$Q_b = \frac{\omega \cdot U}{P_b} = \left(\frac{2 \cdot \pi \cdot \eta}{R_s}\right) \cdot \frac{1}{8}, \tag{47}$$

$$\text{and } Q_{\sigma_e} = \frac{\omega \cdot U}{P_{\sigma_e}} = \tan\left(\delta_e\right), \tag{48}$$

where the wave velocity relation, $1/\sqrt{\mu \cdot \varepsilon} = \lambda \cdot f$ has been used to express ω in terms of λ. An internal quality factor, Q_{int} of the cavity, without considering radiation can then be defined as

$$Q_{int} = \left(Q_{ctr}^{-1} + Q_{out}^{-1} + Q_b^{-1} + Q_{\sigma_e}^{-1}\right)^{-1} = \left(\frac{R_s}{2 \cdot \pi \cdot \eta}\left[\frac{\left(\frac{b}{a}+1\right)}{\frac{b}{\lambda} \cdot \ln\left(\frac{b}{a}\right)} + 8\right] + \tan\left(\delta_e\right)\right)^{-1}. \tag{49}$$

Differentiating with respect to b/a, and setting the result equal to zero results in the ratio of b/a=3.59. This is the same ratio that can be found in the literature for a half-wave cavity (Henry 1959). By examining these components of Q, it becomes apparent that the outer conductor's Q is always b/a times greater than that of the center conductor for equal conductivities. The use of a higher conductivity for the small amount of metal comprising the center conductor is an option to increase its Q. It can also be seen that the dielectric and base Q's are not affected by the geometry terms b/a or b/λ.

Up to this point in the analysis, for a maximum Q, b/a should equal 3.59 and b/λ should be as large as feasible. The upper limit for b is set by the appearance of higher resonance modes somewhere around 2π $(b + a) = \lambda$. Any dielectric should have a minimum loss tangent and a low dielectric constant, and surface

resistance should be kept as small as feasible. Contour plots of the loaded quality factor, $Q_{\Gamma=0}$, for brass at 2.45 GHz and copper at 915 MHz , as given by (49), are shown below in Fig. 10 and Fig. 13 for perfect coupling. Note that $Q_{\Gamma=0}$ is $Q/2$. The corresponding tip electric fields are given in Fig. 11 and Fig. 13 respectively, on a per square-root of power basis. However, the rather significant radiation losses, due to increased aperture size, have been omitted so far.

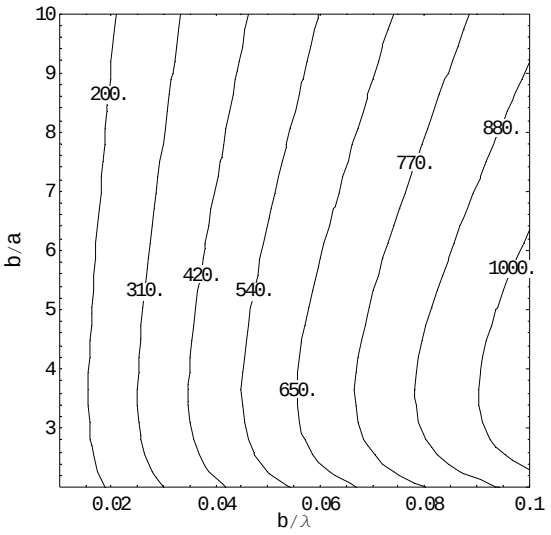

Fig. 10 Contour plot of Q/2 as for Bass, at 2.45 GHz, as given by (49), neglecting radiation, and no dielectric

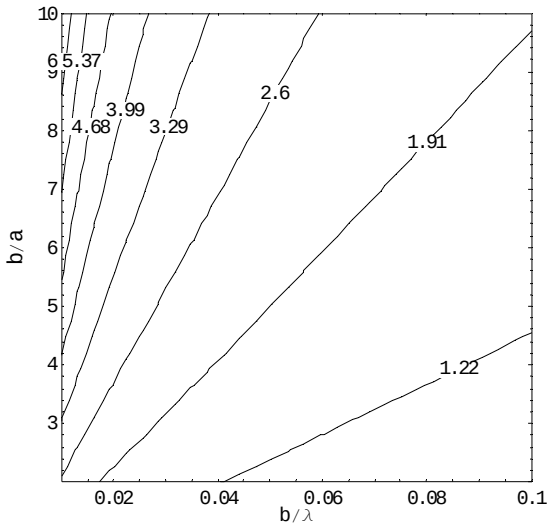

Fig. 11 Contour plot of E_a in (kV cm^{-1} W$^{-1/2}$) for Bass at 2.45 GHz, as given by (30), no radiation and no dielectric

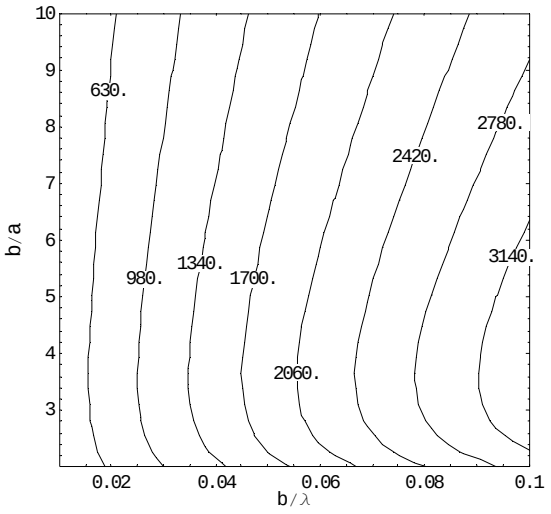

Fig. 12 Contour plot of *Q/2* for Copper at 915 MHz as given by (49), neglecting radiation and no dielectric

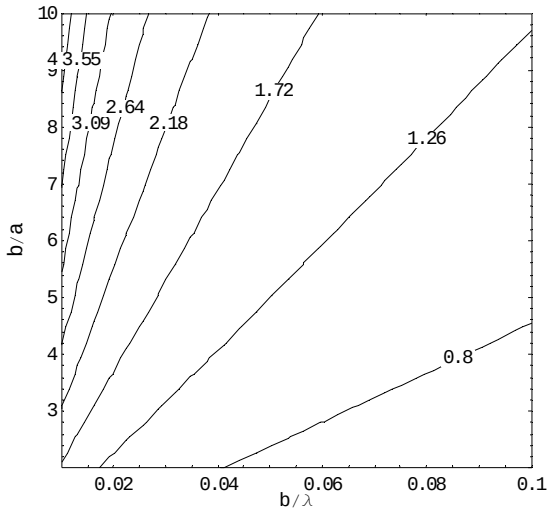

Fig. 13 Contour plot of E_a in (kV cm^{-1} W$^{-1/2}$) for Copper at 915 MHz, as given by (30), no radiation and no dielectric

3.3.2 Radiation Losses

The radiation losses from the QWCCR can be thought of in terms of the aperture admittance of a coaxial line radiating into open space. Equations for this admittance, and an approximation to it, are available in the literature (Marcuvitz 1951). Given the coaxial characteristic conductance, $Y_{0,}$ the full expressions for the aperture shunt conductance, G_r, and susceptance, B_r, can be approximated for a and b much less than λ as

$$G_r \approx \frac{2 \cdot Y_0}{3 \cdot \ln\left(\frac{b}{a}\right)} \cdot \left[\frac{\pi^2 \cdot \left(a^2 - b^2\right)}{\lambda^2}\right]^2 = \frac{4 \cdot \pi^5 \cdot \left[\left(\frac{b/\lambda}{b/a}\right)^2 - \left(\frac{b}{\lambda}\right)^2\right]^2}{3 \cdot \eta \cdot \ln^2\left(\frac{b}{a}\right)}, \tag{50}$$

$$\text{and } B_r \approx \frac{8 \cdot Y_0 \cdot (a+b)}{\lambda \cdot \ln\left(\frac{b}{a}\right)} \cdot \left[\mathrm{E}\left(\frac{2\sqrt{ab}}{a+b}\right) - 1\right] = \frac{16 \cdot \pi \cdot \left(\frac{b/\lambda}{b/a} - \frac{b}{\lambda}\right)}{\eta \cdot \ln^2\left(\frac{b}{a}\right)} \cdot \left[\mathrm{E}\left(\frac{2\sqrt{\frac{b}{a}}}{1+\frac{b}{a}}\right) - 1\right], \tag{51}$$

where $\mathrm{E}(x) = \int_0^{\frac{\pi}{2}} \sqrt{1 - x^2 \cdot \sin^2(\theta)} \cdot d\theta$ is the complete elliptical integral of the second kind. In order to incorporate this into the previous analysis, the potential difference across this shunt admittance, V_{ab}, is needed. The line integral of the electric field from the center to the outer conductor will give this potential difference as

$$V_{ab}\big|_{\beta \cdot z = \pi/4} = \int_{a \to b} E_r \cdot dr = \int_a^b \frac{V_0}{2 \cdot \pi \cdot r} \cdot dr = \frac{V_0 \cdot \ln\left(\frac{b}{a}\right)}{2 \cdot \pi}. \tag{52}$$

The time average power going to radiation, P_{rad}, and the time average energy stored by the susceptance, U_{rad}, are then

$$P_{rad} = \frac{1}{2} G_r \cdot V_{ab}^2 = \frac{V_0^2 \cdot \pi^3 \cdot \left(\frac{b}{\lambda}\right)^4 \cdot \left[\left(\frac{b}{a}\right)^2 - 1\right]^2}{6 \cdot \eta \cdot \left(\frac{b}{a}\right)^4}, \tag{53}$$

$$\text{and } U_{rad} = \frac{1}{4} \cdot \frac{B_r}{\omega} \cdot V_{ab}^2 = \frac{\varepsilon \cdot V_0^2 \cdot \lambda \cdot \left(\frac{b}{\lambda}\right) \cdot \left(\left(\frac{b}{a}\right)^{-1} + 1\right)}{2 \cdot \pi^2} \cdot \left[E\left(\frac{2\sqrt{\frac{b}{a}}}{1+\frac{b}{a}}\right) - 1\right]. \tag{54}$$

Finally, the overall Q of the cavity including radiation can be expressed as

$$Q = \frac{\omega \cdot \left(U + U_{rad}\right)}{P_{ctr} + P_{out} + P_b + P_{\sigma_e} + P_{rad}} \approx \frac{\omega \cdot \left(U\right)}{P_{ctr} + P_{out} + P_b + P_{\sigma_e} + P_{rad}} \,. \tag{55}$$

If the energy stored in the radiation susceptance, U_{rad}, is small compared to the energy stored in the interior of the cavity, U, is small, P_{rad}, can be treated just as another loss mechanism. Fig. 14 is a plot of the ratio of these stored energies, $U_{rad}/\,U$, with respect to the geometry terms b/a and b/λ. This figure shows that the stored energy in the external near field is minimal, compared to the storage inside the cavity, especially for small b/λ, which are necessary for TEM fields.

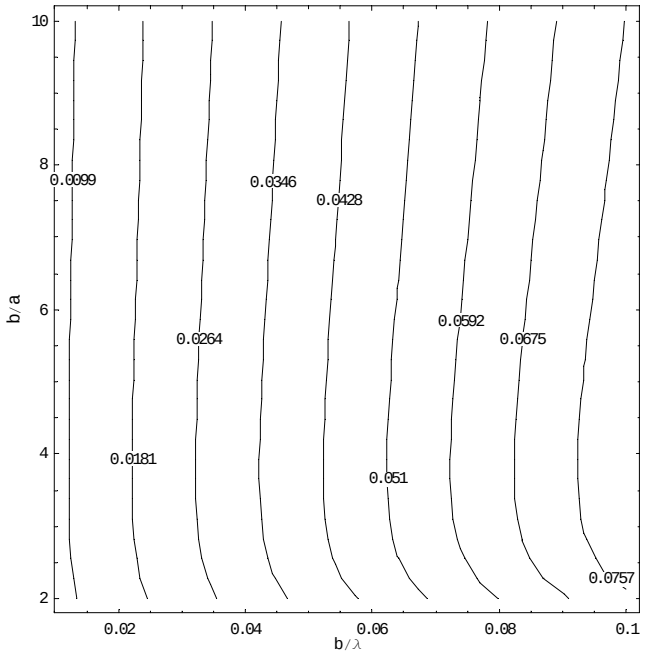

Fig. 14 Contour plot of the ratio of internal to external stored energy, $U_{rad}/\,U$ as given by (54) and (27).

A radiation component, Q_{rad}, of the cavity quality factor can then be defined as

$$Q_{rad} = \frac{\omega \cdot U}{P_{rad}} = \frac{3 \cdot \left(\frac{b}{a}\right)^4 \cdot \ln\left(\frac{b}{a}\right)}{8 \cdot \pi^3 \cdot \left(\frac{b}{\lambda}\right)^4 \cdot \left[\left(\frac{b}{a}\right)^2 - 1\right]^2} \,. \tag{56}$$

This shows that in order to minimize the losses due to radiation, b/λ, should be made small and b/a kept close to unity; however, as can be seen from a contour plot of Q_{rad} in Fig. 15, b/λ is the more important parameter.

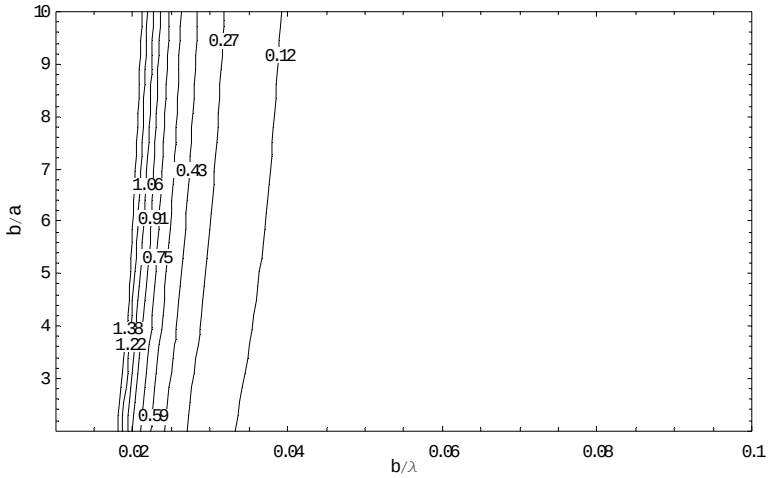

Fig. 15 Contour plot of Q_{rad} x 10^{-5} as given by (56)

The total Q of the QWCCR can then be approximated by

$$Q \approx \left(\frac{8 \cdot \pi^3 \cdot \left(\frac{b}{\lambda}\right)^4 \cdot \left[\left(\frac{b}{a}\right)^2 - 1\right]^2}{3 \cdot \left(\frac{b}{a}\right)^4 \cdot \ln\left(\frac{b}{a}\right)} + \frac{R_s}{2 \cdot \pi \cdot \eta} \left[\frac{\left(\frac{b}{a} + 1\right)}{\frac{b}{\lambda} \cdot \ln\left(\frac{b}{a}\right)} + 8 \right] + \tan\left(\delta_e\right) \right)^{-1} . \tag{57}$$

The optimum value will depend on the ratio of the cavity filling's intrinsic impedance to the surface resistance, R_s/η. Contour plots of the loaded quality factor, $Q_{\Gamma=0}$, under perfect coupling and the associated tip electric fields per square-root of power are given for brass at 2.45 GHz and copper at 915 MHz below in Fig. 16 through Fig. 19. Note that $Q_{\Gamma=0}$ is half the value given by (57). These two cases were chosen as a high and low for the surface resistance in the vicinity of the expected design parameters. As these figures show, maximum Q does not coincide with maximum tip electric field, and it is critical that the center conductor radius be small in order to achieve a high electric field. Once breakdown does occur, the energy stored in the cavity will be dumped into the plasma, and as such, a larger Q would be desirable. Q also plays a role in the time it takes a cavity to fill its energy store and for the electromagnetic fields to build up.

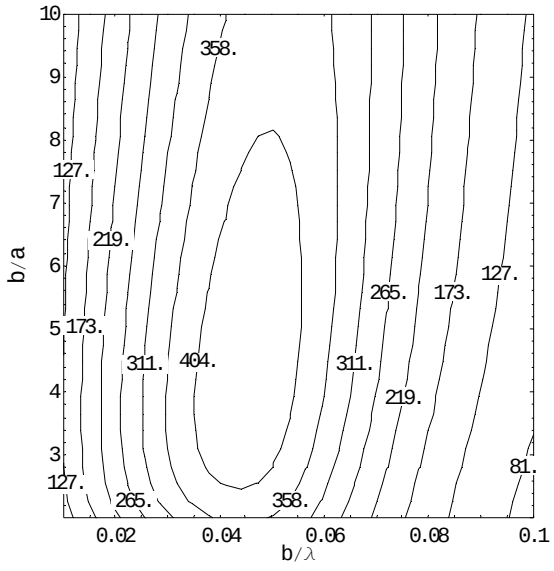

Fig. 16 Contour plot of the $Q/2$ for brass at 2.45 GHz, as given by (57), air dielectric

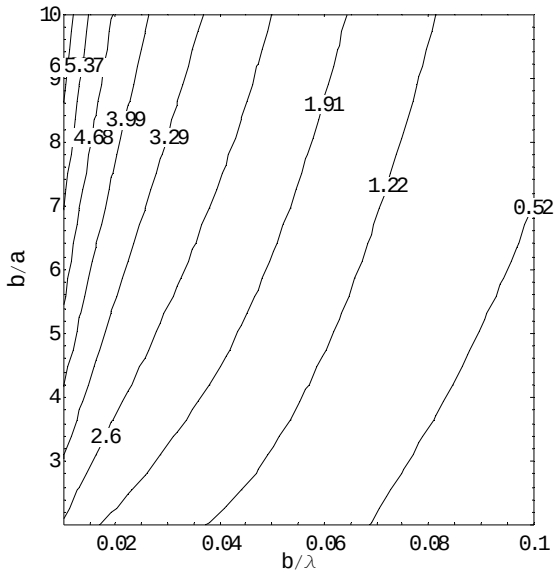

Fig. 17 Contour plot of E_a in (kV cm^{-1} W$^{-1/2}$) for brass at 2.45 GHz, as given by (30),air dielectric

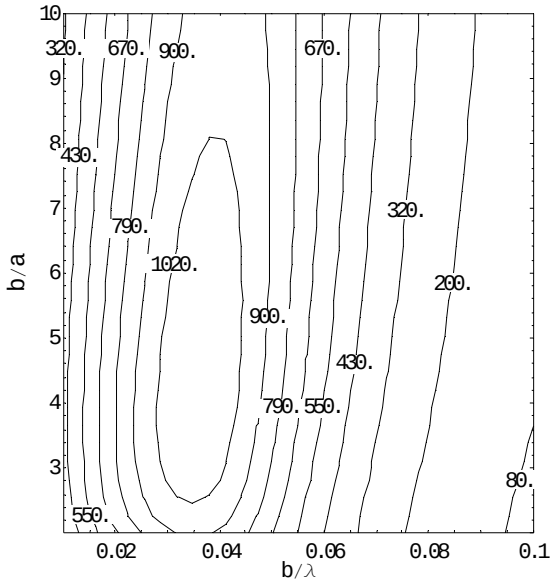

Fig. 18 Contour plot of $Q/2$ for copper at 915 MHz, as given by (57), air dielectric

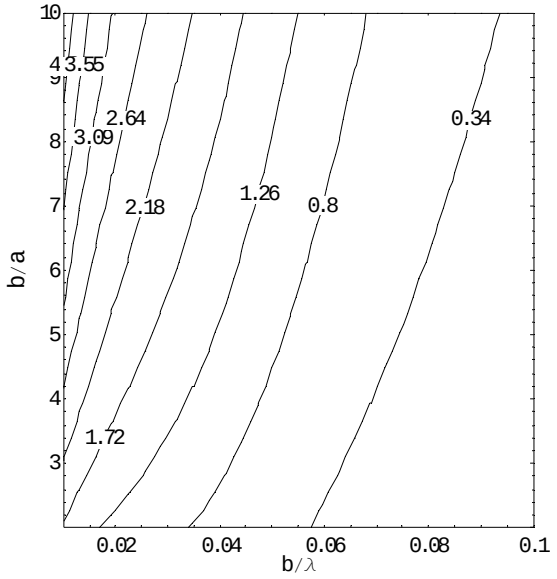

Fig. 19 Contour plot of E_a in (kV cm^{-1} W$^{-1/2}$) for copper at 915 MHz, as given by (30) air dielectric

3.3.3 Cavity Ringup and Energy Storage

The QWCCR at resonance is a system that trades energy back and forth between the magnetic and electric fields. This constitutes a second order system much like an RLC circuit at resonance. The characteristic equation for such a second order system is given by

$$s^2 + \frac{R}{L}s + \frac{1}{L \cdot C} = s^2 + 2 \cdot \zeta \cdot \omega_n \cdot s + \omega_n^2 = s^2 + \frac{\omega_n}{Q} \cdot s + \omega_n^2 , \tag{58}$$

with the natural resonance frequency ω_n , the damping coefficient of ζ, and s, the usual frequency domain variable. This highlights the direct relationship between Q and the damping coefficient ζ as $Q^{-1}=2\,\zeta$. It is well known that the time domain response of a second order system has a transient portion that decays exponentially with a time constant $(\zeta\,\omega)^{-1}$ or $2Q/\omega$. After 5 time constants, these transients are generally considered to have died out, the cavity will be filled with energy and the fields will have reached a steady state value. For a cavity resonant at 2.45 GHz with Q of 100 or greater, this would take 408ns or less, fast enough even for proper ignition timing of higher speed engines.

The energy stored in the cavity can be found by solving (21) for $U=P_L\,Q\,/\,\omega$. For a more thorough treatment including coupling coefficient and time dependence see Slater (Slater 1950). Again, for 2.45 GHz, and a Q of 100, the power stored would only be 41 μW per 1 kW input power. If 0.2 mJ is assumed as a minimum for ignition, and with typical ignition energies much higher than that, energy stored in the cavity can only be a minor contributor toward ignition in a system with a practical power input level in the 100s of Watts. The bulk of the energy will have to come from the power fed to the cavity and cannot rely on a discharge of the cavity's stored energy.

3.4 Analysis Results

The preceding approximate analysis reveals the following factors to consider when designing the geometry of a QWCCR with a large tip electric field. The parameter of highest significance is a small center conductor radius, a, possibly sharpened, as $E_a(\lambda/4)$ is directly inversely proportional to a. It is desirable to maximize the term $\eta\,Q\,P_L$, on which $E_a(\lambda/4)$ depends in the square root. This requires keeping the intrinsic impedance, η, of any filler material high, feeding the resonator as much power, P_L, as possible and maximizing Q. The latter can be accomplished by increasing the volume energy storage U of the cavity, and

minimizing surface and radiation losses. Radiation losses are excessive for large b/λ and the ratio $b/(\lambda\, a)$ is almost on equal footing with the center conductor radius in increasing tip electric field. As b/λ shrinks, conductor surface plus dielectric losses are on equal footing with radiation losses. In this region, the particulars of the materials and the frequency need to be examined. Designs can be accomplished by examining contour plots similar to Fig. 16 through Fig. 19. While the exact values given by such plots may not be realized in practice, they are a valuable design tool.

3.5 QWCCR Design and Implementation

With the preceding analysis of the QWCCR, a practical design was created out of alloy 360 brass. An air dielectric, with a large η was used and a design field strength requirement of greater than 30 kV cm^{-1} was selected. Such field strength is sufficient to cause breakdown under atmospheric conditions. Using Fig. 16, the contour plot for brass at 2.45 GHz, and a 100W power input, the region of the plot indicating field strength greater than 3 kV cm^{-1} $W^{-½}$ was identified. A major diameter of 1/4" or b/λ = 0.026 and a minor diameter of 1/32" or b/a ratio of 8 were selected, corresponding to an estimated field strength of 3.5 kV cm^{-1} $W^{-½}$ and a $Q_{\Gamma=0}$ of 270. Note that for this design to operate at the estimated 300 kV cm^{-1} necessary under 10:1 compression, the product $\eta\, Q\, P_L$ would have to increase by 100 according to (30), or the tip would have to be sharpened to a point with 1/10 the initial diameter to intensify the field.

Fig. 20 shows the implemented design for a 14-1.25 mm spark plug thread. Note the coaxial cable entering the base of the cavity. The coupling is accomplished through a small loop, created by the coaxial cable center conductor attaching back to the shield of the cable. Proper impedance matching between the cavity and the cable was accomplished by rotating the coaxial cable thereby turning the plane of the loop. This adjusts the magnetic linkage between the fields in the base of the cavity.

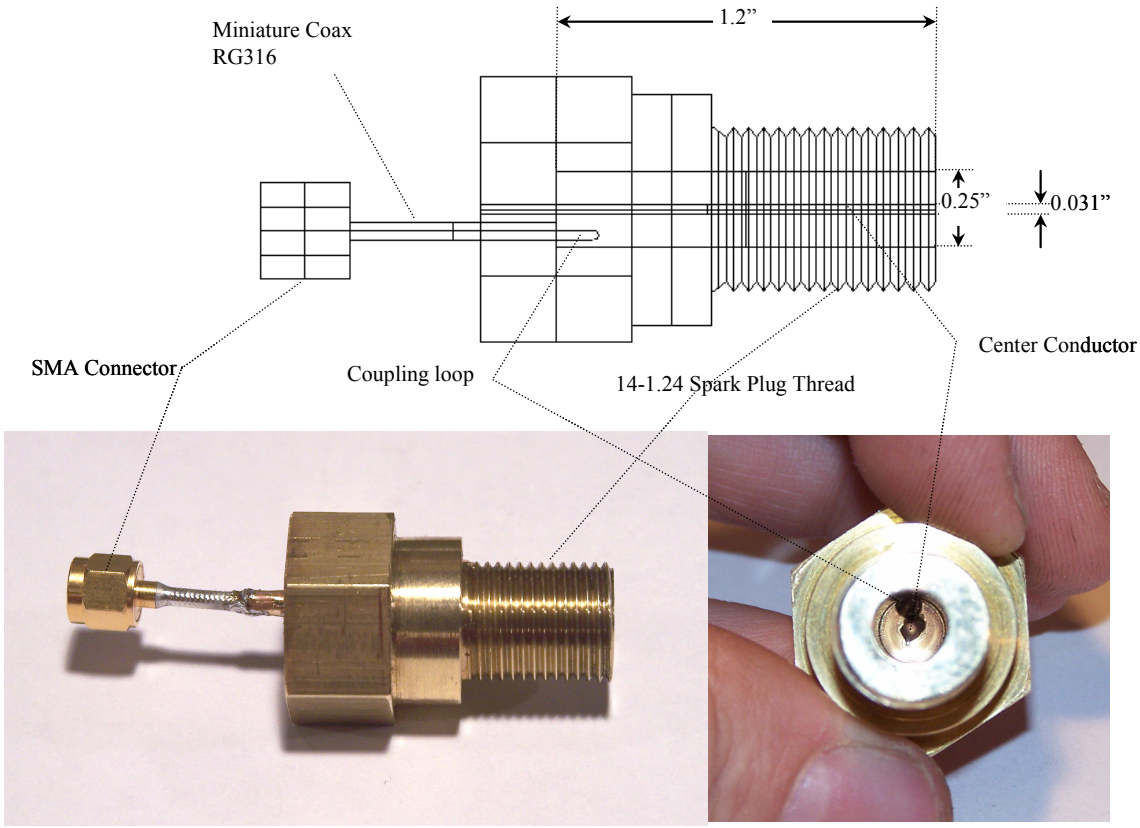

Fig. 20 QWCCR design and implementation

Once a coupling close to 1:1 was achieved, as measured with an HP8753D network analyzer, the coaxial cable was crimped and soldered in place. The achieved coupling and the loaded quality factor $Q_{\Gamma=0}$ was measured to be 258 at a resonant frequency of 2430.73 MHz. Note that the quality factor is somewhat lower than predicted by analysis. Theoretical surface resistance is generally not achievable due to surface imperfections and contaminations, such as oxidation. The magnetic fields in the base of the cavity are slightly disturbed by the presence of the coupling structure, which increases the losses slightly. Soldering also created a small amount of lower conductivity surface around the base center conductor. A photograph of the rounded tip of the cavity center conductor is given in Fig. 21.

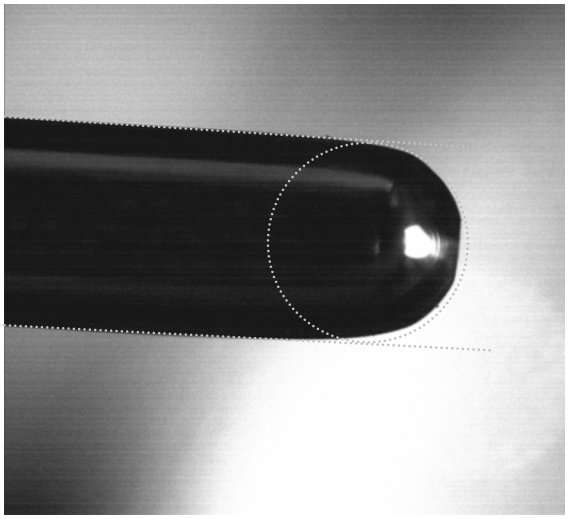

Fig. 21 Implemented rounded QWCCR center conductor tip

This shows the radius of curvature to be approximately the same as the radius of the center conductor, and no field enhancement through sharpening was employed. With the measured $Q_{\Gamma=0}$ of 253 this will produce a field strength of 3.46 kV cm^{-1} W$^{-1/2}$, or 42.4 kV cm^{-1} for 150 W.

3.6 Microwave Pulse Ignition and Measurement Electronics

In order to test the performance of the design, support electronics to provide and measure precisely timed pulses of microwave energy at the correct resonant frequency were assembled. A system diagram of the microwave pulse instrumentation is given below in Fig. 22.

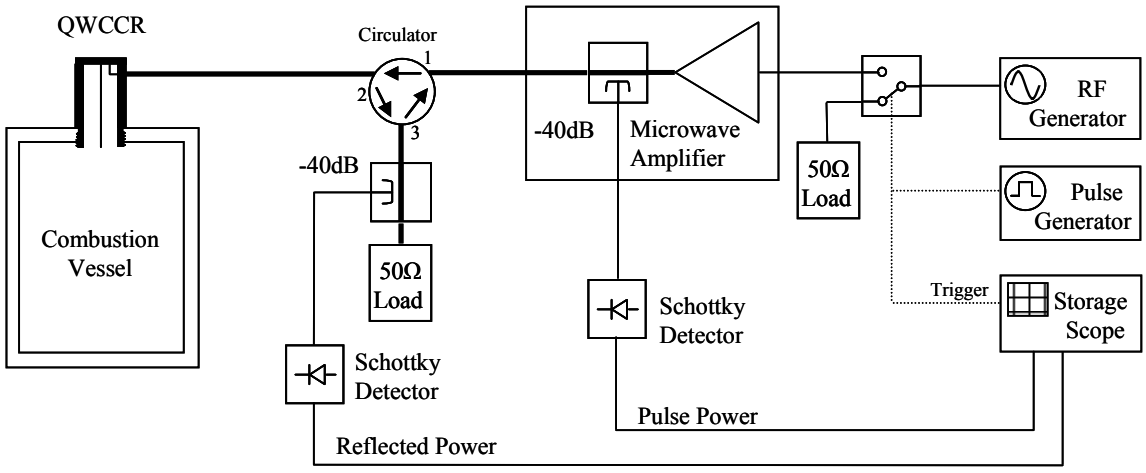

Fig. 22 Microwave pulse delivery and measurement system

The system delivered a microwave pulse, whose length, τ_p, was determined by the pulse generator to the QWCCR. The RF signal generator, a Hewlett Packard™ HP8648C, provided a low level microwave signal at the cavity resonant frequency. When the pulse was off, this signal was shunted to a 50 Ω load by a custom microwave switch. This switch was constructed from a RFMD™ RF2436 MESFET transmit/receive switch, a drain switched RFMD™ RF2126 amplifier and followed by a -30dB attenuator implemented on an FR4 printed circuit board material. This switch provided superior bandwidth to the modulation input of the RF signal generator.

The custom switch routed the microwave signal to a 200 W Amplifier Research™ AR200G1T3 power amplifier. A -40dB sample provided by the power amplifier was captured and the power envelope of the pulse was measured. The envelope detection was performed by a custom built 12 MHz bandwidth, temperature compensated Schottky diode detector based on a Linear Technologies™ LTC5535. Details of the detector circuit are given in the Appendix A. The pulse was then routed through a Pasternack™ PE8301 circulator to the QWCCR. The circulator provided 16.5 dB isolation between the power amplifier and the QWCCR by rerouting any energy reflected back by the QWCCR to a high power 50 Ω load. The reflected energy was again sampled at -40dB and envelope detected by another identical Schottkey diode detector. The output of the detectors was captured by a Tektronix™ TDS460A digital storage oscilloscope, which was edge triggered by the pulse generator. The time history of the pulse power and the reflected power, corrected for cable losses, allowed the necessary energy calculations to be performed. The forward path loss corrections were determined through simultaneous measurements with a Hewlett Packard™ HP8594E spectrum analyzer and the diode sensors. The forward path loss measurement was performed by replacing the QWCCR with the spectrum analyzer, protected by a 30 dB power attenuator. Similarly the reverse path loss was determined by leaving the QWCCR disconnected; causing an open termination which reflected all forward power. For this measurement, the 50 Ω load on port 3 of the circulator (see Fig. 22) was replaced with the attenuator protected spectrum analyzer. Pre and post test measurement of QWCCR coupling and the quality factor were also performed. These showed no appreciable changes (see Fig. 78 and Fig. 79 in Appendix A).

The microwave pulse energy accepted by QWCCR, U_{qw}, was calculated by numerically integrating the difference of the pulse power, P_{pls}, and the reflected power P_{ref}, as

$$U_{qw} = \int_{t=0}^{t=\tau_p} P_{pls}(t) - P_{ref}(t) \cdot dt \,. \tag{59}$$

The oscilloscope channels were set at 0.5 V/div and data was collected with a sample rate of 25 MHz.

3.7 Conventional Sparkplug Ignition Comparison System

In order to have a reference, the ignition tests were performed with a conventional capacitive discharge ignition (CDI) system and the microwave resonator ignition system. The conventional spark plug system served as an experimental control and provided a frame of reference for the microwave resonator results. The CDI igniter system was constructed using a AVX Corp.™ 1.5 μF 1100 V film power capacitors (FFB16L0155K), a 1 mA, 1.5 kV high voltage charging DC-DC supply, a STMicroelectronics™ silicon controlled rectifier (TYN816RG), a Motocraft™ E8AF-12029-BA ignition coil, high voltage copper wire and an AC Delco™ 44XLS non-resistive spark plug with a large gap spacing of 0.0755 inches. The large spacing was used to attain an atmospheric pressure breakdown threshold similar to that of a pressurized engine cylinder. This spacing was set by cutting back and polishing the center electrode of the spark plug to maintain a uniform field configuration. The breakdown voltage at an atmospheric 30 kV cm^{-1} breakdown field-strength was 5.8 kV for this gap. A schematic of the circuit is given in Fig. 23 and the spark plug is shown in Fig. 24.

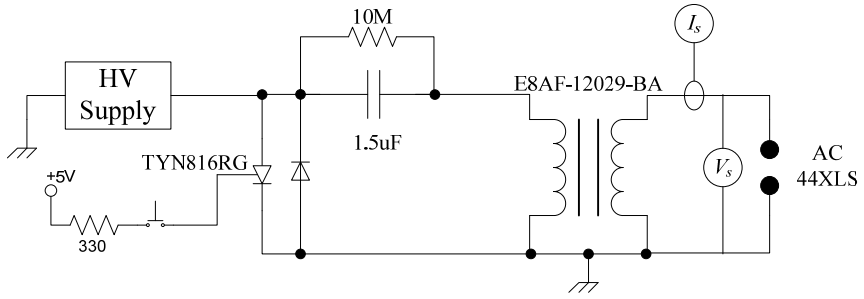

Fig. 23 CDI ignition system

Fig. 24 Spark plug use in ignition experiments

Note that the ignition coil efficiency was characterized in prior experiments by measuring the primary and secondary side of the coil for various sparks. The primary voltage was measured directly with the TDS460A oscilloscope and a conventional high voltage probe. The primary current was measured with a Tektronix™ A6302 probe and matching AM503A probe amplifier. During the ignition experiment and the prior coil characterization, the oscillating current through the spark plug, I_s, and the voltage across the spark plug, $V_{s,}$ were recorded with a high bandwidth (30 Hz to 60 MHz), ±1% accurate Pearson™ 2878 pulse transformer with a sensitivity of 0.1 V/A and a calibrated 1/1000 Tektronix™ 6015 high voltage probe. The use of a non-resistive spark plug allowed the spark energy, U_s, to be calculated through numerical integration of the product of the gap voltage, V_s, and the gap current, I_s, by

$$U_s = \int V_s(t) \cdot I_s(t) \cdot dt \,. \tag{60}$$

The high voltage probe was calibrated with a Meterman™ 37XR digital voltmeter, a high-voltage power supply and a resistive divider. The oscilloscope channel connected to the high voltage probe was set at 1 V per division and the channel connected to the current probe was set at 5 mV per division. The resulting expected accuracy for the power measurement was ±1.2%. Data was collected with a sample rate of 25 MHz.

3.8 Combustion Vessel and Associated Instrumentation

Combustion was contained in a combustion vessel made of 4 in schedule 80 steel pipe and flanges. Successful ignition and the ignition spark were observed through a view port. A system diagram of the experimental setup is shown in Fig. 25.

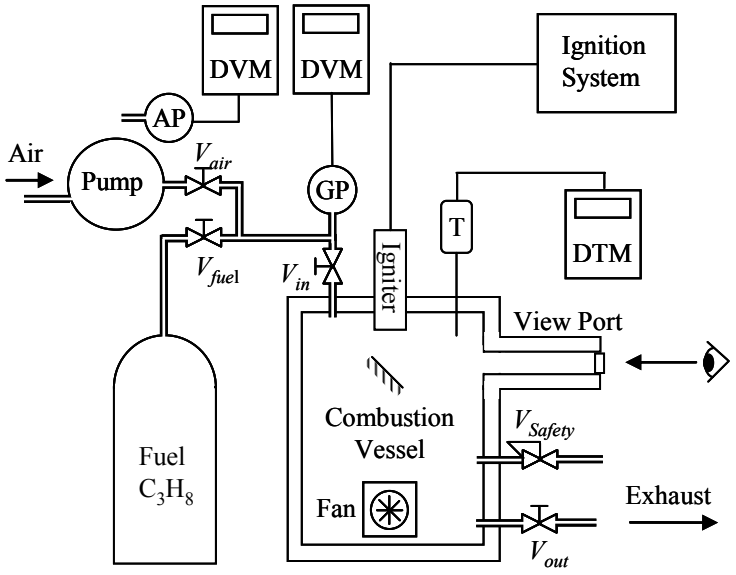

Fig. 25 Combustion vessel measurement system

The premix and postmix gas temperatures were monitored with a fast response Omega™ KMQSS-010E-6 thermocouple and an Omega™ HH506A temperature logger, DTM. Mixing of the air and fuel to a desired molar air fuel ratio, $\overline{far}$, was performed using Dalton's law of partial pressures for ideal gases (Cengel and Boles 1994) as follows: With the air valve, V_{air}, the inlet valve, $V_{in,}$ and the exhaust valve, V_{out}, open and all other valves closed, the pump was used to flush the vessel with fresh warm air for 5 min while the fan was running. Then the V_{air} and V_{out} valves were closed, the fan was turned off and the absolute pressure, P_{air}, and the absolute temperature, T_{air}, in the vessel were recorded with a calibrated Freescale™ MPX4250AP absolute pressure sensor, AP, and a Meterman™ 37XR digital voltmeter, DVM. The V_{fuel} valve was then partially opened long enough to raise the gauge pressure in the vessel to achieve the desired total pressure. The gauge pressure was recorded with a calibrated Freescale™ MPX5010DP and a second Meterman™ 37XR digital voltmeter, DVM, once the gas pressure had stabilized. At that time, the postmix temperature was recorded. From these measurements, the absolute pressure, P_{mix}, and absolute temperature, T_{mix}, were determined. Since a specific molar quantity of any ideal gas occupies the same volume at a given absolute temperature and pressure, the molar fuel to air ratio is given by

$$\overline{far} = \frac{P_{air} \cdot T_{mix}}{T_{air} \cdot P_{mix}} - 1 , \tag{61}$$

and the mixture composition in percent volume was calculated with

$$\left(\frac{1}{far}+1\right)^{-1}\cdot 100\%\,. \tag{62}$$

The MPX4250AP and the MPX5010DP sensors were calibrated with 0.05% accurate digital pressure calibrators, a Heise™ PTE-1 and a Fluke™ 713 30G, respectively. Given the pressure ranges of the calibrators, the experimental pressures, and the supply tubing volume, the expected accuracy of the mixture composition by volume was ±0.25% or better.

Ignition of the mixture was attempted a maximum of 10 times with a given amount of energy ignition energy, before slightly increasing the ignition energy. Prior to each ignition attempt, the mixture was agitated with the fan to assure that the liquefied-petroleum-gas (lpg) fuel and the air were well mixed. The actual ignition attempts were made with the fan off. The LPG used was 90% propane, and according to the combustion reaction for propane,

$$\mathbf{C}_3\mathbf{H}_8+5\left(\mathbf{O}_2+3.773\mathbf{N}_2\right)\rightarrow 3\mathbf{CO}_2+4\mathbf{H}_2\mathbf{O}+18.665\mathbf{N}_2\,, \tag{63}$$

a stoichimetric mixture requires 23.9 parts of air to 1 part of fuel by volume. This corresponds to a mixture that is 4.02% propane by volume. The gas mixing did not significantly affect the overall gas temperature. Assuming a constant gas temperature and 14.7 PSIA of barometric pressure, the required pressure increase for a stoichiometric mixture was determined to be 0.62 PSI. The reaction also shows that the final pressure of the combustion products was lower than the mixture starting pressure. The generated heat is rapidly lost through the massive uninsulated steel combustion vessel and the water vapor condenses leaving only 21.7 moles of products, having started with 24.9 moles of reactants. The water was removed by flushing the vessel with warm air between successful ignitions. The LPG fuel used was the commonly available United States commercial LPG as is used in many consumer and industrial applications. Upper and lower flammability for this fuel are 9% and 2% by volume, respectively, according to the material safety data sheet (MSDS). This range was explored by the comparative ignition experiments with emphasis on leaner mixture compositions at 4% and lower.

CHAPTER 4: Results and Conclusions

4.1 Spark Ignition Results

Spark plug ignition was attempted on 18 mixtures of various compositions in the range of 3% to 9% by volume. All but two mixtures could be ignited with the capacitive discharge ignition (CDI) system used. The system's upper energy delivery limit, at a capacitor charge of 840 V, was approximately 40 mJ. The capacitor initially held an energy of ½·1.487μF·(840V)^2 = 525 mJ, but the average spark power delivered was only 20 W for 2 ms. For lower capacitor charges, the delivered power was considerably less (as low as 5W). This emphasizes the inefficiencies of this traditional ignition system at delivering higher energies. The bulk of the losses can be attributed to the voltage step-up device, the ignition coil as indicated by measurement of the energy entering the coil primary, and energy of the spark (see Fig. 87 in Appendix A). Without these losses, the average power delivered should have been 260W.

At a very lean 3.4% composition, the CDI system could not provide enough power to two of the mixtures for ignition. Leaner mixtures were observed to burn with a blue flame, and richer mixtures burned bright yellow, darkening the view port with soot deposits formed by incomplete combustion. Typical wave forms are given below in Fig. 26. All captured voltage and current waveforms of the sparks are given in Appendix A, Fig. 60 through Fig. 77.

The voltage waveforms commence with a very short 40μs spike of magnitude equal to the breakdown voltage of the gap, which is followed by several arc oscillations. While this voltage spike produces a significant power spike, it is too brief for transferring substantial energy. The bulk of the energy is transferred at a lower power level during the oscillations, which are a result of the resonance circuit formed by the ignition coil and the discharge capacitor. The current waveforms can be characterized by a decaying sinusoid in phase and of the same frequency as the voltage oscillations. The lower level energy transfer to the gas occurs during the peaks of current oscillations, when the arc maintains an approximately current independent voltage. These waveforms were analyzed to determine the energy content for each mixture

tested. The results are summarized in the graphs below in Fig. 27. The U shape of the data in Fig. 27 parallels what was found in the literature (see Fig. 7). Note that higher energies for a particular mixture composition will also cause ignition, and the interior of the U constitutes the region where ignition is possible. The exact energies required are dependent on the particulars of the spark plug and the nature of the combustion vessel. This data provides a frame of reference for the QWCCR ignition data.

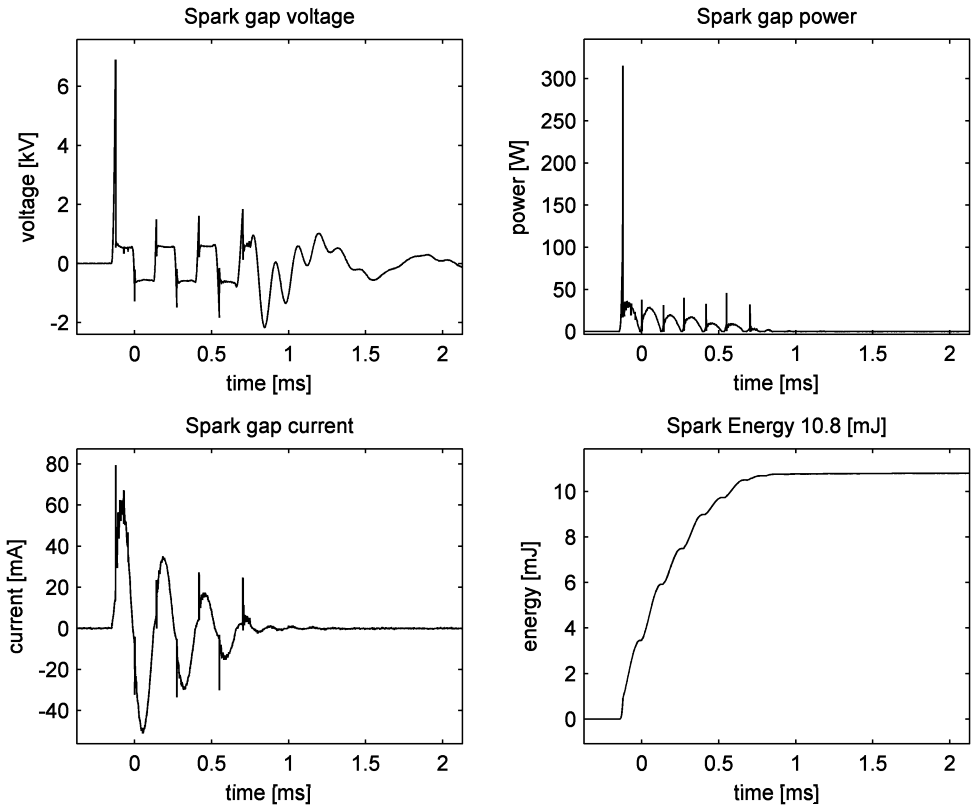

Fig. 26 Successful spark ignition of 3.9% LPG by volume

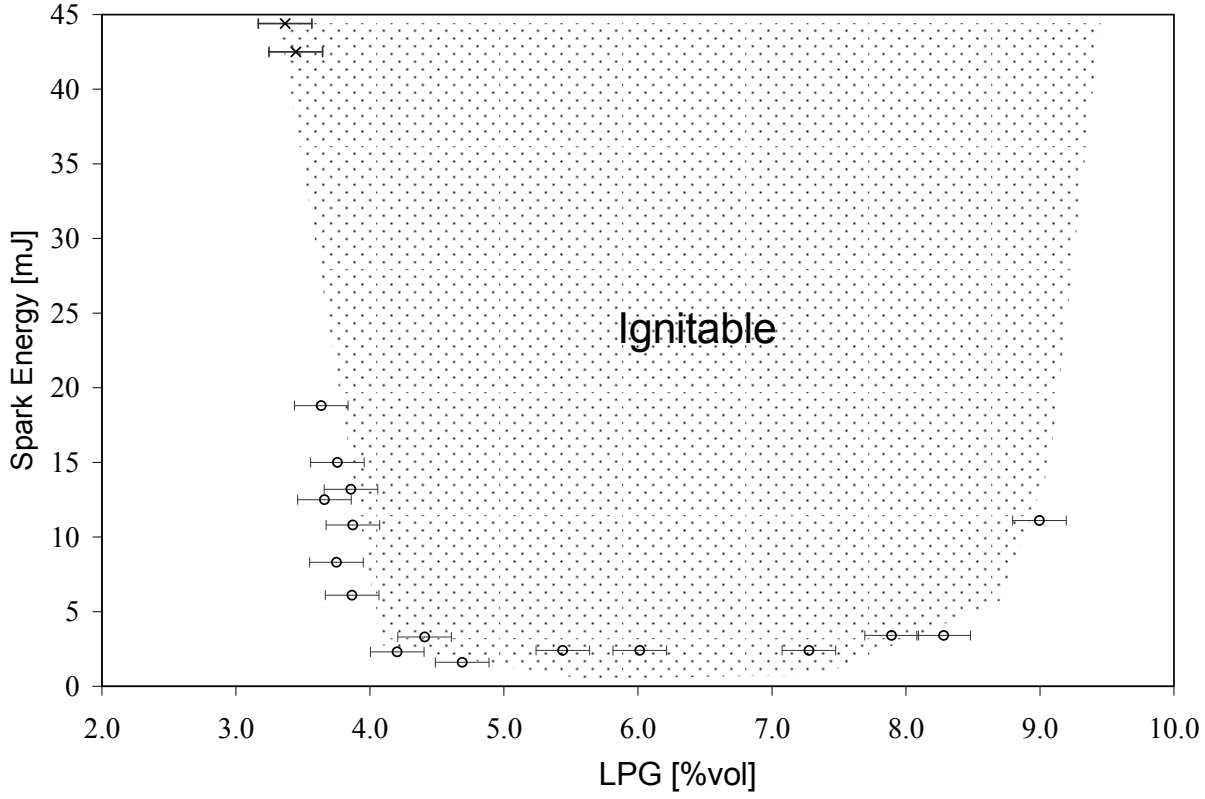

Fig. 27 Spark energy data (o ignited; + did not ignite)

4.2 Microwave Ignition Results

The particular QWCCR ignition was tested on 27 mixtures of various compositions in the range of 3 to 9% by volume. All but three of these mixtures resulted in successful ignition. The system's upper limit for energy and power delivery is a function of the available microwave power and the duration of the pulse. A nominal power of 150 W was used with pulse lengths comparable to the duration of the CDI spark. The microwave ignition system easily sustained this power level for the duration of the pulse. The oscillations in the longest ignition spark shown in Fig. 61 took approximately 2 ms die out. At 150 W, a microwave pulse of 2 ms could potentially deliver up to 300 mJ of energy, all at the much larger 150W power level. The collected data for ignition energies for the various mixture compositions is summarized in Fig. 30. The equipment limited available power of 150W could not ignite a lean 3% and a rich 9% mixture. It was not

possible to separately measure the dynamic losses on the interior of the QWCCR and calculate a step-up efficiency, but the data clearly shows that the total energy accepted by the QWCCR is comparable to the energy required for ignition by a conventional spark. A typical set of waveforms is given below in Fig. 28.

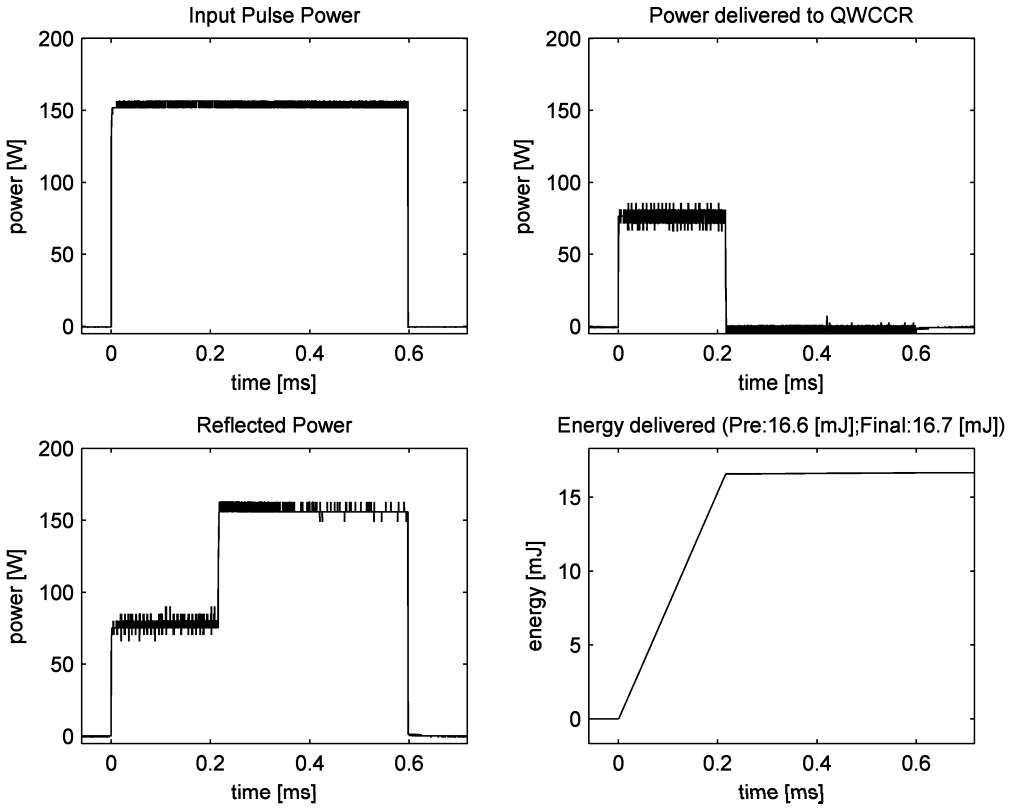

Fig. 28 QWCCR successful ignition of 3.8% LPG by volume

Approximately half the microwave input power is reflected by the QWCCR from the beginning of the pulse. Some time later during the pulse, all, or nearly all of the power is reflected. In open air, this change in power reflection coincides with the formation of optically visible plasma. This step can be taken as an indication that significant energy has been transferred to the gas which has formed a conductive microwave plasma discharge. Given that the HP8594E spectrum analyzer is only accurate to within ±0.3 dB, it is not possible to accurately determine the amount of power delivered to the QWCCR after this plasma has formed. Since some power is necessary to maintain a discharge, this power is not identically zero. Only if

the pulse causes breakdown reasonably late in its duration can energies be inferred reliably from the collected data. Ignition of lean mixtures, as shown by the CDI system spark data earlier, requires energy transfer after the breakdown. Plasma pulse data for a lean mixture at 3.5% LPG is shown in Fig. 29. Note that the energy given by the integration is dominated by the uncertain portion of the pulse after the very early breakdown.

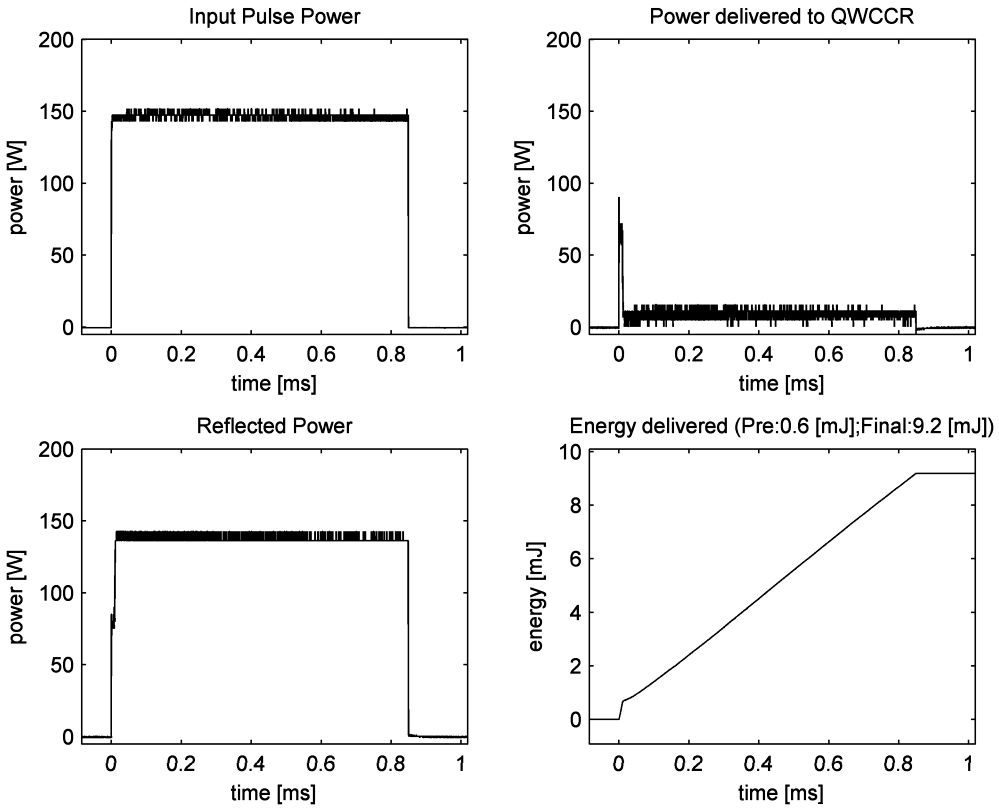

Fig. 29 QWCCR successful ignition of 3.5% LPG by volume

With this in mind, the collected data was analyzed and energy integration was performed in two steps: a pre-breakdown energy and a total energy were calculated for each pulse. Prior to integrating, a median and average filter were applied to the data to remove bit noise from the oscilloscope analog to digital converter. If the two energies given by the integration differ significantly, the overall energy measurement is likely to be uncertain. Given the statistical nature of when the breakdown happened during the pulse, this uncertainty

varied on an individual basis. Note that leaner mixtures required longer, more energetic pulses that caused breakdown early. The results of the final microwave ignition energies with error bars are displayed in Fig. 30.

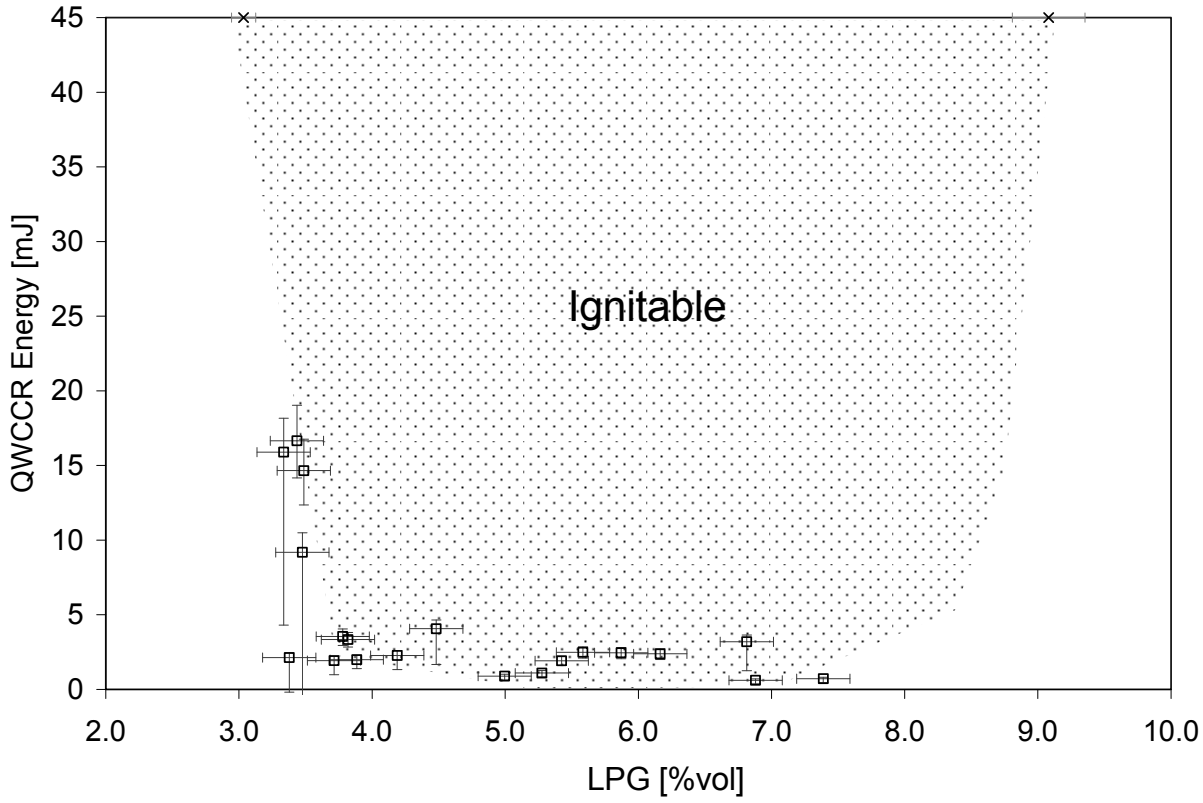

Fig. 30 QWCCR energy data (□ ignited; × did not ignite)

4.3 Comparison of Results

A comparison of Fig. 30 to Fig. 27 indicates that for mixtures close to stoichiometric, and slightly rich mixtures, both the spark plug spark and the QWCCR require a similar amount of energy for ignition, approximately 5 mJ. Both also require more energy to ignite lean mixtures, however, it remains uncertain from this data whether the QWCCR required about the same or less energy than a conventional spark for these lean mixtures. Energy transfer by the QWCCR can also be achieved at a much higher and controllable average power level and the step-up of the energy to a potential necessary for breakdown is

achieved with much greater efficiency than by an ignition coil. If the QWCCR is modified to accept the now reflected power, a substantial efficiency advantage over the spark plug ignition coils system can be obtained. Given larger input pulse powers, such as can be generated by a microwave magnetron, the QWCCR does have the potential to deliver substantial amounts of energy in short periods of time. A 1 kW, 1ms microwave pulse could potentially deliver 2000 mJ. Operation at such high power levels would be beneficial for lean ignition.

4.4 Conclusion

The experimental data shows that the microwave plasma discharge generated by the QWCCR is as good an ignition source as conventional spark for easily ignitable mixtures, whose composition is close to stoichiometric or slightly rich. Although advantages of the QWCCR for ultra lean ignition are not directly supported by the data, further experimentation using more accurate and precise microwave instrumentation could verify these, and provide an improved statistical picture. As with spark breakdown and ignition, microwave breakdown and ignition are strongly dependant on the conditions at the breakdown site. It is however evident that the QWCCR can easily deliver ignition energy at considerably larger power levels than the CDI system used. This additional power will be necessary for the ignition of ultra lean mixtures leaning to higher combustion efficiencies and the associated fuel-savings.

Returning to the design aspects of the QWCCR, there is substantial potential for optimization by changes in the geometry that will reduce radiation losses through the aperture, and by maintaining a high volume to interior surface area ratio. The theoretical analysis performed allows the prediction of cylindrical design performance using the derived equations and design graphs. Much like choosing appropriate gap spacing for a spark plug, the radius of the center conductor at the tip can be chosen to cause breakdown at a given desired field strength. In spark plugs this allows energy to build up prior to the breakdown event. This is also true for the QWCCR and additionally a larger exposed tip area can be turned into plasma at breakdown. This can aid in the ignition of the mixture, however, if the tip is chosen too large, breakdown may not occur reliably, or at all. Further improvements in QWCCR design can be made through selection of

low loss materials to improve the quality factor and the associated resonant field step-up to higher potentials.

4.5 Recommendations

Future cavity designs should consider non-cylindrical designs, especially tapered designs. The taper can provide a small aperture, b/λ, and large volume resulting in considerable improvements in cavity Q. Such tapers can be constructed to maintain a constant radius ratio, b/a, and maintain a constant impedance quarter wave section in which a resonant field can build-up. Narrowing of the cavity near the opening will also intensify the fields at the tip, by placing the maximum electric potential across a smaller distance, (b–a).

Future experimental work needs to be performed with improved instrumentation that should explore ignition of very lean mixtures. It would be beneficial to sample the power in the QWCCR cavity as a direct measurement of the energy entering the QWCCR. Energy coupling to the resonator needs to be improved to prevent the majority of the energy from being reflected once breakdown occurs. This could be accomplished by tracking the resonance frequency of the cavity to dynamically modify the frequency of the driving signal.

A simpler approach is to directly incorporate the QWCCR as the frequency determining element in the microwave oscillator by using a closed loop feedback scheme with appropriate signal phase adjustment for oscillation and switching control. Such a feedback oscillator design with the QWCCR could also provide valuable information about the combustion process. By monitoring the feedback loop which is coupled with the dynamics of the resonator frequency and the resonators impedance changes, high-speed in-cylinder combustion diagnostics may be possible.

BIBLIOGRAPHY

Anderson, D.G., Lisak, M., and Lewin, P.T., "Thermal Lowering of the Threshold for Microwave Breakdown in Air-Filled Waveguides," *IEEE Transactions on Microwave Theory and Techniques*, Vol. 35, No. 7, July 1987.

Anikin, N.B., Mintoussov, E.I., Pancheshnyi, S.V., Roupassov, D.V., Sych, V.E., and Starikovskii, A.Y., "Nonequilibrium Plasmas and its Applications for Combustion and Hypersonic Flow Control," AIAA Paper 2003-1053, *41st AIAA Aerospace Science Meeting Exhibit*, Reno, NV, Jan. 9-12, 2003.

Balanis, C., Advanced Engineering Electromagnetics, New York, NY: John Wiley & Sons, 1989.

Ballal, D.R., and Lefebvre, A.H., "Influence of Flow Parameters on Minimum Ignition Energy and Quenching Distance," *Proceedings of Fifteenth International Symposium on Combustion*, pp 1473-1481, The Combustion Institute, 1974.

Baretto, E., "Ignition by Electric Sparks," *5th Conference on Electrostatic Phenomena*, The Institute of Physics, St. Catherine's College, Oxford, 1979.

Berezhetskaya, N.K., Gritsinin, S.I., Kop'ev, V.A., Kossyi, I.A., Popov, N.A., Silakov, V.P., and Van Wie, D., "Microwave Discharge as a Method for Igniting Combustion in Gas Mixtures," AIAA Paper 2005-0991, *43rd AIAA Aerospace Sciences Meeting and Exhibit*, Reno, NV, Jan 10-13, 2005.

Bonazza, T.J., Van Voorhies, K.L., and Smith, J.E., "RF Plasma Ignition System Concept for Lean Burn International Combustion Engines," SAE Paper 929416, 1992.

Bone, W.A., and Townend, T.A, Flame and Combustion in Gases, London, England: Longmans, Green and Co. Ltd., 1927, p 89.

Brown, S.C., and MacDonald, A.D., "Limits for the Diffusion Theory of High-Frequency Gas Discharge Breakdown," Technical Report No. 132, Research Laboratory of Electronics, Massachusetts Institute of Technology, 1950.

Brown, S.C., Introduction to Electrical Discharges in Gases, New York, NY: John Wiley, 1966.

Cengel, Y.A., and Boles, M.A, Thermodynamics, An Engineering Approach 2nd ed., New York, NY: McGraw-Hill, 1994, p 668.

Chintala, N., Bao, A., Lou, G., and Adamovich, I.V., "Measurements of Combustion Efficiency in Nonequilibrium RF Plasma-Ignited Flows," *Combustion and Flame*, Vol. 144, 2006, pp 744-56.

Coward, H.F., and Jones, G.W., "Limits of Flammability of Gases and Vapours," Bulletin 503, U.S. Department of the Interior, Bureau of Mines, 1952.

Dale, J.D., Checkel, M.D., and Smy, P.R., "Application of High Energy Ignition Systems to Engines," *Progress in Energy and Combustion Science*, Vol. 23, pp 379-398, 1997.

Henry, K., Radio Engineering Handbook 5th ed., New York, NY: McGraw-Hill, 1959, pp 6.46-6.58.

Heywood, J.B., Internal Combustion Engine Fundamentals, New York, NY: McGraw-Hill, 1988, pp 427-437.

Lankin, W.P., Thwaites, H.L., Skarstorm, C.W., and Baum, A.W., "Fourth Annual Report on Fundamental Combustion Studies," *Esso Labs Report No.* RL-5M-48(69), Standart Oil Dev. Co., Nov. 30, 1948.

Leonov, A.B., Yarantsev, D.A., Napartovich, A.P., and Kochetov, I.V., "Plasma-Assisted Ignition and Flame Holding in High-Speed Flow," AIAA Paper 2006-563, *44th AIAA Aerospace Sciences Meeting and Exhibit*, Reno, NV, 2006.

Lewis, B., and von Elbe, G., "Ignition and Flame Stabilization in Gases," *Trans. ASME*, Vol. 70, pp 307-316, 1948.

Lieberman, M.A., "Plasma Processing in the 21st Century," *Berkeley Dept. of Electrical and Computer Science*, Berkeley, CA, May 9, 2005.

Linkenheil, K., Ruoβ, H.O., and Heinrich, W., "Design and Evaluation of a Novel Spark-Plug Based on a Microwave Coaxial Resonator," *34th European Microwave Conference*, Amsterdam, Netherlands, 2004.

Lowery, Andrew D., "An Experimental and Computational Investigation of Dielectrics for use in Quarter Wave Coaxial Cavity Resonators," Master Thesis, West Virginia University, Morgantown, WV, 2006.

MacDonald, A.D., Gaskell, D.U., and Gitterman, H.N., "Microwave Breakdown in Air, Oxygen, and Nitrogen," *Physical Review*, Vol. 130, No. 5, June 1, 1963.

MacDonald, A.D., Microwave Breakdown in Gases, New York, NY, John Wiley, 1966.

MacDonald, A.D., and Tetenbaum, S.J., "High Frequency and Microwave Discharges," in Ch 3 of Hirsh, M.N, VOskam, H.J., Gaseous Electronics Vol. 1 Electrical Discharges, New York, NY, Academic Press, 1978.

Maly, R., "Spark Ignition: Its Physics and Effect on the Internal Combustion Engine," in Hillard, J.C. and Springer, G.S., Fuel Economy in Road Vehicles Powered by Spark Ignition Engines, Ch. 3, Plennum Press, New York, NY, 1984, p 91.

Maly, R., Saggau, B., Wagner, E., and Zigler, G., "Prospects of Ignition Enhancement," SAE Paper 830478, *SAE Transactions*, Vol. 92, 1983.

Maly, R., and Vogel, M., "Initiation and Propagation of Flame Fronts in Lean CH_4-Air Mixtures by the Three Modes of the Ignition Spark," *Proceedings of Seventeenth International Symposium on Combustion*, The Combustion Institute, 1976, pp 821-831.

Marcuvitz, N., Waveguide Handbook, New York, NY, McGraw-Hill, 1951, pp 213-216.

McDaniel, E.W., Collision Phenomena in Ionized Gases, New York, NY, John Wiley, 1964, p 19.

McIntyre, Dustin L., "The Coaxial Cavity Resonator as a Prototype RF IC Engine Ignition Source," Master Thesis, West Virginia University, Morgantown, WV, 2000.

McMillian, M., Richardson, S., Woodruff, S.D., and McIntyre, D., "Laser-Spark Ignition Testing in a Natural Gas-Fueled Single-Cylinder Engine," SAE Paper 2004-01-0980, 2004 SAE World Congress, Detroit, MI, Mar. 8-11, 2004.

Mullins, B.P., and Penner, S.S., Explosions, Detonations, Flammability and Ignition, New York, NY, Pergamon Press, 1959.

Nash, M.A., "The Coaxial Cavity Resonator and R.F. Power Processing," Master Thesis, West Virginia University, Morgantown, WV, 1988.

Pancheshnyi, S., Lacoste, D.A., Bourdon, A., and Laux, C.O., "Ignition of Propane-Air Mixtures by Repetitively Pulsed Nanosecond Gas Discharges," *Proc. 17th Int. Symp. on Plasma Chemistry*, Toronto, Canada, Aug. 7-12, 2005.

Platzman, P.M., and Solt, E.H., "Microwave Breakdown of Air in Nonuniform Electric Fields," *Physical Review*, Vol. 119, No. 4, Aug. 1960, p 1143.

Quiles, C.P.V., "Passive Intermodulation and Corona Discharge for Microwave Structures in Communications Satellites," Dissertation, Technische Universität Darmstatt, Darmstatt, Germany, 2005.

Rager, J., "Funkenerosion an Zündketzenelectroden (Spark erosion of spark plug electrodes)," Ph.D. Dissertation, University of the Saarland, Stuttgart, Germany, 2006.

Roth, J.R., Industrial Plasma Engineering, Philadelphia, PA, Institute of Physics Publishing, 1995.

Rousseau, S., Lemoult, B., and Tazerout, M., "Combustion Characterization of Natural Gas in a Lean Burn Spark-Ignition Engine," *Proceedings of the Institution of Mechanical Engineers*, Vol. 213, Part D, p 481, 1999.

Slater, J.C., Microwave Electronics, D. Van Nostrand Company, Inc. Princeton, NJ, 1950.

Smith, J.E., Craven, R.M., Van Voorhies, K.L., and Bonazza, T.J., "Radio Frequency Coaxial Cavity Resonator as an Ignition Source and Associated Method," United States Patent No. 5,361,737, Nov. 8, 1994.

Starikovskaia, S.M., "Topical Review: Plasma Assisted Ignition and Combustion," *Journal of Physics D: Applied Physics*, Vol. 39, August 2006, pp R265-29.

Stiles, R.D., Thompson, G.J., and Smith, J.E., "Investigation of a Radio Frequency Plasma Ignitor for Possible Internal Combustion Engine Use," SAE Paper 970071, 1997.

Stiles, R.D., and Smith, J.E., "Modeling the Radio Frequency Coaxial Cavity Plasma Igniter as an Internal Combustion Engine Ignition System," SAE Paper 980168, 1998.

Soldera, F.A., Mücklich, F.T., Hrastnik, K., and Kaiser, T., "Description of Discharge Process in Spark Plugs and its Correlation with Electrode Erosion Patterns," *IEEE Transactions on Vehicular Technology*, Vol. 53, No. 4, 2004.

Tomala, R., "Microwave Breakdown in Air-Filled Waveguides and Resonators," Thesis, Chalmers University of Technology, Goeteborg, Sweden, 2005.

Van Voorhies, K.L., Bonazza, T.L., and Smith, J.E., "Analysis of RF Corona Discharge Plasma Ignition," Technology for Energy Efficiency in the 21st Century, Proc. of the 27th Intersociety Energy Conversion Engineering Conference, SAE Paper 929502, 1992.

Von Hagen, J., Venot, Y., Zhang, Y., and Wiesbeck, W., "Microwave-Generated Plasma in Air Under Standard Conditions," *IEEE Transactions on Plasma Science*, Vol. 29, No. 4, 2001.

Wang, F., Liu, J.B., Sinibaldi, J., Brophy, C., Kuthi, A., Jiang, C., Ronney, P., and Gundersen, M.A., "Transient Plasma Ignition of Quiescent and Flowing Air/Fuel Mixtures," *IEEE Transactions on Plasma Science,* Vol. 33, No. 2, 2005.

Wightman, J.P., "Chemical Effects of Microwave Discharges," *Proceedings of the IEEE*, Vol. 62, No. 1, 1974.

Wolf, R.A., "Design of Electrical Equipment for Intrinsic Safety," First WVU Conference on Coal Mine Electrotechnology, West Virginia University, Aug 2-4, 1972.

Woo, R., "Final Report on RF Voltage Breakdown in Coaxial Transmission Lines," NASA Technical Report 32-1500, JPL California Institute of Technology, Pasadena, CA, 1970.

Woo, W., and De Groon, J.S., "Microwave Absorption and Plasma Heating Due to Microwave Breakdown in the Atmosphere," *Physics of Fluids*, Vol. 27, No. 2, pp 475-487, 1984.

Woo, R., "Final Report on RF Voltage Breakdown in Coaxial Transmission Lines," NASA Technical Report 32-1500, Jet Propulsion Laboratory, California Institute of Technology, Pasadena, CA, Oct. 1, 1970.

Zaidi, S.H., Stockman, E., Qin, X., Zhao, Z., Macheret, S., Ju, Y. Miles, R.B., Sullivan, D.J., and Kline, J.F., "Measurements of Hydrocarbon Flame Speed Enhancement in High-Q Microwave Cavity," AIAA Paper 2006-1217, *44th AIAA Aerospace Sciences Meeting and Exhibit*, Reno, NV, 2006.

APPENDIX A

A.1 QWCCR IGNITION TEST DATA

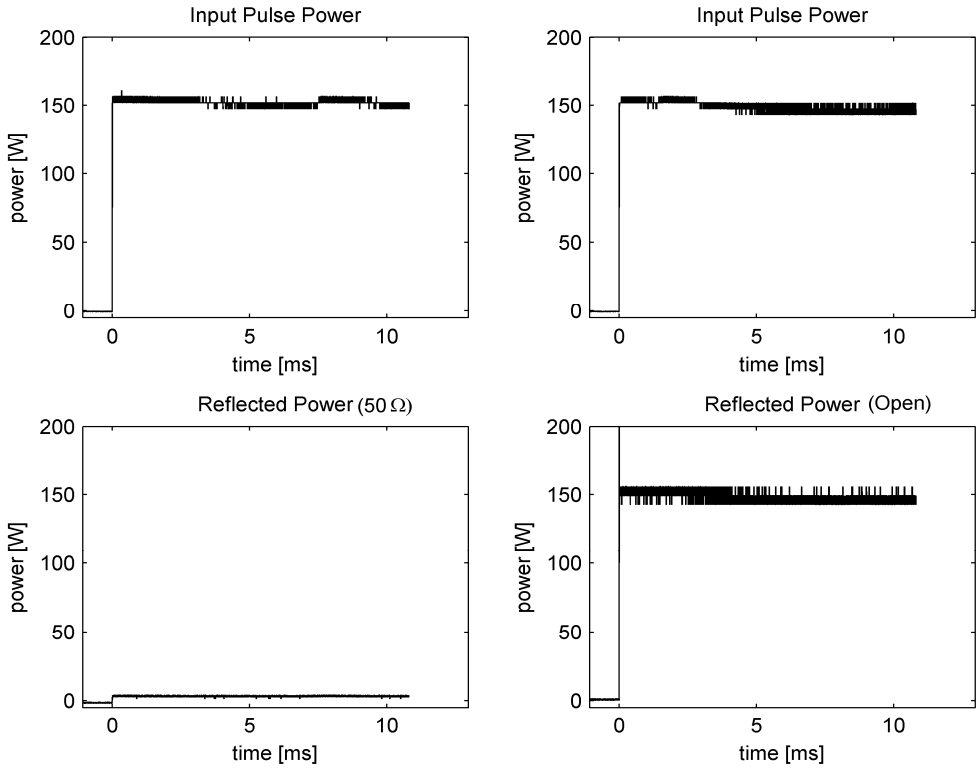

Fig. 31 Forward and reverse path loss test for 50 Ω load and open

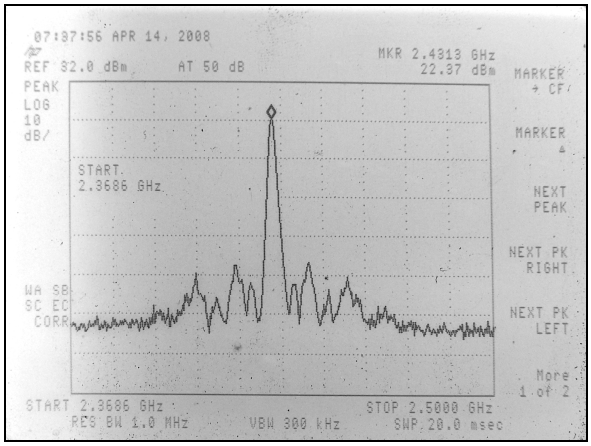

Fig. 32 Spectrum analyzer measurement of signal

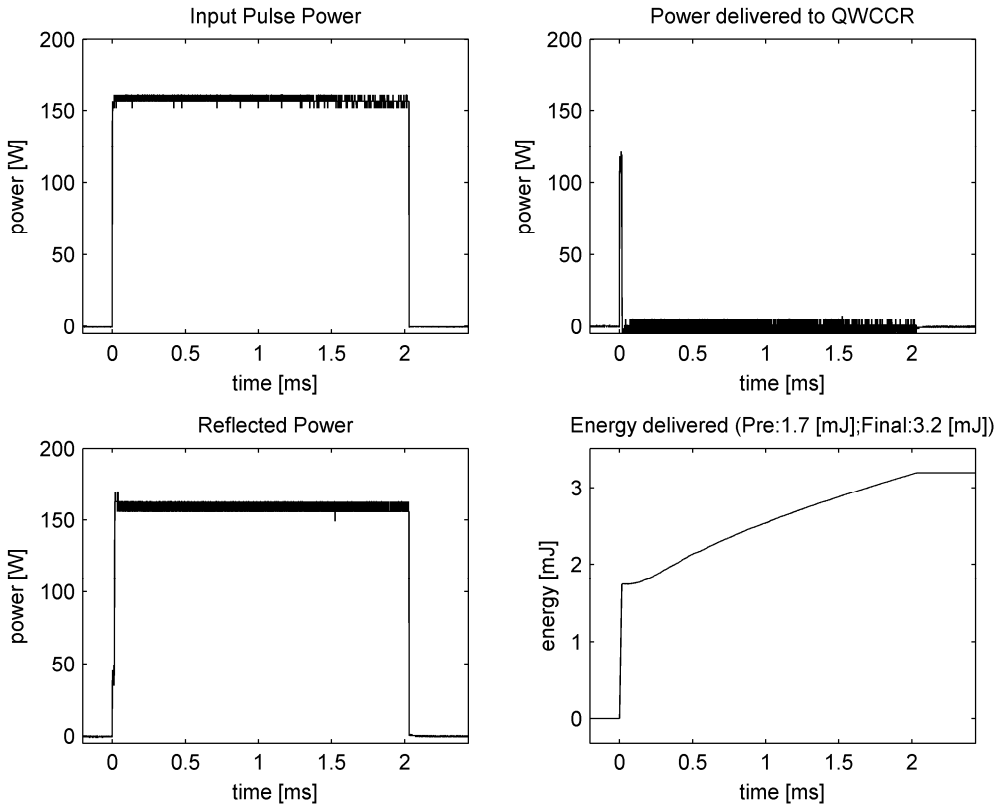

Fig. 33 QWCCR, successful ignition of 5.9% LPG by volume

Table 1 Test-29 data for 5.9% LPG

Pre Mix Temperature	61.9	ºF
Final Temperature	62	ºF
Barometric Pressure	14.18	PSIA
Initial Gauge Pressure	0.00	PSIG
Final Gauge Pressure	0.89	PSIG
Fuel to Air Ratio	0.062	
Mixture Composition	5.9	% by Vol.
Input Pulse Average Power	157	Watt
Pulse Length	2.031	ms
Pulse Energy	318.9	mJ
Energy Delivered	3.2	mJ
Trigger Count	1	

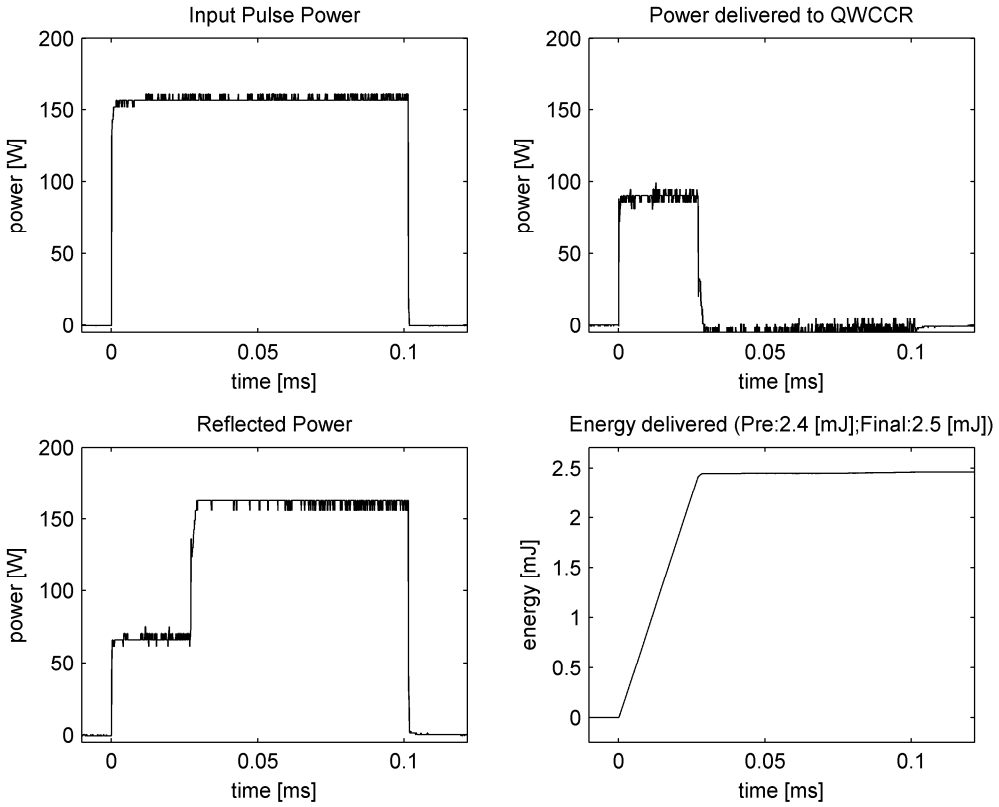

Fig. 34 QWCCR, successful ignition of 4.9% LPG by volume

Table 2 Test-30 data for 4.9% LPG

Pre Mix Temperature	63	ºF
Final Temperature	63	ºF
Barometric Pressure	14.17	PSIA
Initial Gauge Pressure	0.00	PSIG
Final Gauge Pressure	0.74	PSIG
Fuel to Air Ratio	0.052	
Mixture Composition	4.9	% by Vol.
Input Pulse Average Power	154	Watt
Pulse Length	0.103	ms
Pulse Energy	15.9	mJ
Energy Delivered	2.5	mJ
Trigger Count	1	

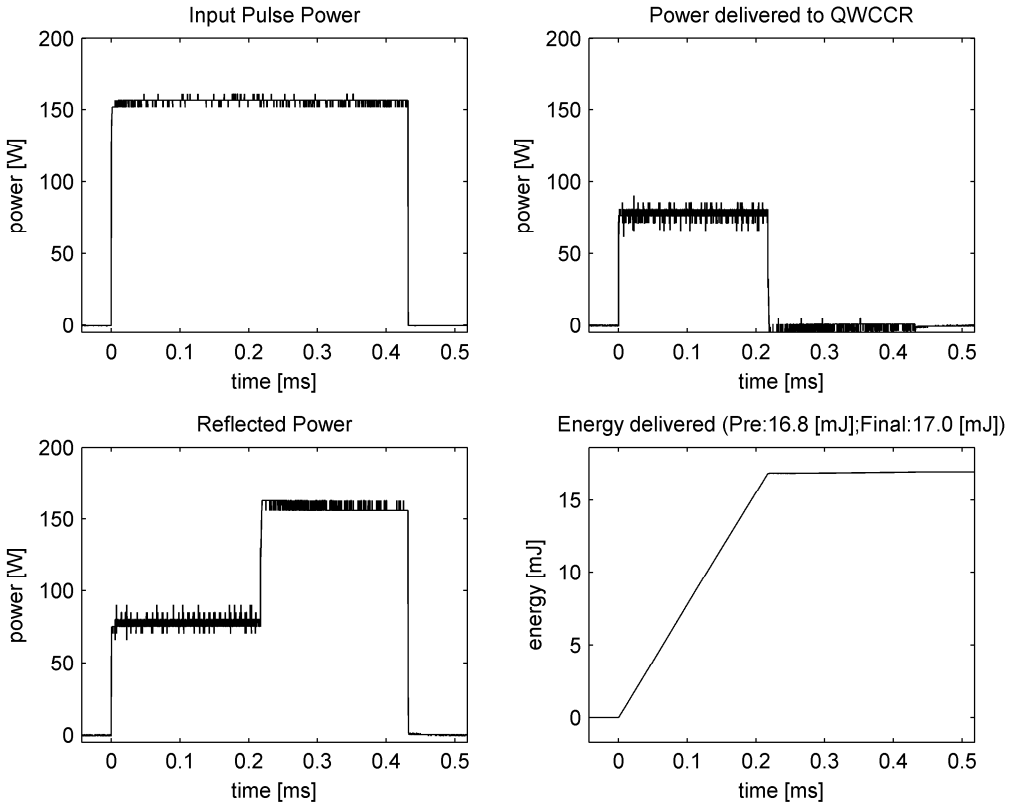

Fig. 35 QWCCR, successful ignition of 4.1% LPG by volume

Table 3 Test-31 data for 4.1% LPG

Pre Mix Temperature	65	ºF
Final Temperature	64.3	ºF
Barometric Pressure	14.17	PSIA
Initial Gauge Pressure	0.00	PSIG
Final Gauge Pressure	0.63	PSIG
Fuel to Air Ratio	0.043	
Mixture Composition	4.1	% by Vol.
Input Pulse Average Power	155	Watt
Pulse Length	0.433	ms
Pulse Energy	67.1	mJ
Energy Delivered	17.0	mJ
Trigger Count	7	

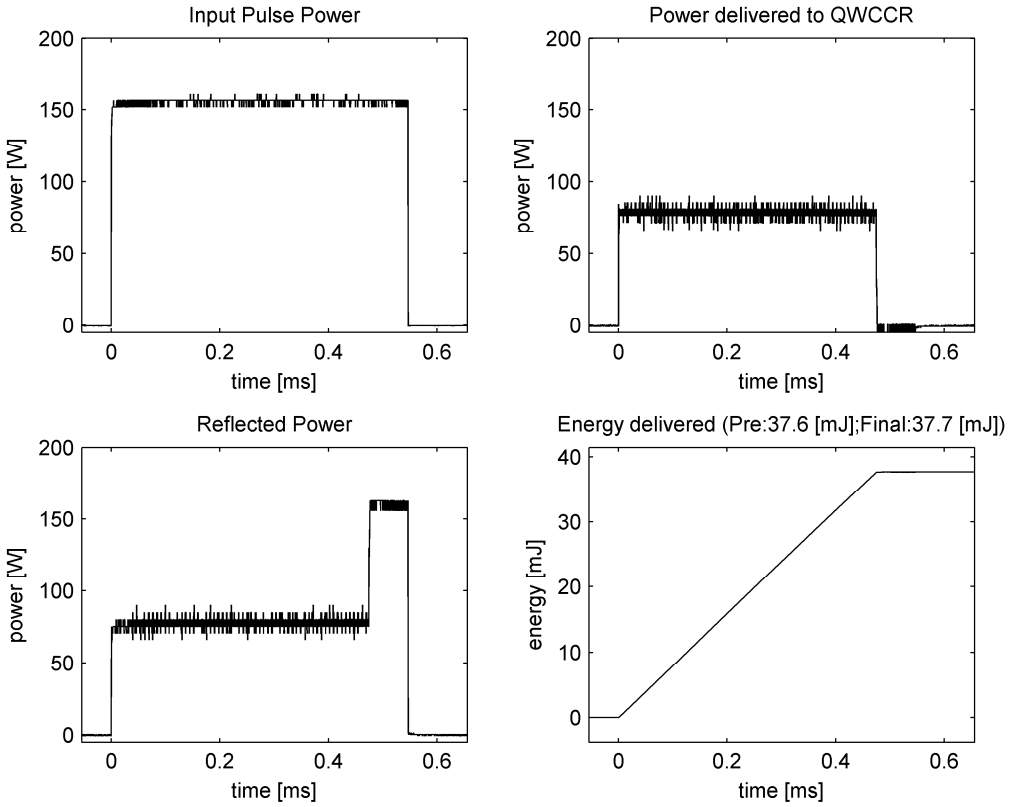

Fig. 36 QWCCR, successful ignition of 3.5% LPG by volume

Table 4 Test-32 data for 3.7% LPG

Pre Mix Temperature	65.9	ºF
Final Temperature	65	ºF
Barometric Pressure	14.17	PSIA
Initial Gauge Pressure	0.00	PSIG
Final Gauge Pressure	0.54	PSIG
Fuel to Air Ratio	0.036	
Mixture Composition	3.5	% by Vol.
Input Pulse Average Power	155	Watt
Pulse Length	0.548	ms
Pulse Energy	84.9	mJ
Energy Delivered	37.7	mJ
Trigger Count	2	

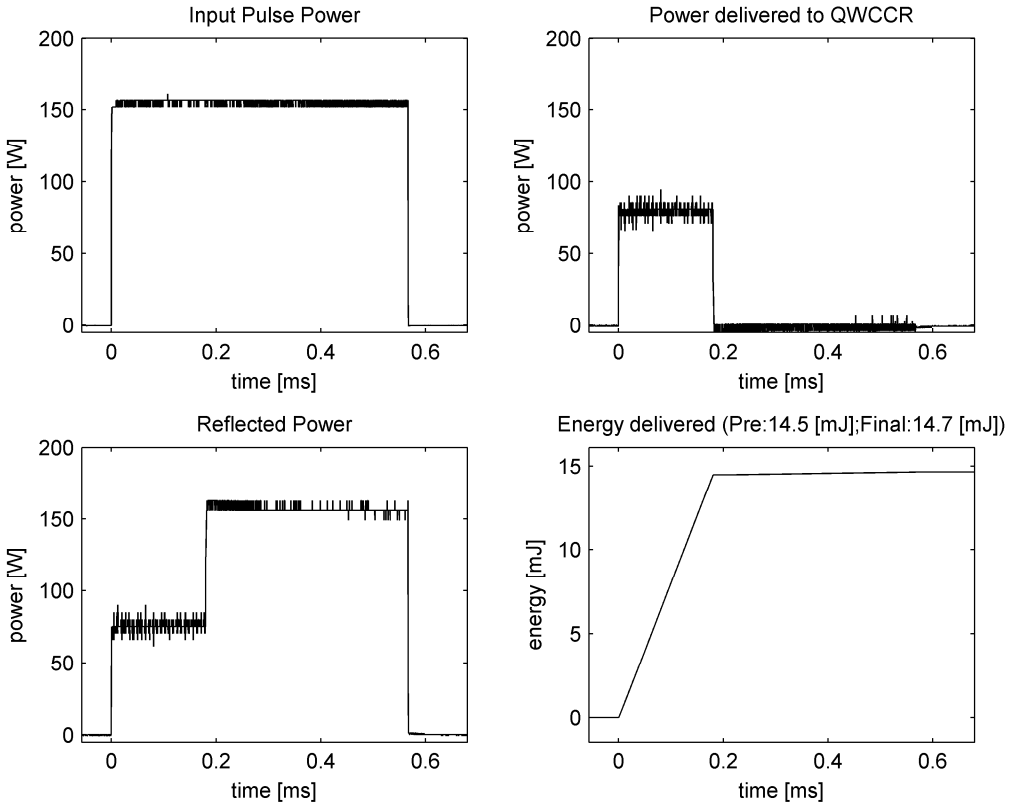

Fig. 37 QWCCR, successful ignition of 3.7% LPG by volume

Table 5 Test-33 data for 3.7% LPG

Pre Mix Temperature	66.3	ºF
Final Temperature	65.2	ºF
Barometric Pressure	14.17	PSIA
Initial Gauge Pressure	0.00	PSIG
Final Gauge Pressure	0.58	PSIG
Fuel to Air Ratio	0.039	
Mixture Composition	3.7	% by Vol.
Input Pulse Average Power	155	Watt
Pulse Length	0.568	ms
Pulse Energy	88.0	mJ
Energy Delivered	14.7	mJ
Trigger Count	3	

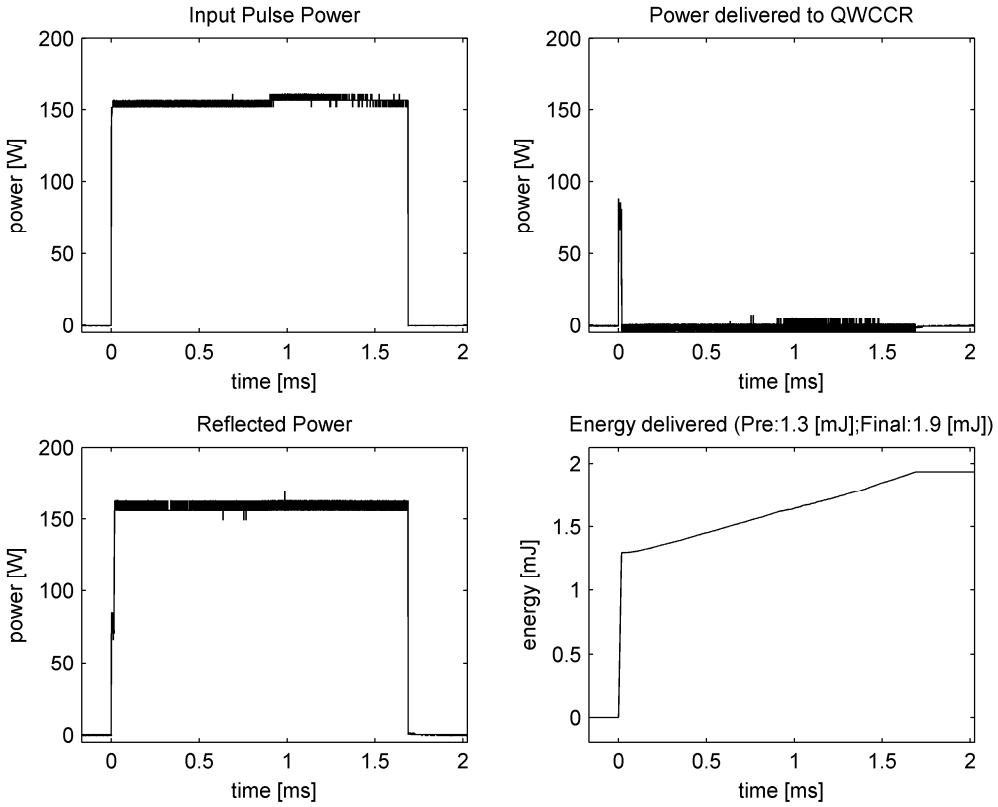

Fig. 38 QWCCR, successful ignition of 3.4% LPG by volume

Table 6 Test-34 data for 3.4% LPG

Pre Mix Temperature	66.5	ºF
Final Temperature	66	ºF
Barometric Pressure	14.16	PSIA
Initial Gauge Pressure	0.00	PSIG
Final Gauge Pressure	0.52	PSIG
Fuel to Air Ratio	0.036	
Mixture Composition	3.4	% by Vol.
Input Pulse Average Power	156	Watt
Pulse Length	1.688	ms
Pulse Energy	263.3	mJ
Energy Delivered	1.9	mJ
Trigger Count	5	

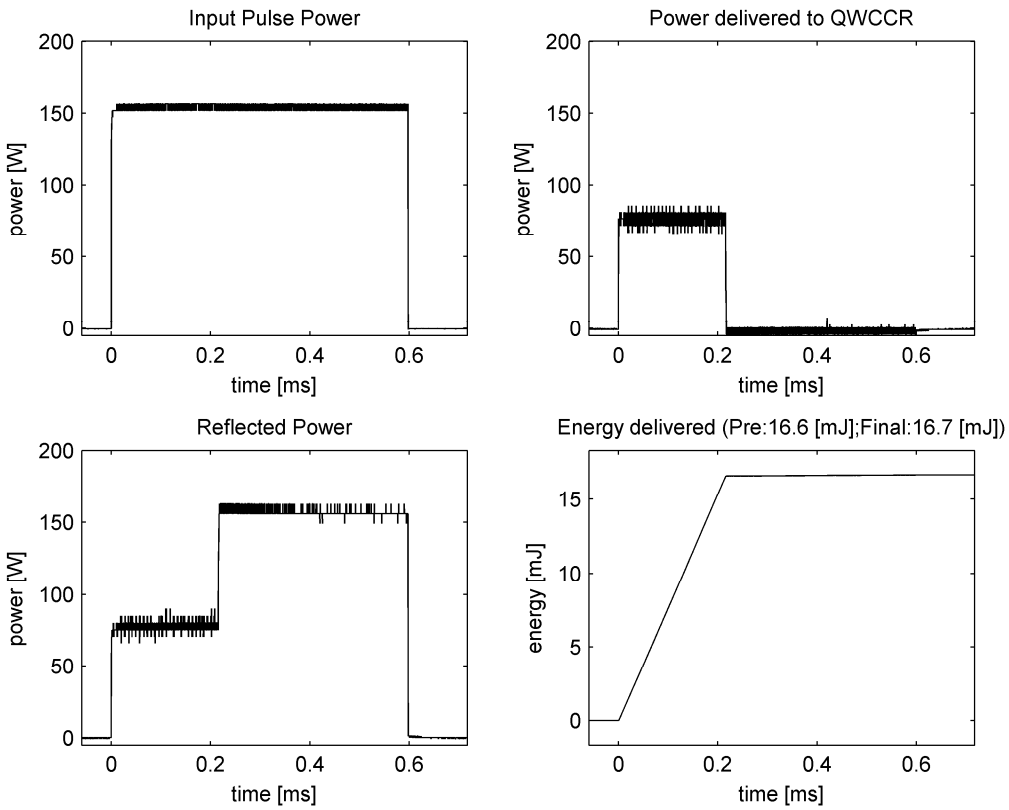

Fig. 39 QWCCR, successful ignition of 3.8% LPG by volume

Table 7 Test-35 data for 3.8% LPG

Pre Mix Temperature	67.1	ºF
Final Temperature	66.6	ºF
Barometric Pressure	14.17	PSIA
Initial Gauge Pressure	0.00	PSIG
Final Gauge Pressure	0.58	PSIG
Fuel to Air Ratio	0.039	
Mixture Composition	3.8	% by Vol.
Input Pulse Average Power	153	Watt
Pulse Length	0.599	ms
Pulse Energy	91.6	mJ
Energy Delivered	16.7	mJ
Trigger Count	10	

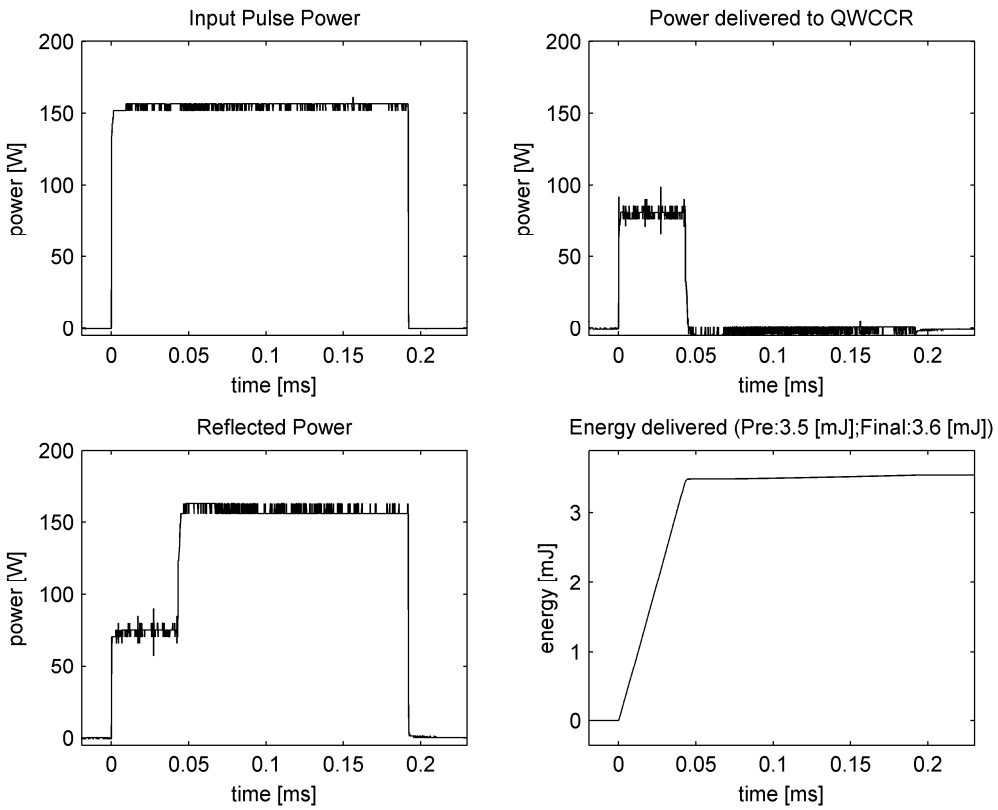

Fig. 40 QWCCR, successful ignition of 5.4% LPG by volume

Table 8 Test-36 data for 5.4% LPG

Pre Mix Temperature	66.2	ºF
Final Temperature	66.2	ºF
Barometric Pressure	14.17	PSIA
Initial Gauge Pressure	0.00	PSIG
Final Gauge Pressure	0.82	PSIG
Fuel to Air Ratio	0.057	
Mixture Composition	5.4	% by Vol.
Input Pulse Average Power	153	Watt
Pulse Length	0.193	ms
Pulse Energy	29.5	mJ
Energy Delivered	3.6	mJ
Trigger Count	1	

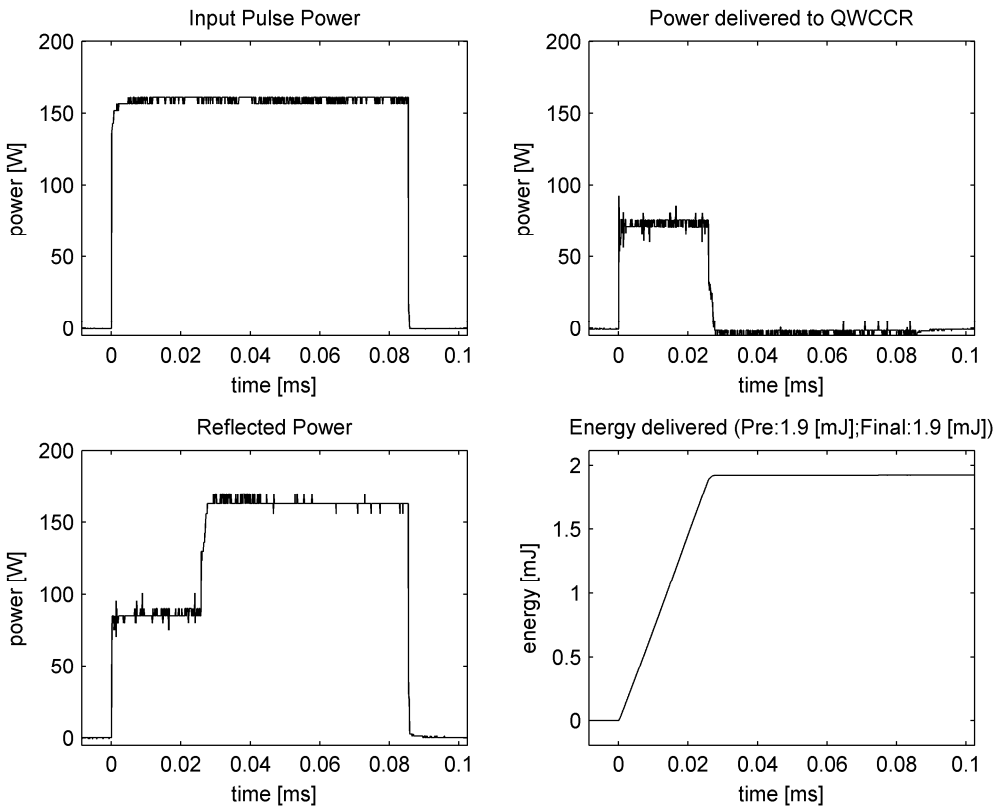

Fig. 41 QWCCR, successful ignition of 5.6% LPG by volume

Table 9 Test-37 data for 5.6% LPG

Pre Mix Temperature	66.2	ºF
Final Temperature	66.2	ºF
Barometric Pressure	14.17	PSIA
Initial Gauge Pressure	0.00	PSIG
Final Gauge Pressure	0.84	PSIG
Fuel to Air Ratio	0.059	
Mixture Composition	5.6	% by Vol.
Input Pulse Average Power	155	Watt
Pulse Length	0.087	ms
Pulse Energy	13.5	mJ
Energy Delivered	1.9	mJ
Trigger Count	4	

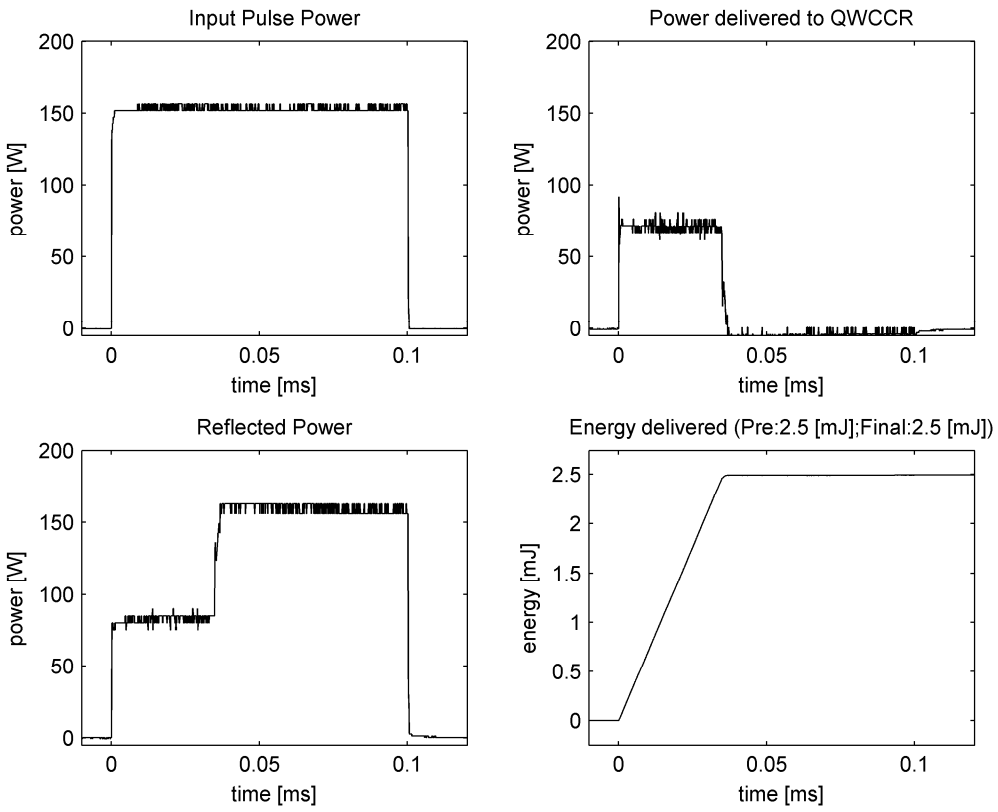

Fig. 42 QWCCR, successful ignition of 4.4% LPG by volume

Table 10 Test-38 data for 4.4% LPG

Pre Mix Temperature	68.9	ºF
Final Temperature	68.3	ºF
Barometric Pressure	14.17	PSIA
Initial Gauge Pressure	0.00	PSIG
Final Gauge Pressure	0.68	PSIG
Fuel to Air Ratio	0.046	
Mixture Composition	4.4	% by Vol.
Input Pulse Average Power	150	Watt
Pulse Length	0.102	ms
Pulse Energy	15.3	mJ
Energy Delivered	2.5	mJ
Trigger Count	2	

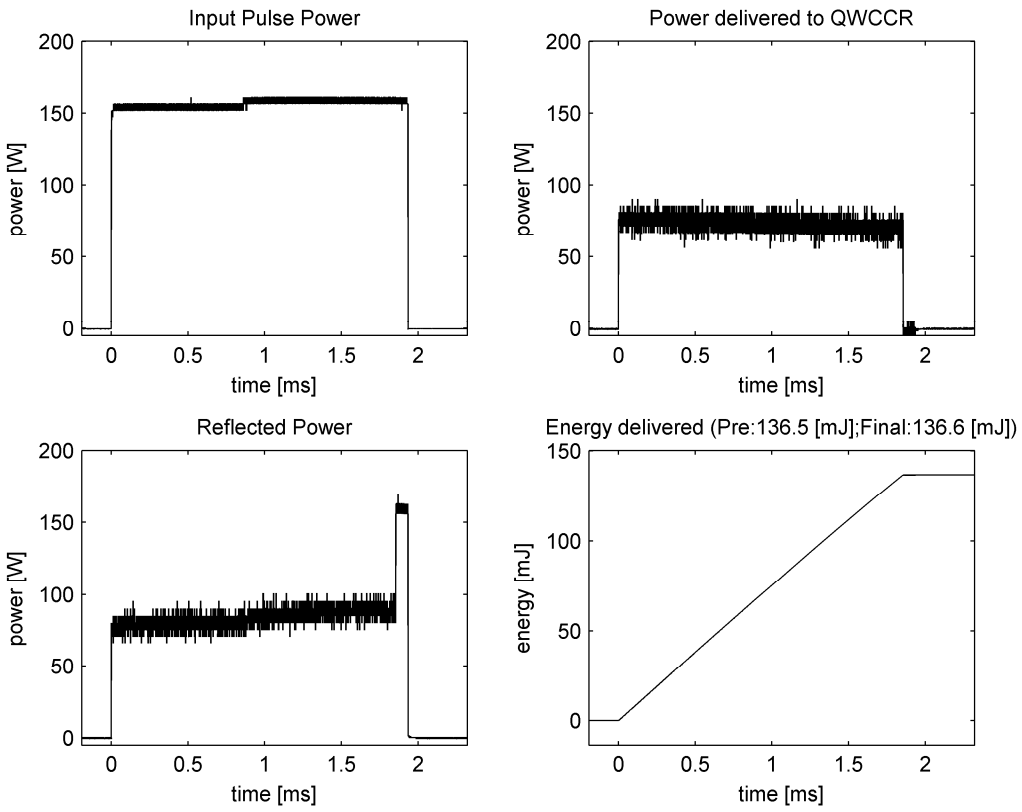

Fig. 43 QWCCR, successful ignition of 4.0% LPG by volume

Table 11 Test-39 data for 4.0% LPG

Pre Mix Temperature	70	ºF
Final Temperature	69.1	ºF
Barometric Pressure	14.17	PSIA
Initial Gauge Pressure	0.00	PSIG
Final Gauge Pressure	0.62	PSIG
Fuel to Air Ratio	0.042	
Mixture Composition	4.0	% by Vol.
Input Pulse Average Power	157	Watt
Pulse Length	1.935	ms
Pulse Energy	303.8	mJ
Energy Delivered	136.6	mJ
Trigger Count	2	

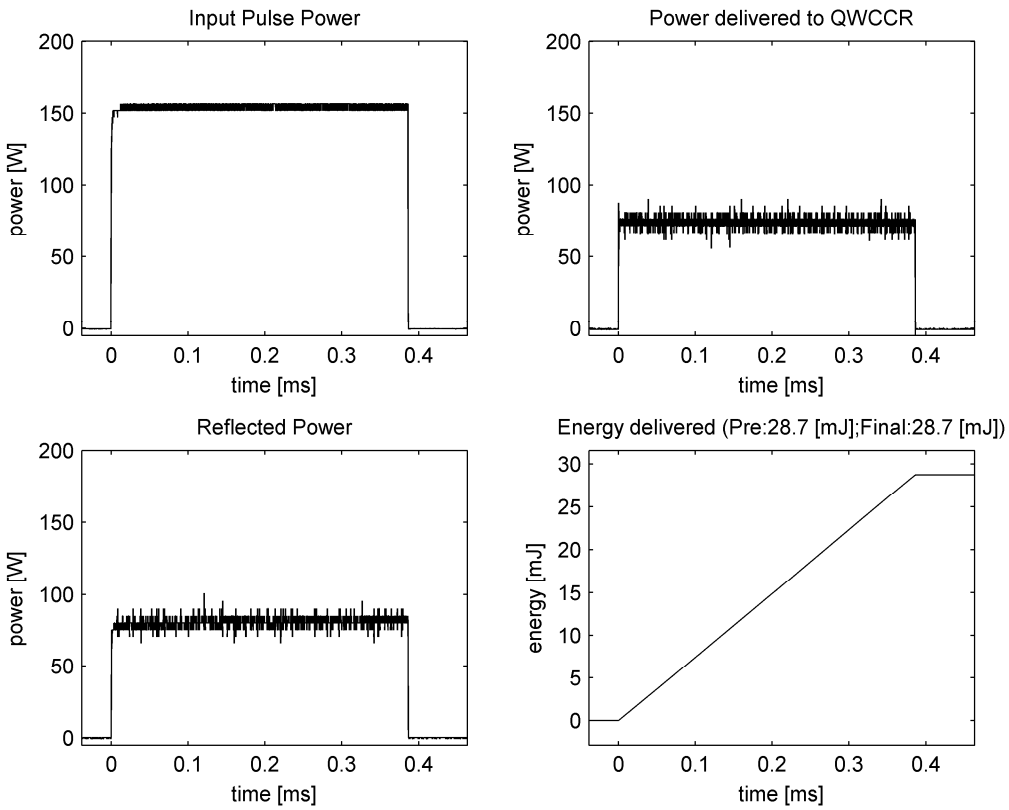

Fig. 44 QWCCR, successful ignition of 7.5% LPG by volume

Table 12 Test-40 data for 7.5% LPG

Pre Mix Temperature	69.5	ºF
Final Temperature	68.9	ºF
Barometric Pressure	14.17	PSIA
Initial Gauge Pressure	0.00	PSIG
Final Gauge Pressure	1.17	PSIG
Fuel to Air Ratio	0.081	
Mixture Composition	7.5	% by Vol.
Input Pulse Average Power	154	Watt
Pulse Length	0.388	ms
Pulse Energy	59.8	mJ
Energy Delivered	28.7	mJ
Trigger Count	6	

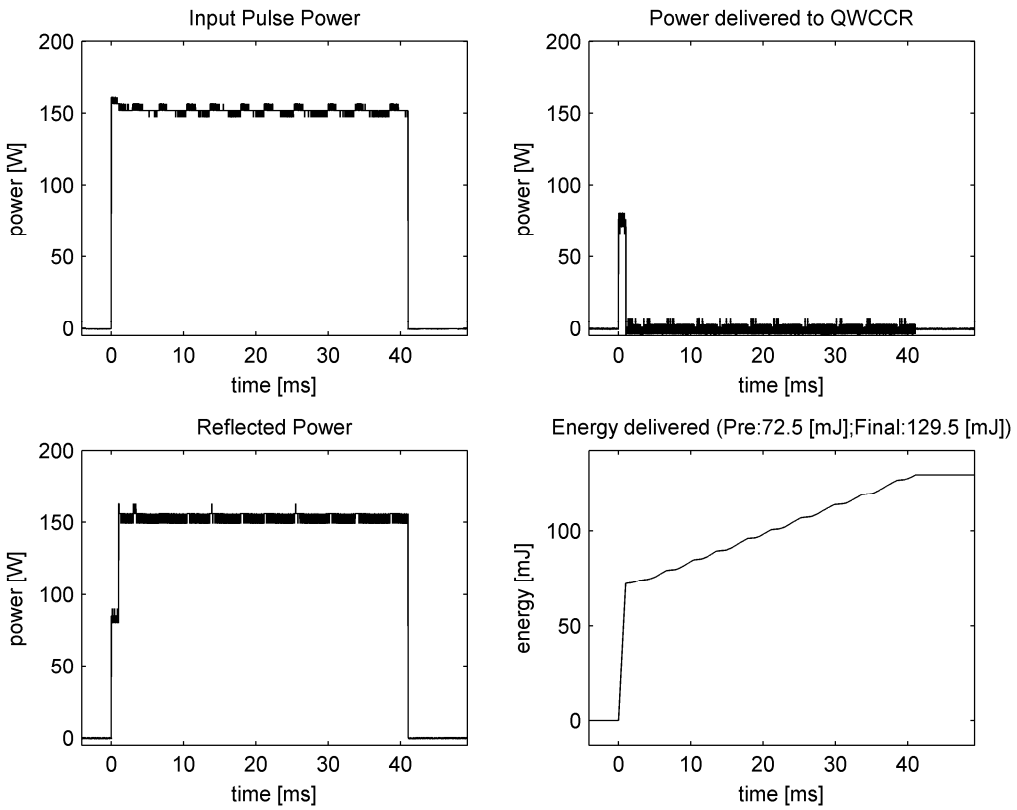

Fig. 45 QWCCR, unsuccessful attempt of 3.0% LPG by volume

Table 13 Test-41 data for 3.0% LPG

Pre Mix Temperature	68.3	ºF
Final Temperature	68.3	ºF
Barometric Pressure	14.18	PSIA
Initial Gauge Pressure	0.00	PSIG
Final Gauge Pressure	0.45	PSIG
Fuel to Air Ratio	0.031	
Mixture Composition	3.0	% by Vol.
Input Pulse Average Power	152	Watt
Pulse Length	41.052	ms
Pulse Energy	6239.9	mJ
Energy Delivered	129.5	mJ
Trigger Count	10	

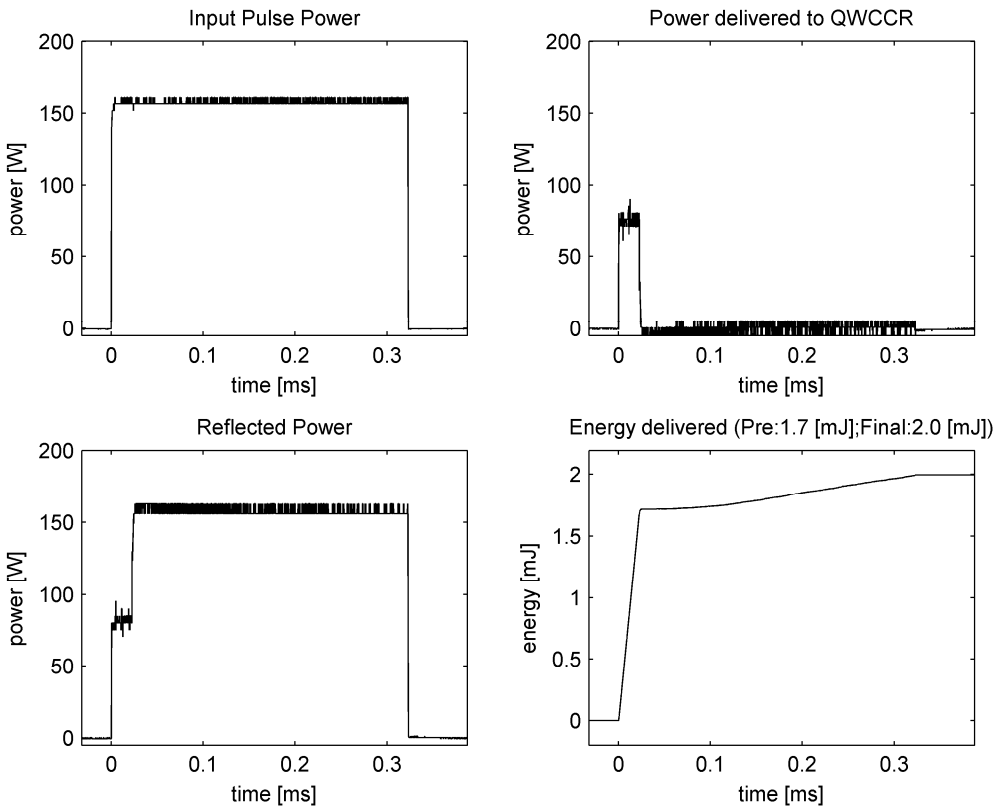

Fig. 46 QWCCR, successful ignition of 3.9% LPG by volume

Table 14 Test-42 data for 3.9% LPG

Pre Mix Temperature	66.1	ºF
Final Temperature	66.1	ºF
Barometric Pressure	14.19	PSIA
Initial Gauge Pressure	0.00	PSIG
Final Gauge Pressure	0.58	PSIG
Fuel to Air Ratio	0.040	
Mixture Composition	3.9	% by Vol.
Input Pulse Average Power	156	Watt
Pulse Length	0.325	ms
Pulse Energy	50.7	mJ
Energy Delivered	2.0	mJ
Trigger Count	2	

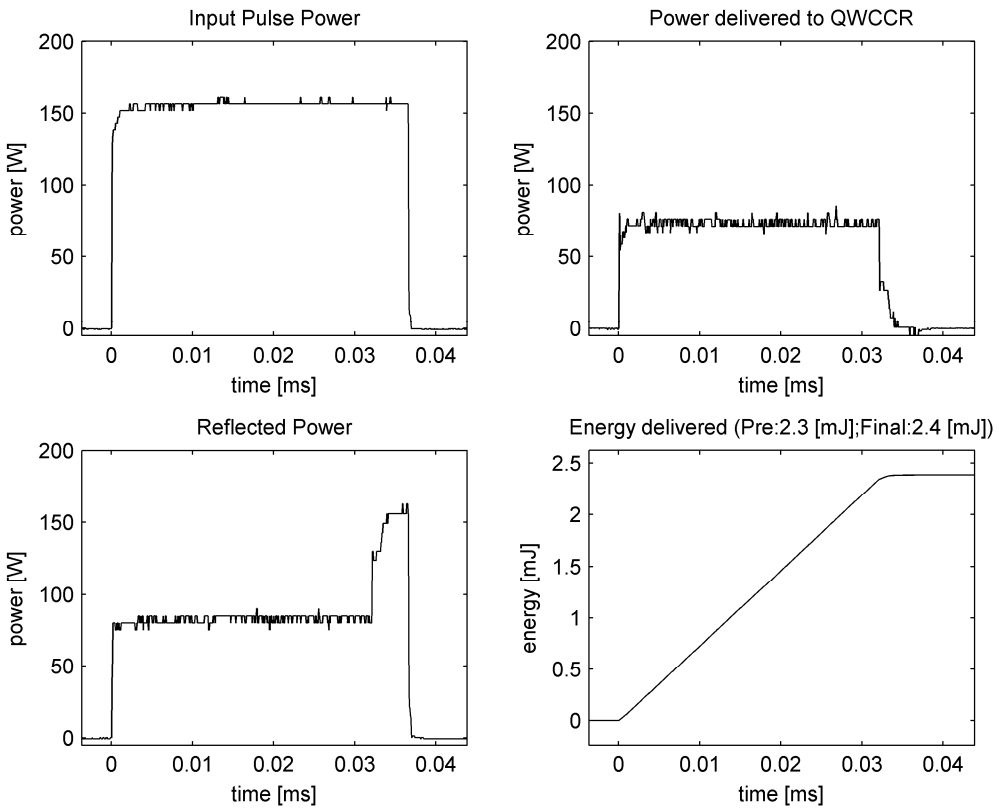

Fig. 47 QWCCR, successful ignition of 6.2% LPG by volume

Table 15 Test-43 data for 6.2% LPG

Pre Mix Temperature	69.1	ºF
Final Temperature	68.3	ºF
Barometric Pressure	14.20	PSIA
Initial Gauge Pressure	0.00	PSIG
Final Gauge Pressure	0.96	PSIG
Fuel to Air Ratio	0.066	
Mixture Composition	6.2	% by Vol.
Input Pulse Average Power	147	Watt
Pulse Length	0.038	ms
Pulse Energy	5.6	mJ
Energy Delivered	2.4	mJ
Trigger Count	2	

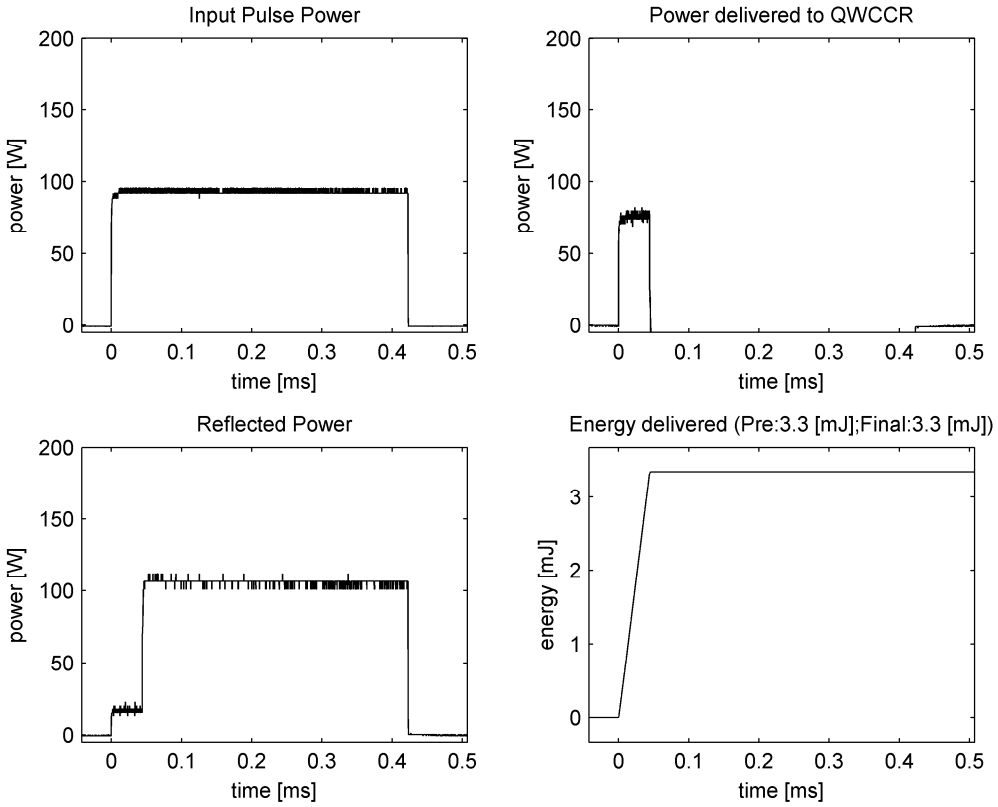

Fig. 48 QWCCR, successful ignition of 3.8% LPG by volume

Table 16 Test-44 data for 3.8% LPG

Pre Mix Temperature	62.4	ºF
Final Temperature	62.2	ºF
Barometric Pressure	14.31	PSIA
Initial Gauge Pressure	0.01	PSIG
Final Gauge Pressure	0.58	PSIG
Fuel to Air Ratio	0.040	
Mixture Composition	3.8	% by Vol.
Input Pulse Average Power	92	Watt
Pulse Length	0.424	ms
Pulse Energy	39.0	mJ
Energy Delivered	3.3	mJ
Trigger Count	2	

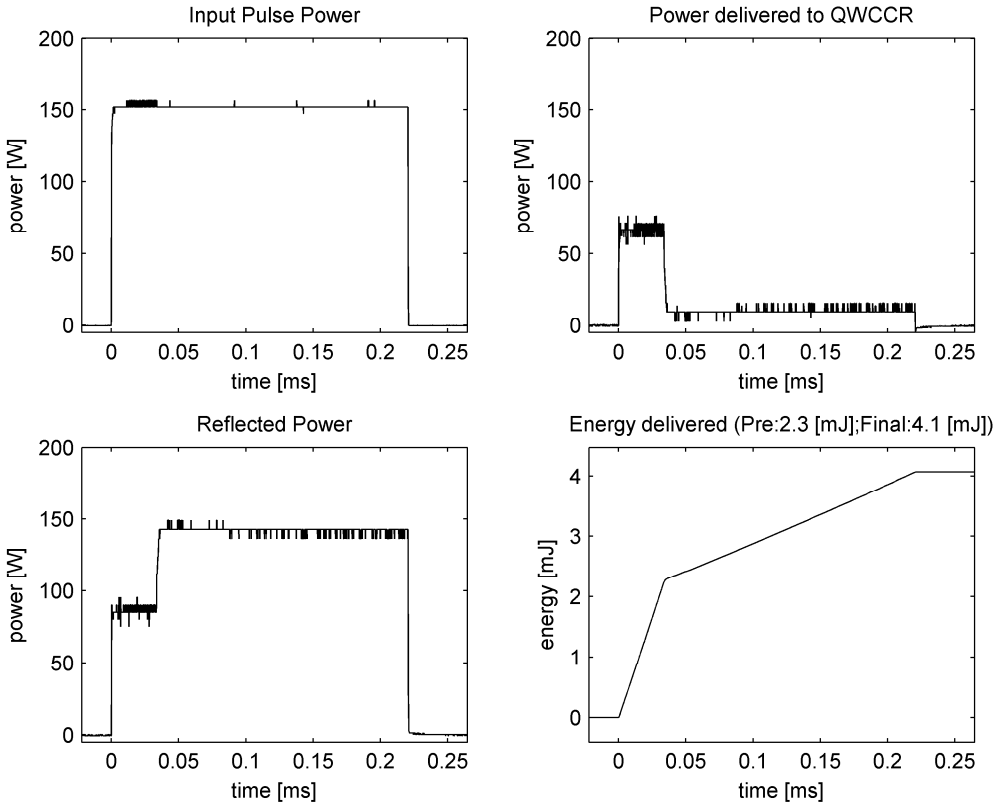

Fig. 49 QWCCR, successful ignition of 4.5% LPG by volume

Table 17 Test-45 data for 4.5% LPG

Pre Mix Temperature	64.4	ºF
Final Temperature	62.8	ºF
Barometric Pressure	14.31	PSIA
Initial Gauge Pressure	0.00	PSIG
Final Gauge Pressure	0.72	PSIG
Fuel to Air Ratio	0.047	
Mixture Composition	4.5	% by Vol.
Input Pulse Average Power	151	Watt
Pulse Length	0.222	ms
Pulse Energy	33.5	mJ
Energy Delivered	4.1	mJ
Trigger Count	1	

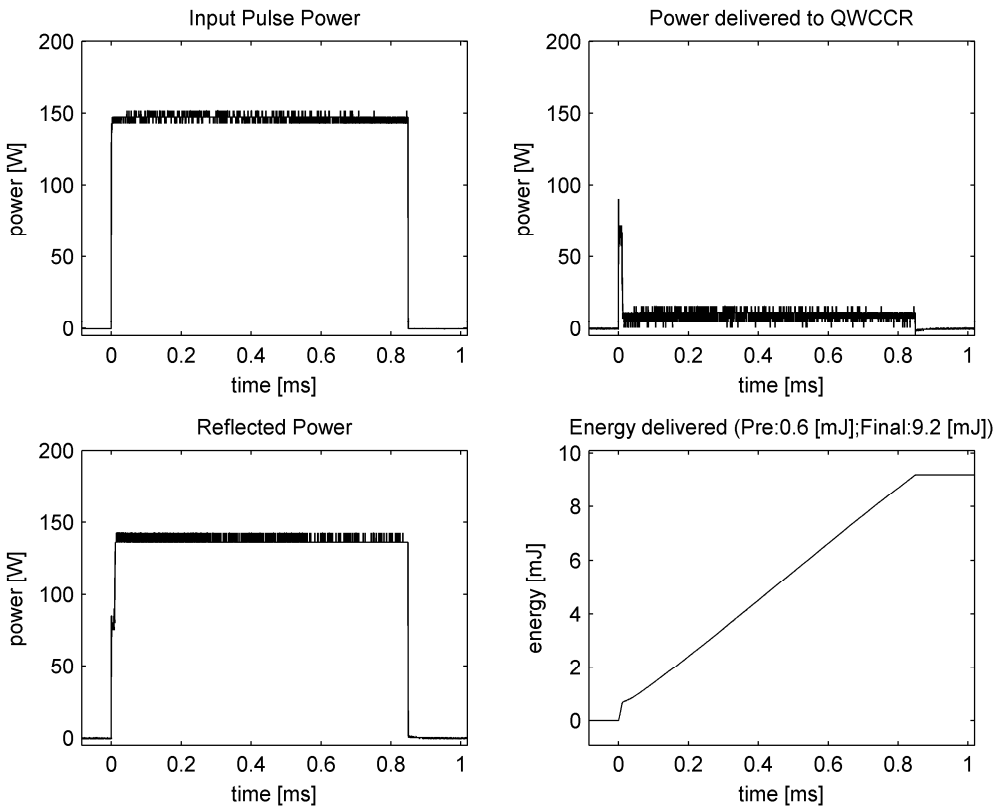

Fig. 50 QWCCR, successful ignition of 3.5% LPG by volume

Table 18 Test-46 data for 3.5% LPG

Pre Mix Temperature	64.6	ºF
Final Temperature	64.1	ºF
Barometric Pressure	14.31	PSIA
Initial Gauge Pressure	0.00	PSIG
Final Gauge Pressure	0.53	PSIG
Fuel to Air Ratio	0.036	
Mixture Composition	3.5	% by Vol.
Input Pulse Average Power	147	Watt
Pulse Length	0.85	ms
Pulse Energy	125.0	mJ
Energy Delivered	9.2	mJ
Trigger Count	1	

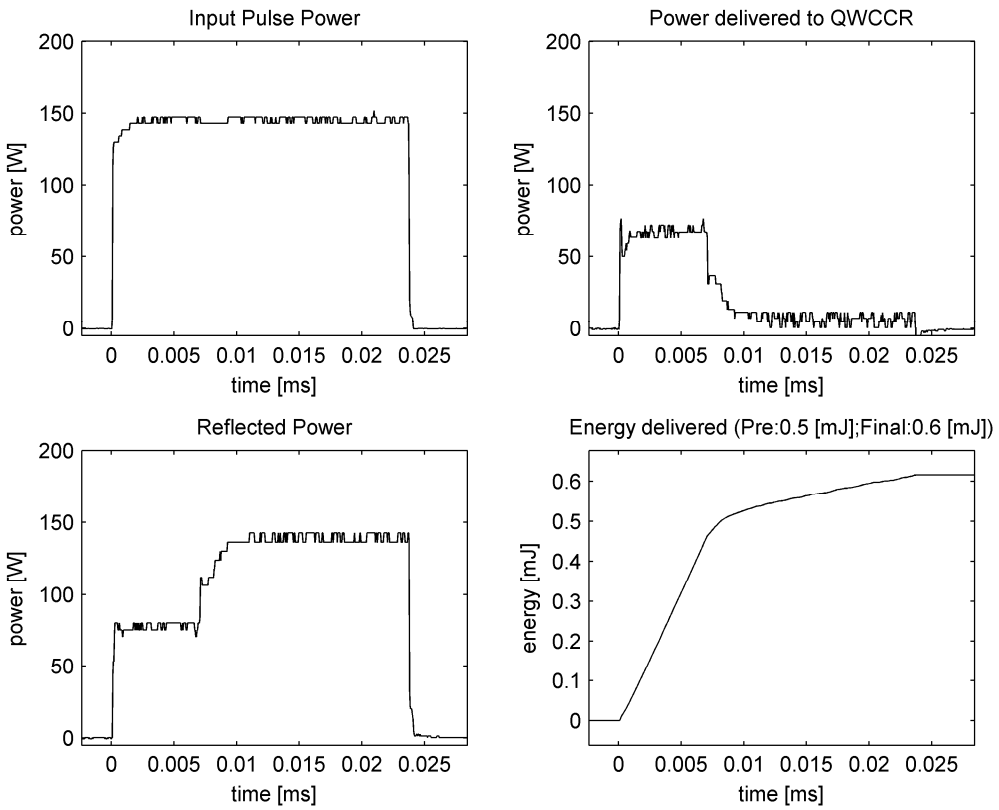

Fig. 51 QWCCR, successful ignition of 6.9% LPG by volume

Table 19 Test-47 data for 6.9% LPG

Pre Mix Temperature	63.6	ºF
Final Temperature	63.5	ºF
Barometric Pressure	14.29	PSIA
Initial Gauge Pressure	0.00	PSIG
Final Gauge Pressure	1.06	PSIG
Fuel to Air Ratio	0.074	
Mixture Composition	6.9	% by Vol.
Input Pulse Average Power	132	Watt
Pulse Length	0.025	ms
Pulse Energy	3.3	mJ
Energy Delivered	0.6	mJ
Trigger Count	2	

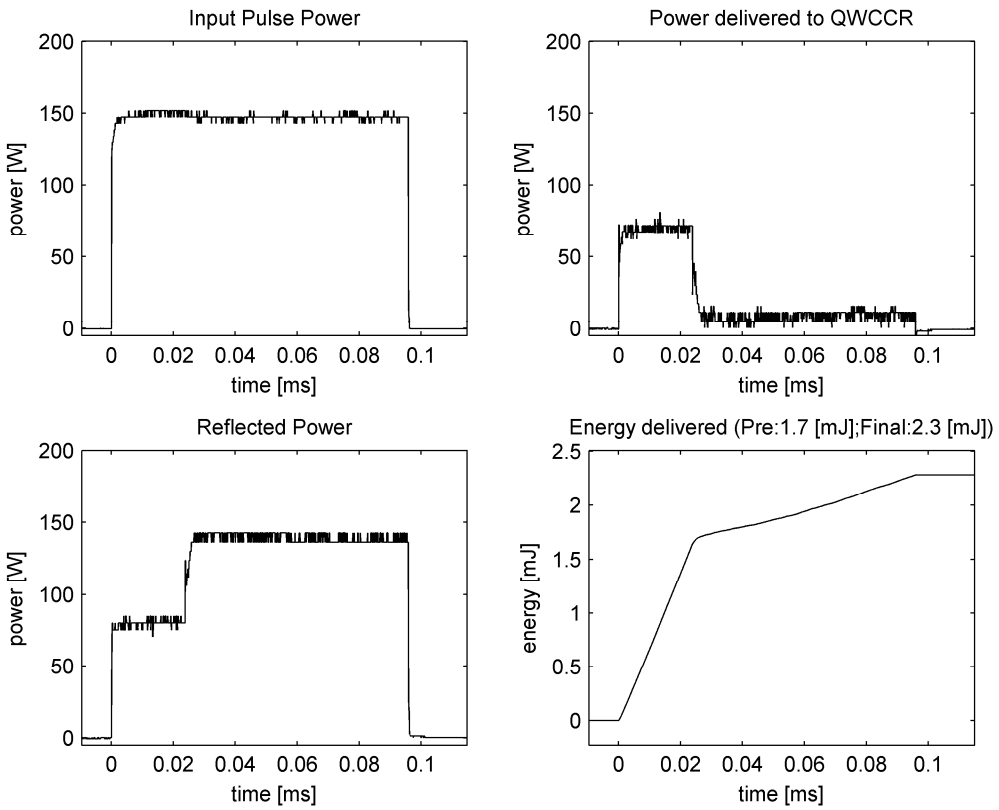

Fig. 52 QWCCR, successful ignition of 4.2% LPG by volume

Table 20 Test-48 data for 4.2% LPG

Pre Mix Temperature	65.8	ºF
Final Temperature	64.8	ºF
Barometric Pressure	14.29	PSIA
Initial Gauge Pressure	0.00	PSIG
Final Gauge Pressure	0.66	PSIG
Fuel to Air Ratio	0.044	
Mixture Composition	4.2	% by Vol.
Input Pulse Average Power	144	Watt
Pulse Length	0.098	ms
Pulse Energy	14.1	mJ
Energy Delivered	2.3	mJ
Trigger Count	1	

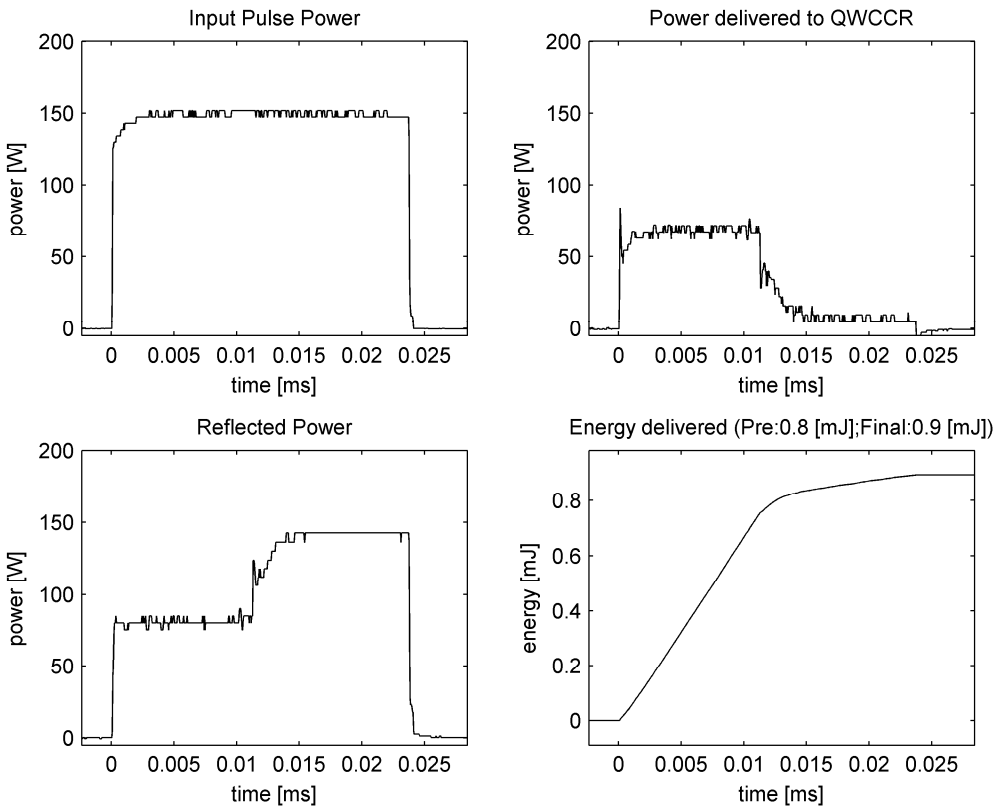

Fig. 53 QWCCR, successful ignition of 5.0% LPG by volume

Table 21 Test-49 data for 5.0% LPG

Pre Mix Temperature	66.7	ºF
Final Temperature	66.1	ºF
Barometric Pressure	14.29	PSIA
Initial Gauge Pressure	0.00	PSIG
Final Gauge Pressure	0.77	PSIG
Fuel to Air Ratio	0.053	
Mixture Composition	5.0	% by Vol.
Input Pulse Average Power	136	Watt
Pulse Length	0.025	ms
Pulse Energy	3.4	mJ
Energy Delivered	0.9	mJ
Trigger Count	4	

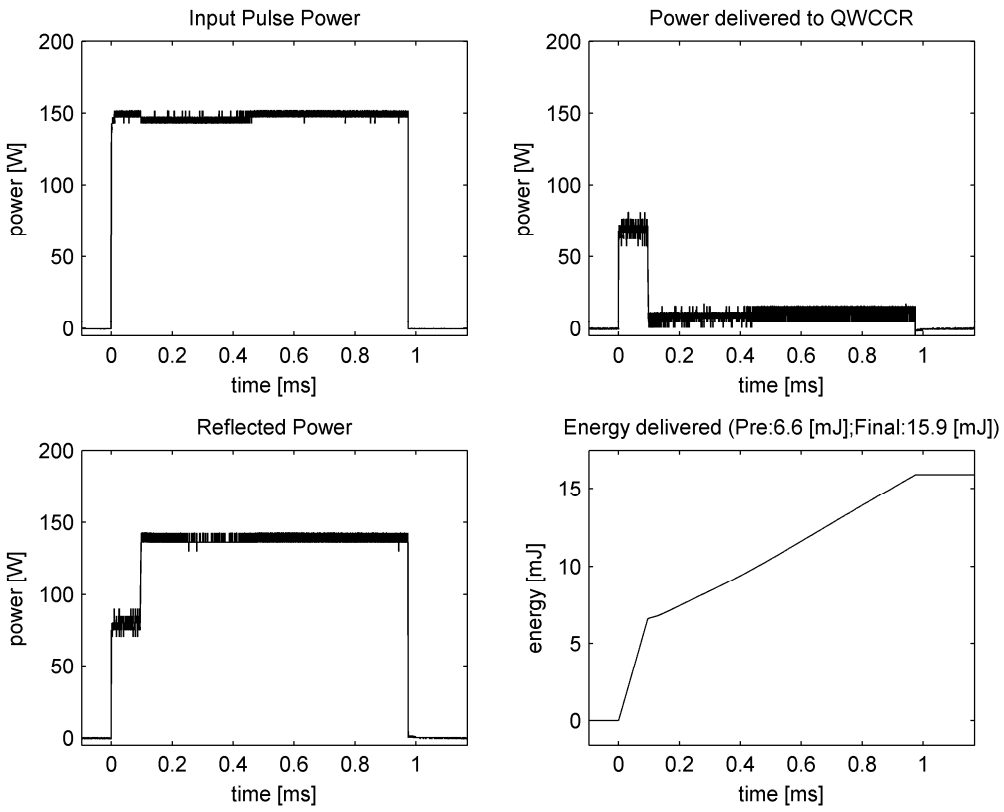

Fig. 54 QWCCR, successful ignition of 3.3% LPG by volume

Table 22 Test-50 data for 3.3% LPG

Pre Mix Temperature	67	ºF
Final Temperature	66.6	ºF
Barometric Pressure	14.29	PSIA
Initial Gauge Pressure	0.00	PSIG
Final Gauge Pressure	0.51	PSIG
Fuel to Air Ratio	0.035	
Mixture Composition	3.3	% by Vol.
Input Pulse Average Power	148	Watt
Pulse Length	0.975	ms
Pulse Energy	144.3	mJ
Energy Delivered	15.9	mJ
Trigger Count	1	

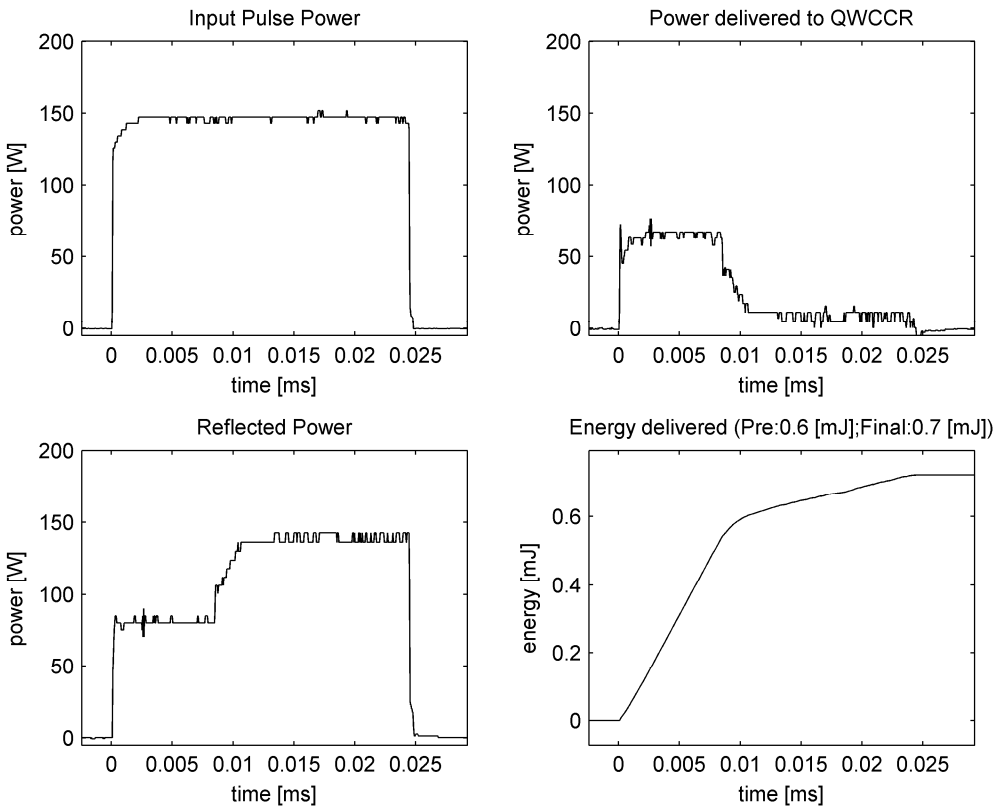

Fig. 55 QWCCR, successful ignition of 7.4% LPG by volume

Table 23 Test-51 data for 7.4% LPG

Pre Mix Temperature	66.4	ºF
Final Temperature	65.8	ºF
Barometric Pressure	14.29	PSIA
Initial Gauge Pressure	0.00	PSIG
Final Gauge Pressure	1.16	PSIG
Fuel to Air Ratio	0.080	
Mixture Composition	7.4	% by Vol.
Input Pulse Average Power	134	Watt
Pulse Length	0.026	ms
Pulse Energy	3.5	mJ
Energy Delivered	0.7	mJ
Trigger Count	2	

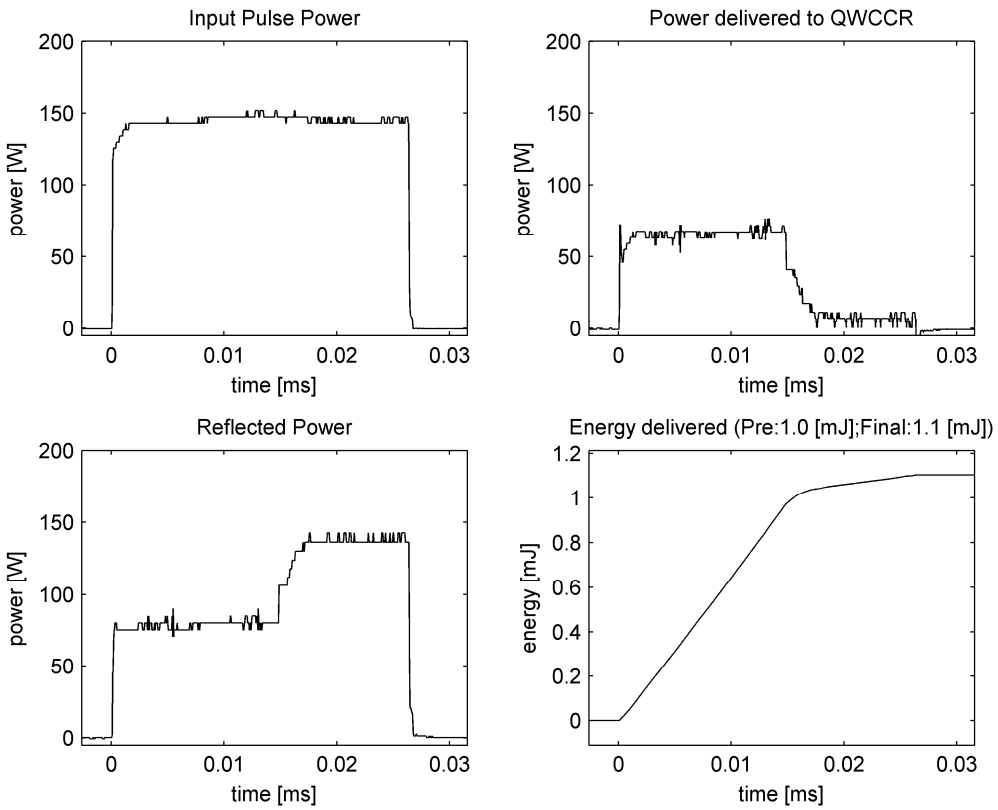

Fig. 56 QWCCR, successful ignition of 5.3% LPG by volume

Table 24 Test-52 data for 5.3% LPG

Pre Mix Temperature	67.3	ºF
Final Temperature	66.6	ºF
Barometric Pressure	14.29	PSIA
Initial Gauge Pressure	0.00	PSIG
Final Gauge Pressure	0.82	PSIG
Fuel to Air Ratio	0.056	
Mixture Composition	5.3	% by Vol.
Input Pulse Average Power	134	Watt
Pulse Length	0.028	ms
Pulse Energy	3.8	mJ
Energy Delivered	1.1	mJ
Trigger Count	1	

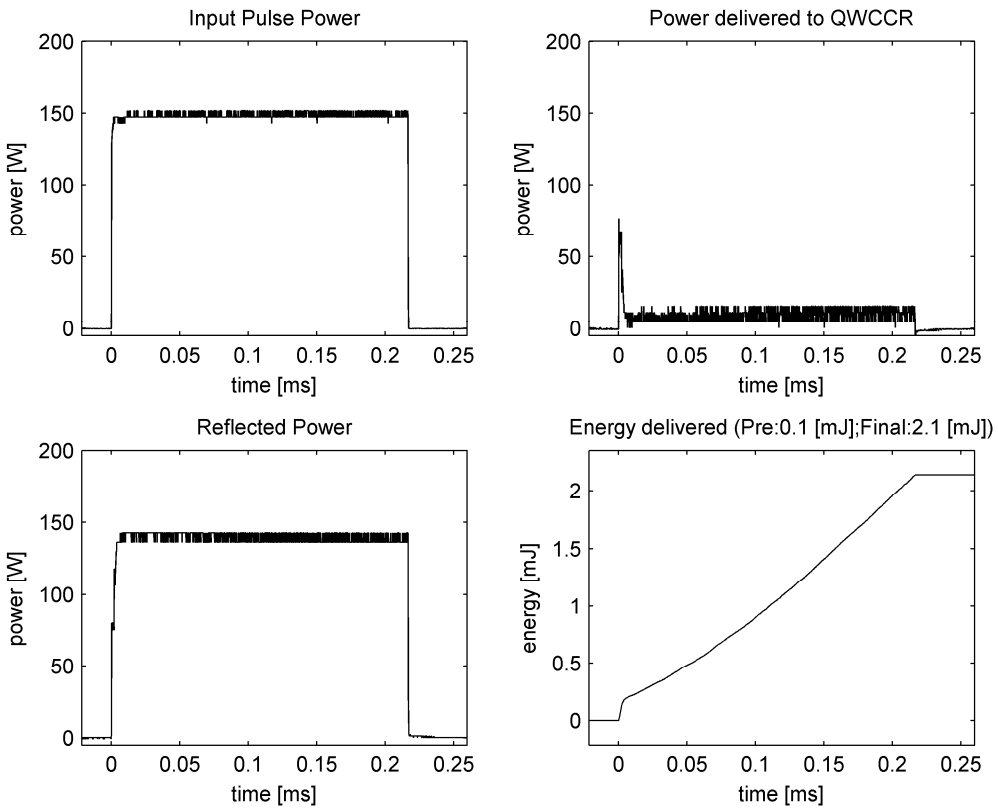

Fig. 57 QWCCR, successful ignition of 3.4% LPG by volume

Table 25 Test-53 data for 3.4% LPG

Pre Mix Temperature	70	ºF
Final Temperature	68.0	ºF
Barometric Pressure	14.29	PSIA
Initial Gauge Pressure	0.00	PSIG
Final Gauge Pressure	0.56	PSIG
Fuel to Air Ratio	0.035	
Mixture Composition	3.4	% by Vol.
Input Pulse Average Power	147	Watt
Pulse Length	0.218	ms
Pulse Energy	32.0	mJ
Energy Delivered	2.1	mJ
Trigger Count	3	

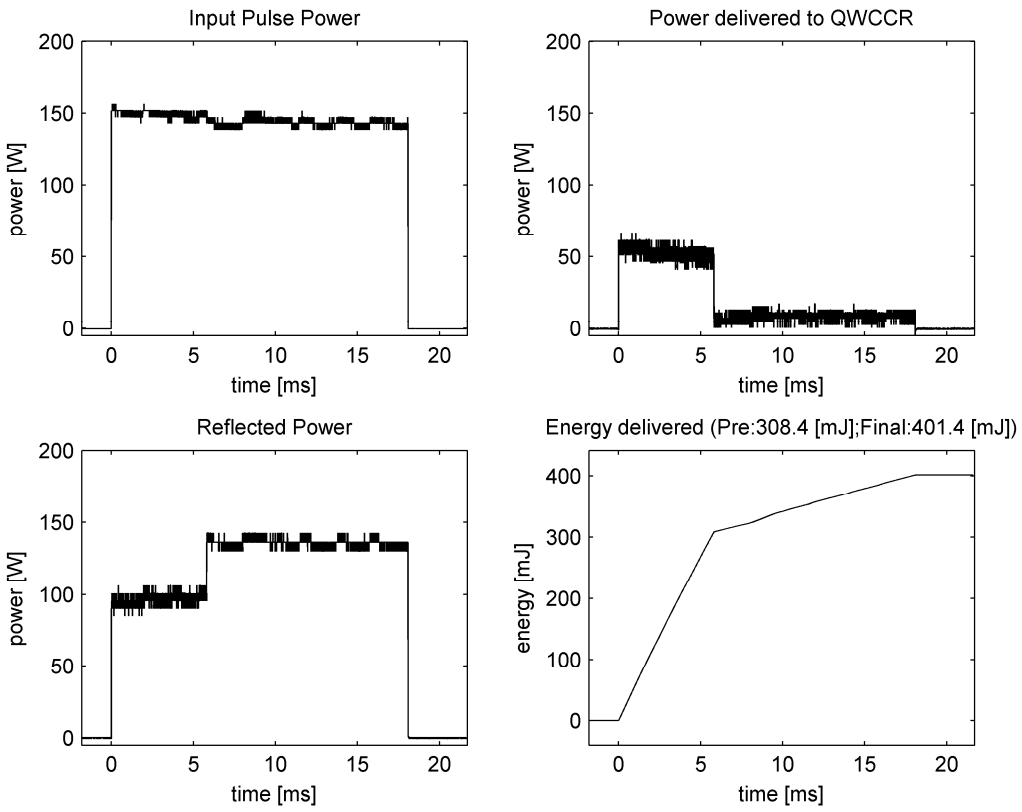

Fig. 58 QWCCR, unsuccessful ignition attempt of 3.0% LPG by volume

Table 26 Test-54 data for 3.0% LPG

Pre Mix Temperature	67.9	ºF
Final Temperature	68.1	ºF
Barometric Pressure	14.29	PSIA
Initial Gauge Pressure	0.00	PSIG
Final Gauge Pressure	0.45	PSIG
Fuel to Air Ratio	0.031	
Mixture Composition	3.0	% by Vol.
Input Pulse Average Power	146	Watt
Pulse Length	18.08	ms
Pulse Energy	2640	mJ
Energy Delivered	401.4	mJ
Trigger Count	10	

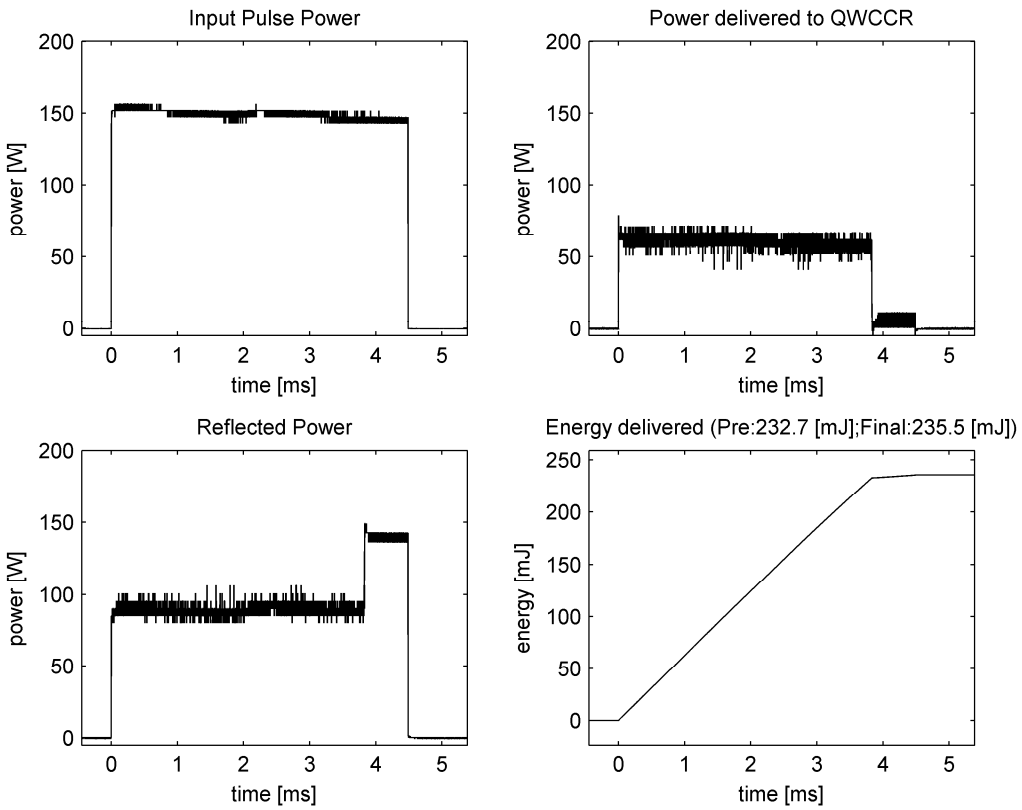

Fig. 59 QWCCR, successful ignition of 3.7% LPG by volume

Table 27 Test-55 data for 3.7% LPG

Pre Mix Temperature	66.2	ºF
Final Temperature	66.3	ºF
Barometric Pressure	14.28	PSIA
Initial Gauge Pressure	0.00	PSIG
Final Gauge Pressure	0.55	PSIG
Fuel to Air Ratio	0.039	
Mixture Composition	3.7	% by Vol.
Input Pulse Average Power	149	Watt
Pulse Length	4.49	ms
Pulse Energy	669.0	mJ
Energy Delivered	235.5	mJ
Trigger Count	2	

A.2 SPARK PLUG IGNITION TEST DATA

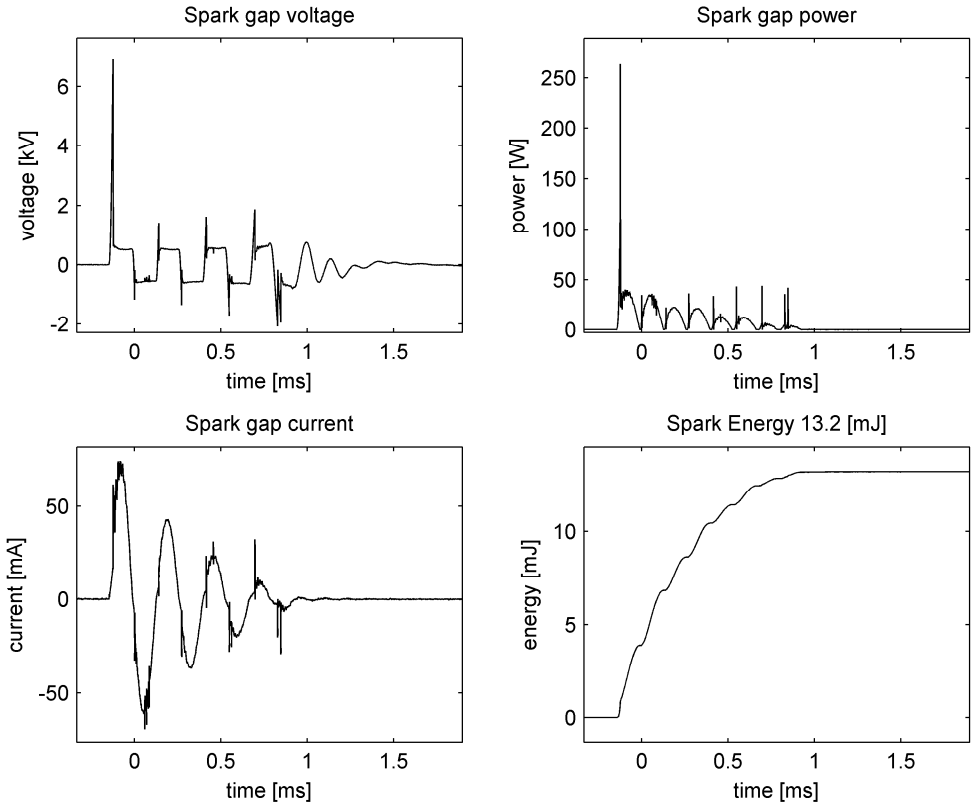

Fig. 60 Spark, successful ignition of 3.9% LPG by volume

Table 28 Test-10 data for 3.9% LPG

Pre Mix Temperature	70.1	ºF
Final Temperature	70.2	ºF
Barometric Pressure	14.06	PSIA
Initial Gauge Pressure	0.00	PSIG
Final Gauge Pressure	0.57	PSIG
Fuel to Air Ratio	0.040	
Mixture Composition	3.9	% by Vol.
Capacitor Value	1.487	µF
Capacitor Voltage	260	V
Capacitor Energy	50.3	mJ
Spark Energy	13.2	mJ
Trigger Count	4	

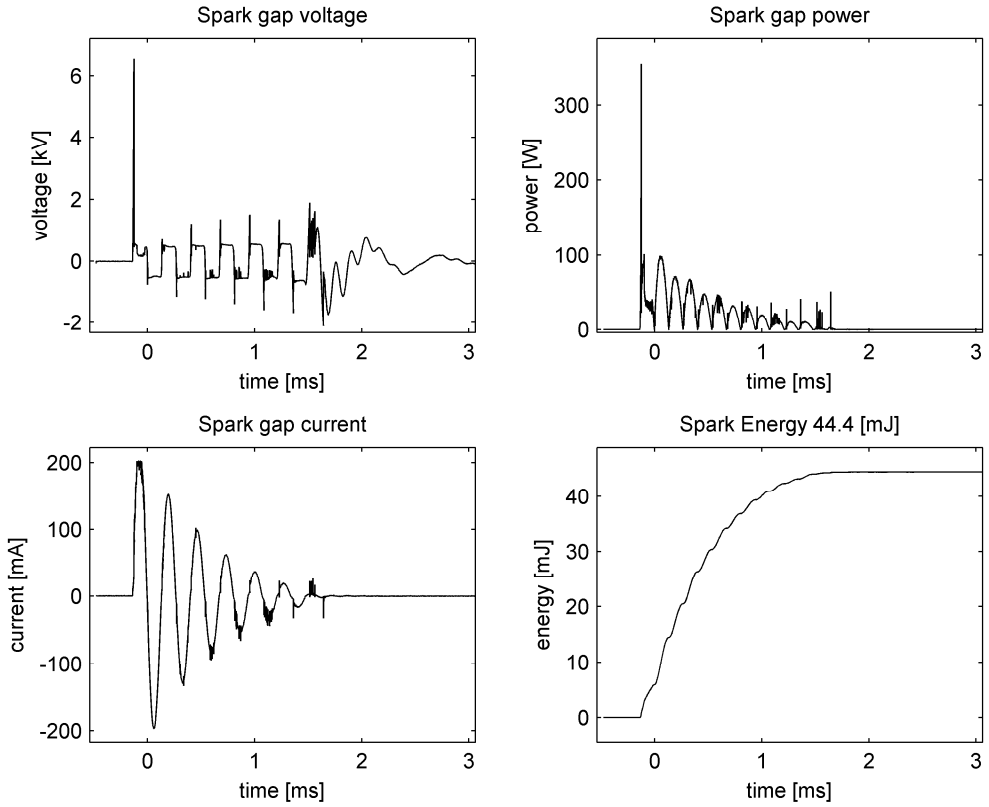

Fig. 61 Spark, unsuccessful attempt of 3.4% LPG by volume

Table 29 Test-11 data for 3.4% LPG

Pre Mix Temperature	70.3	ºF
Final Temperature	70.2	ºF
Barometric Pressure	14.07	PSIA
Initial Gauge Pressure	0.00	PSIG
Final Gauge Pressure	0.50	PSIG
Fuel to Air Ratio	0.035	
Mixture Composition	3.4	% by Vol.
Capacitor Value	1.487	µF
Capacitor Voltage	840	V
Capacitor Energy	524.6	mJ
Spark Energy	44.4	mJ
Trigger Count	10	

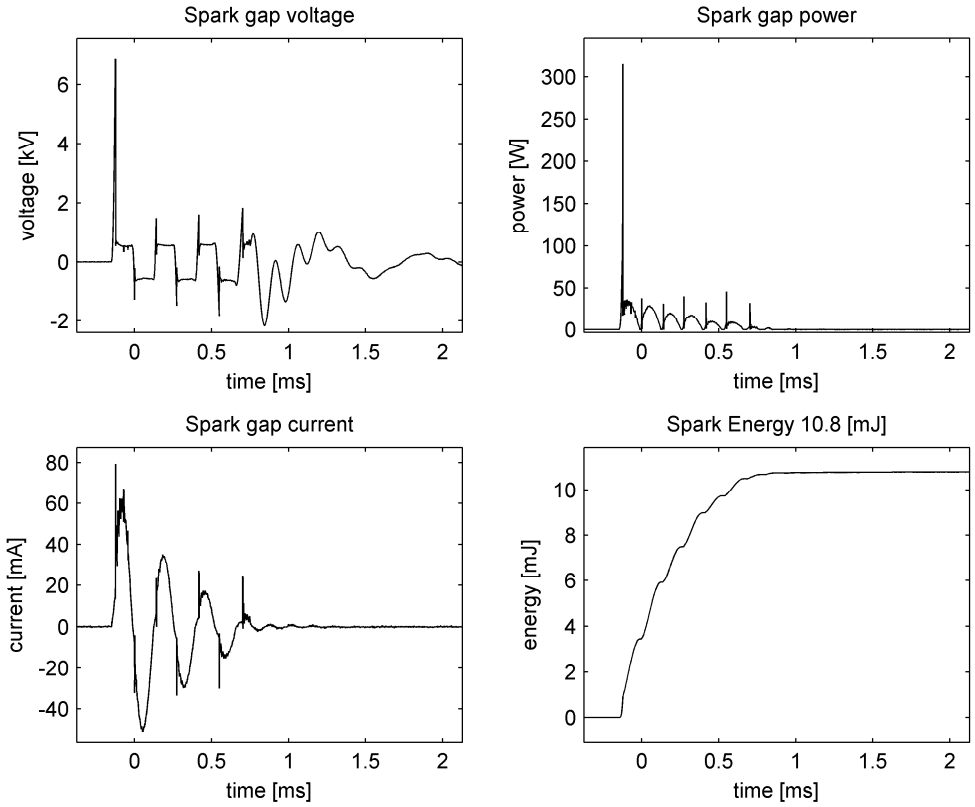

Fig. 62 Spark, successful ignition of 3.9% LPG by volume

Table 30 Test-12 data for 3.9% LPG

Pre Mix Temperature	69.5	ºF
Final Temperature	69.2	ºF
Barometric Pressure	14.06	PSIA
Initial Gauge Pressure	0.00	PSIG
Final Gauge Pressure	0.58	PSIG
Fuel to Air Ratio	0.040	
Mixture Composition	3.9	% by Vol.
Capacitor Value	1.487	µF
Capacitor Voltage	220	V
Capacitor Energy	36.0	mJ
Spark Energy	10.8	mJ
Trigger Count	3	

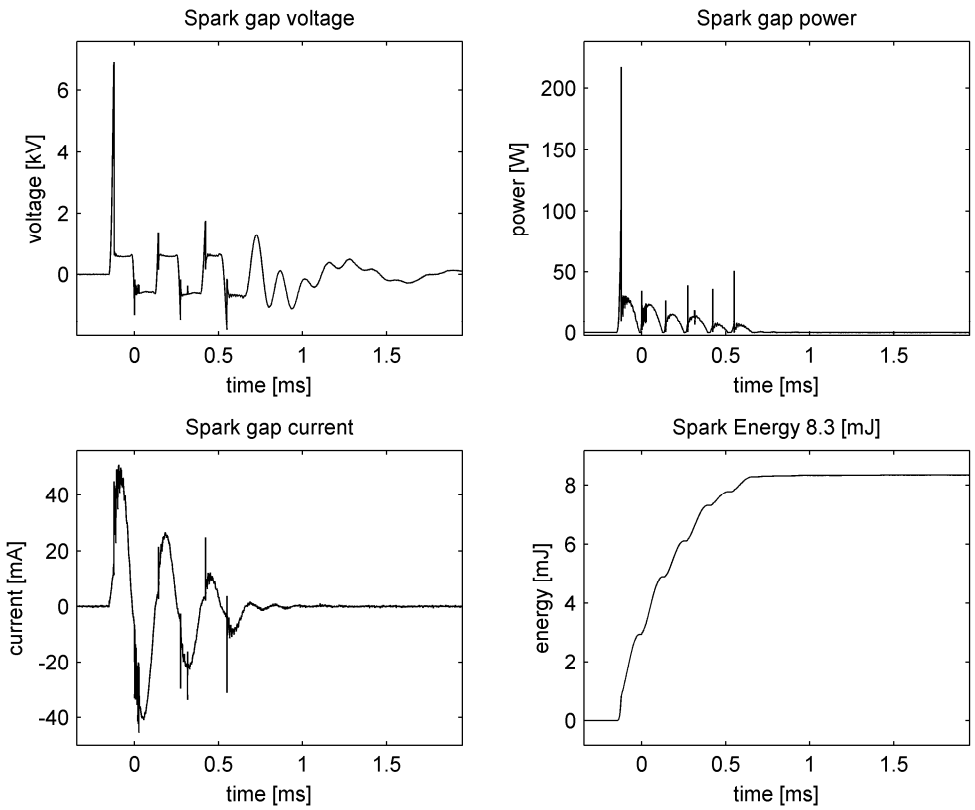

Fig. 63 Spark, successful ignition of 3.8% LPG by volume

Table 31 Test-13 data for 3.8% LPG

Pre Mix Temperature	70.8	ºF
Final Temperature	69.8	ºF
Barometric Pressure	14.06	PSIA
Initial Gauge Pressure	0.00	PSIG
Final Gauge Pressure	0.58	PSIG
Fuel to Air Ratio	0.039	
Mixture Composition	3.8	% by Vol.
Capacitor Value	1.487	µF
Capacitor Voltage	180	V
Capacitor Energy	24.1	mJ
Spark Energy	8.3	mJ
Trigger Count	1	

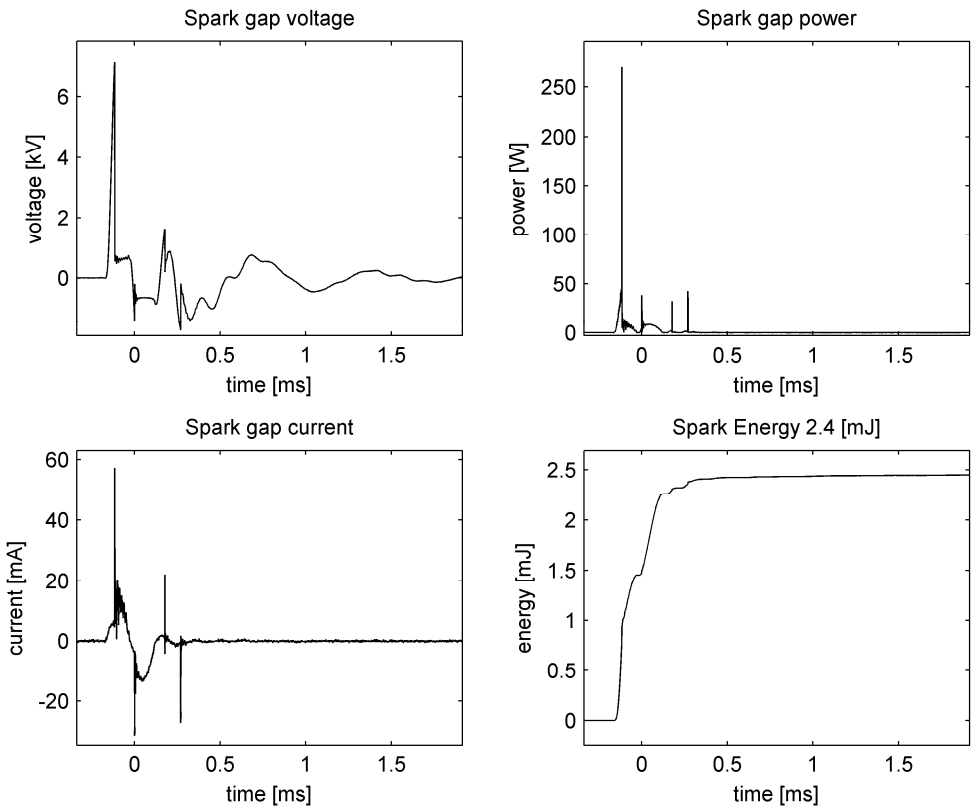

Fig. 64 Spark, successful ignition of 6.0% LPG by volume

Table 32 Test-14 data for 6.0% LPG

Pre Mix Temperature	71	ºF
Final Temperature	70.5	ºF
Barometric Pressure	14.06	PSIA
Initial Gauge Pressure	0.00	PSIG
Final Gauge Pressure	0.92	PSIG
Fuel to Air Ratio	0.064	
Mixture Composition	6.0	% by Vol.
Capacitor Value	1.487	µF
Capacitor Voltage	80	V
Capacitor Energy	4.8	mJ
Spark Energy	2.4	mJ
Trigger Count	1	

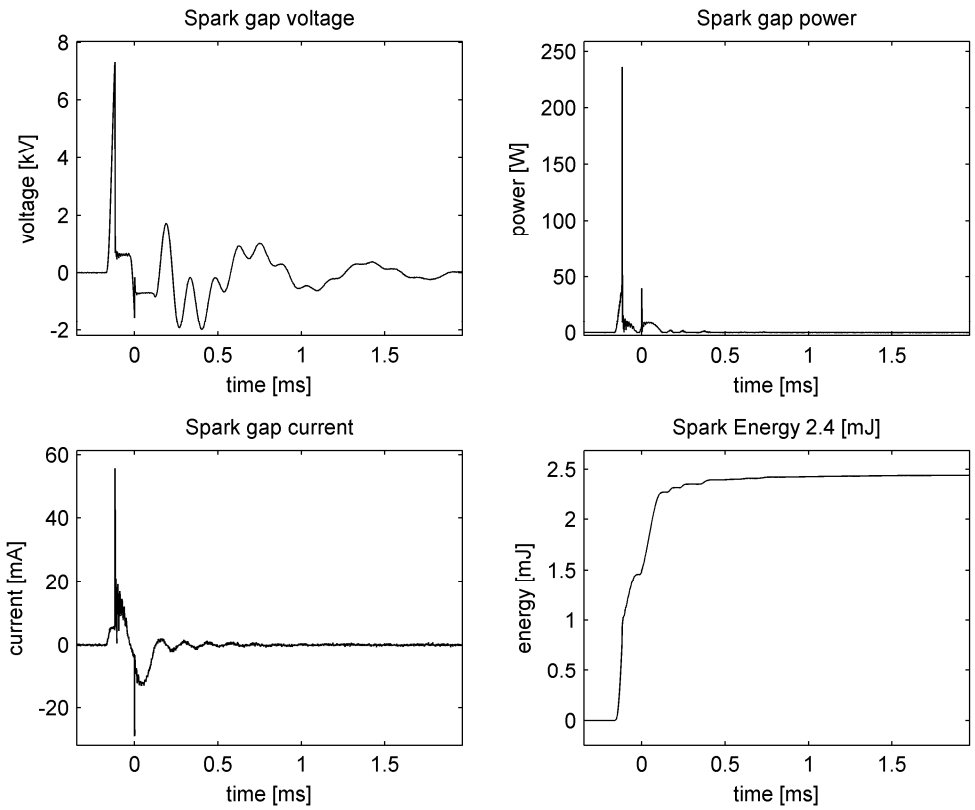

Fig. 65 Spark, successful ignition of 7.3% LPG by volume

Table 33 Test-15 data for 7.3% LPG

Pre Mix Temperature	72.3	ºF
Final Temperature	72.0	ºF
Barometric Pressure	14.05	PSIA
Initial Gauge Pressure	0.00	PSIG
Final Gauge Pressure	1.12	PSIG
Fuel to Air Ratio	0.078	
Mixture Composition	7.3	% by Vol.
Capacitor Value	1.487	µF
Capacitor Voltage	80	V
Capacitor Energy	4.8	mJ
Spark Energy	2.4	mJ
Trigger Count	2	

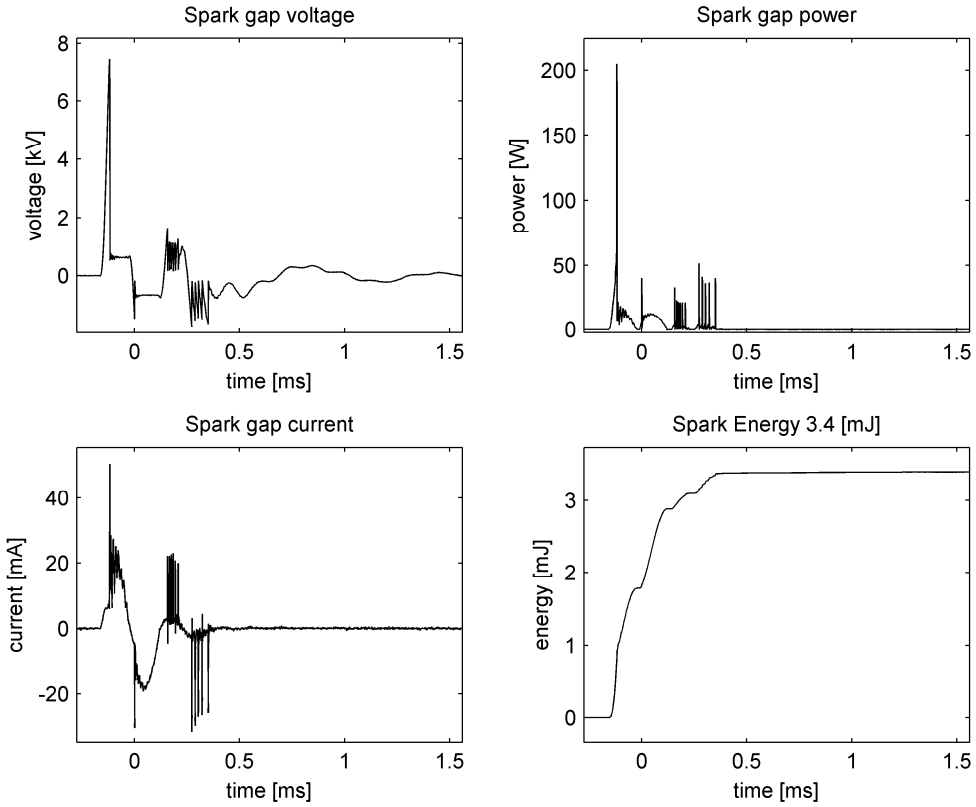

Fig. 66 Spark, successful ignition of 7.9% LPG by volume

Table 34 Test-16 data for 7.9% LPG

Pre Mix Temperature	72.6	ºF
Final Temperature	73.5	ºF
Barometric Pressure	14.04	PSIA
Initial Gauge Pressure	0.00	PSIG
Final Gauge Pressure	1.19	PSIG
Fuel to Air Ratio	0.086	
Mixture Composition	7.9	% by Vol.
Capacitor Value	1.487	µF
Capacitor Voltage	100	V
Capacitor Energy	7.4	mJ
Spark Energy	3.4	mJ
Trigger Count	1	

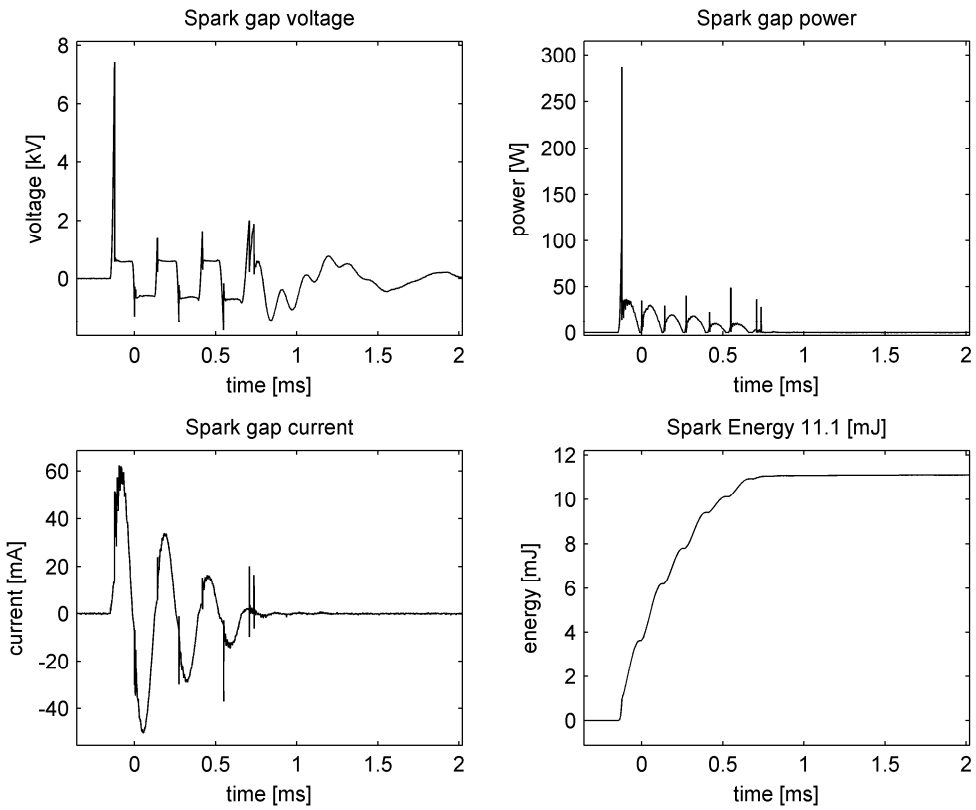

Fig. 67 Spark, successful ignition of 9.0% LPG by volume

Table 35 Test-17 data for 9.0% LPG

Pre Mix Temperature	72.3	ºF
Final Temperature	72.6	ºF
Barometric Pressure	14.05	PSIA
Initial Gauge Pressure	0.00	PSIG
Final Gauge Pressure	1.39	PSIG
Fuel to Air Ratio	0.099	
Mixture Composition	9.0	% by Vol.
Capacitor Value	1.487	µF
Capacitor Voltage	220	V
Capacitor Energy	36.0	mJ
Spark Energy	11.1	mJ
Trigger Count	5	

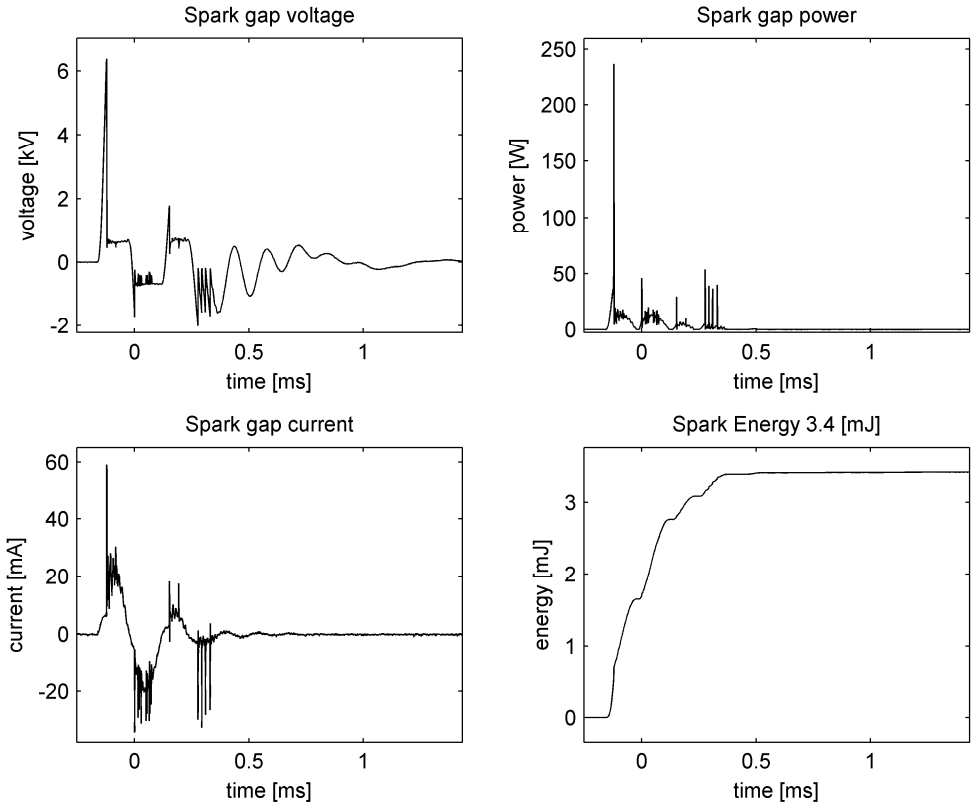

Fig. 68 Spark, successful ignition of 8.3% LPG by volume

Table 36 Test-18 data for 8.3% LPG

Pre Mix Temperature	72.3	ºF
Final Temperature	73.0	ºF
Barometric Pressure	14.04	PSIA
Initial Gauge Pressure	0.00	PSIG
Final Gauge Pressure	1.26	PSIG
Fuel to Air Ratio	0.090	
Mixture Composition	8.3	% by Vol.
Capacitor Value	1.487	µF
Capacitor Voltage	100	V
Capacitor Energy	7.4	mJ
Spark Energy	3.4	mJ
Trigger Count	1	

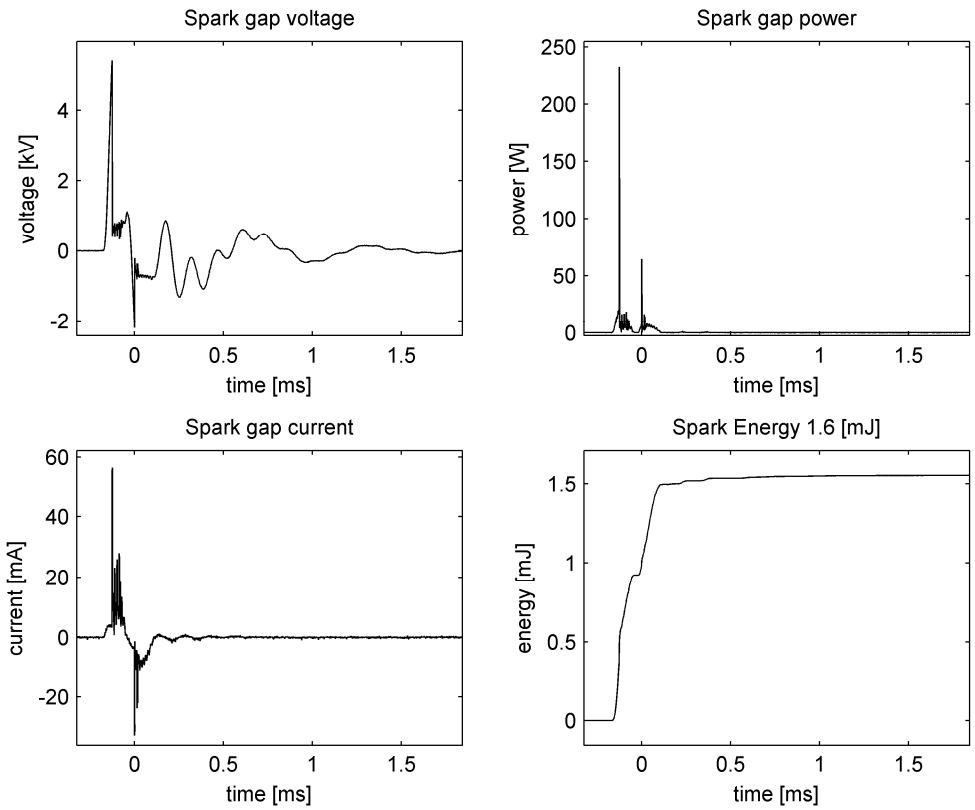

Fig. 69 Spark, successful ignition of 4.7% LPG by volume

Table 37 Test-19 data for 4.7% LPG

Pre Mix Temperature	72.7	ºF
Final Temperature	73.3	ºF
Barometric Pressure	14.04	PSIA
Initial Gauge Pressure	0.00	PSIG
Final Gauge Pressure	0.68	PSIG
Fuel to Air Ratio	0.049	
Mixture Composition	4.7	% by Vol.
Capacitor Value	1.487	μF
Capacitor Voltage	60	V
Capacitor Energy	2.7	mJ
Spark Energy	1.6	mJ
Trigger Count	1	

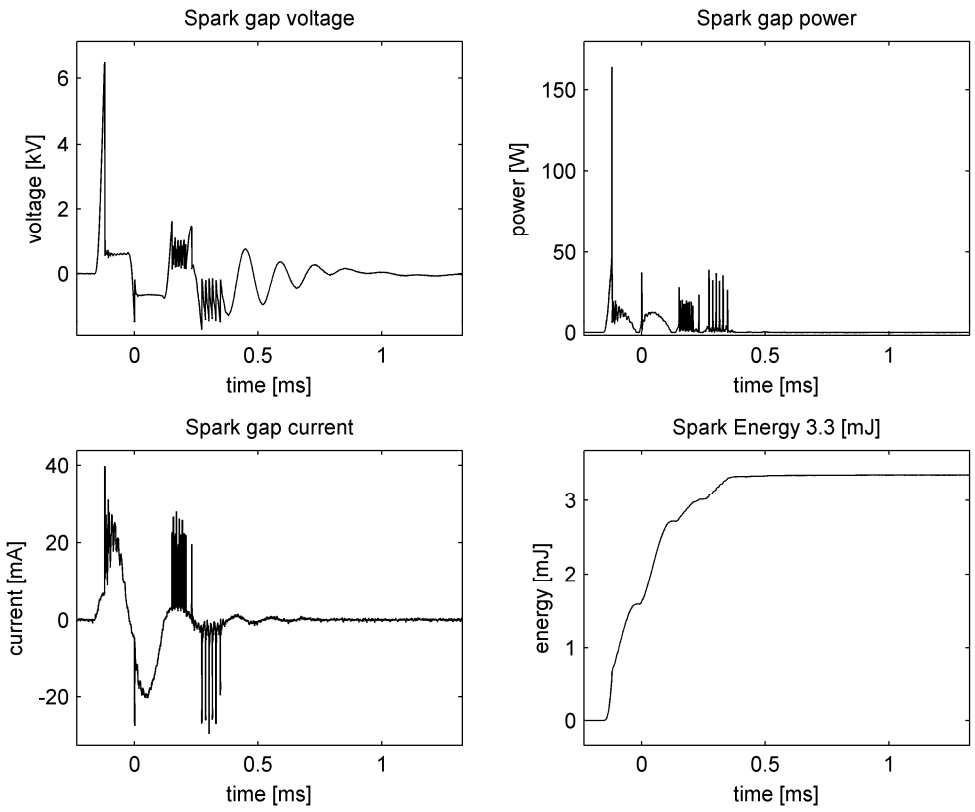

Fig. 70 Spark, successful ignition of 4.4% LPG by volume

Table 38 Test-20 data for 4.4% LPG

Pre Mix Temperature	71.6	ºF
Final Temperature	71.7	ºF
Barometric Pressure	14.03	PSIA
Initial Gauge Pressure	0.00	PSIG
Final Gauge Pressure	0.65	PSIG
Fuel to Air Ratio	0.046	
Mixture Composition	4.4	% by Vol.
Capacitor Value	1.487	µF
Capacitor Voltage	100	V
Capacitor Energy	7.4	mJ
Spark Energy	3.3	mJ
Trigger Count	1	

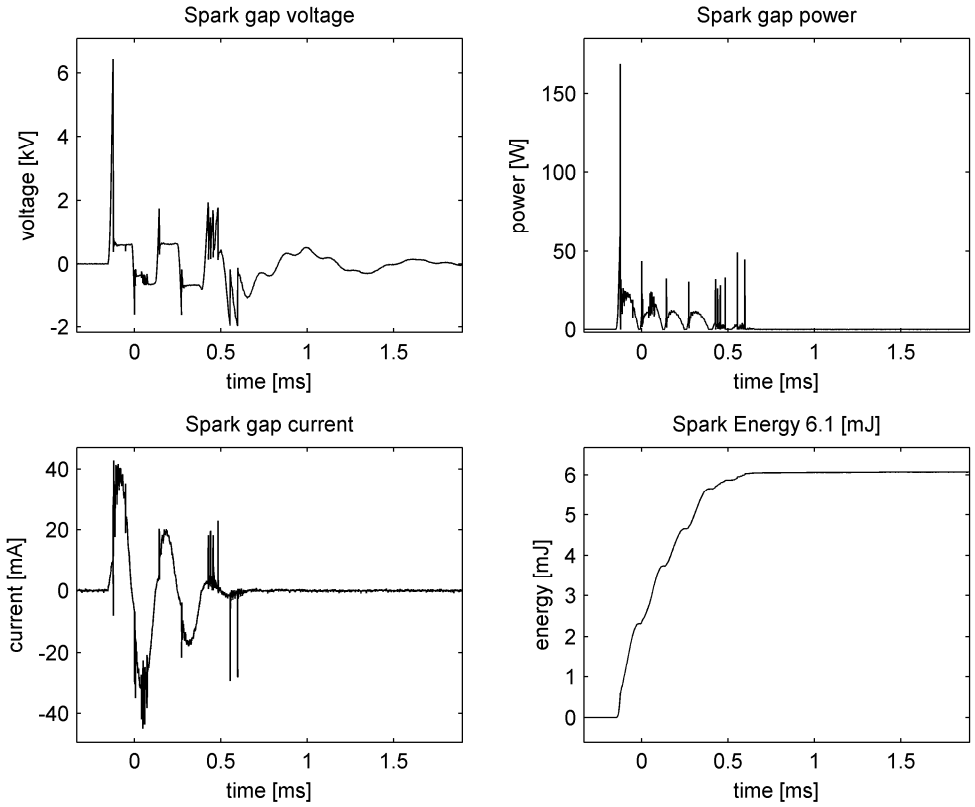

Fig. 71 Spark, successful ignition of 3.9% LPG by volume

Table 39 Test-21 data for 3.9% LPG

Pre Mix Temperature	73.8	ºF
Final Temperature	73.1	ºF
Barometric Pressure	14.03	PSIA
Initial Gauge Pressure	0.00	PSIG
Final Gauge Pressure	0.59	PSIG
Fuel to Air Ratio	0.040	
Mixture Composition	3.9	% by Vol.
Capacitor Value	1.487	µF
Capacitor Voltage	150	V
Capacitor Energy	16.7	mJ
Spark Energy	6.1	mJ
Trigger Count	10	

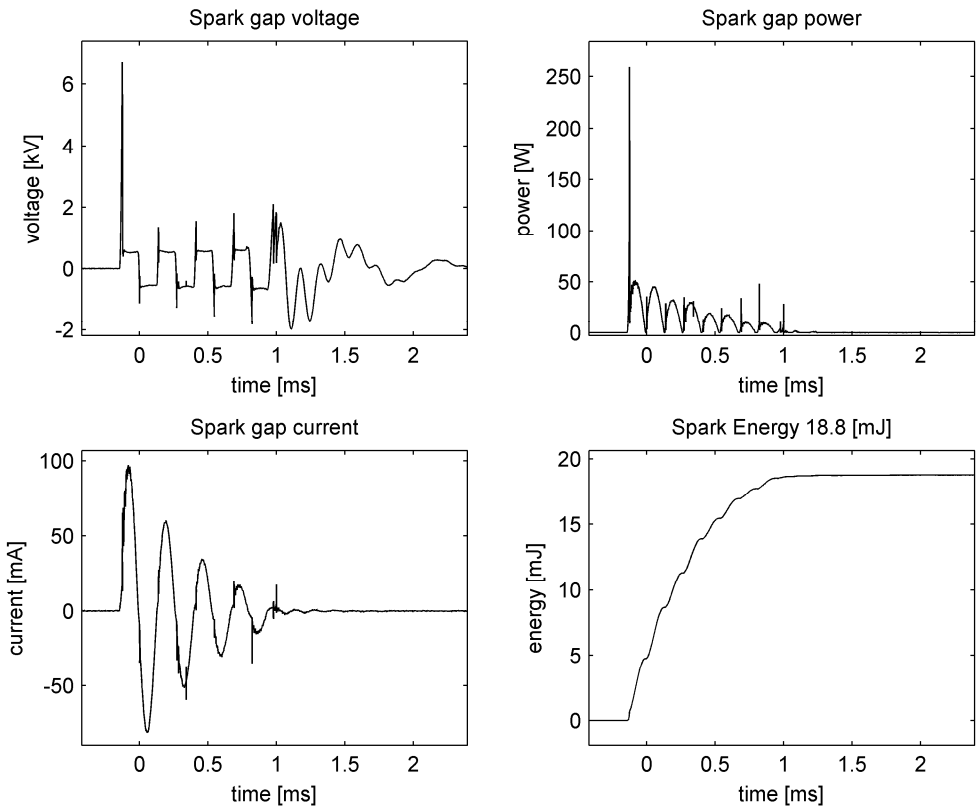

Fig. 72 Spark, successful ignition of 3.6% LPG by volume

Table 40 Test-22 data for 3.6% LPG

Pre Mix Temperature	74.4	ºF
Final Temperature	73.3	ºF
Barometric Pressure	14.03	PSIA
Initial Gauge Pressure	0.00	PSIG
Final Gauge Pressure	0.57	PSIG
Fuel to Air Ratio	0.038	
Mixture Composition	3.6	% by Vol.
Capacitor Value	1.487	µF
Capacitor Voltage	340	V
Capacitor Energy	85.9	mJ
Spark Energy	18.8	mJ
Trigger Count	2	

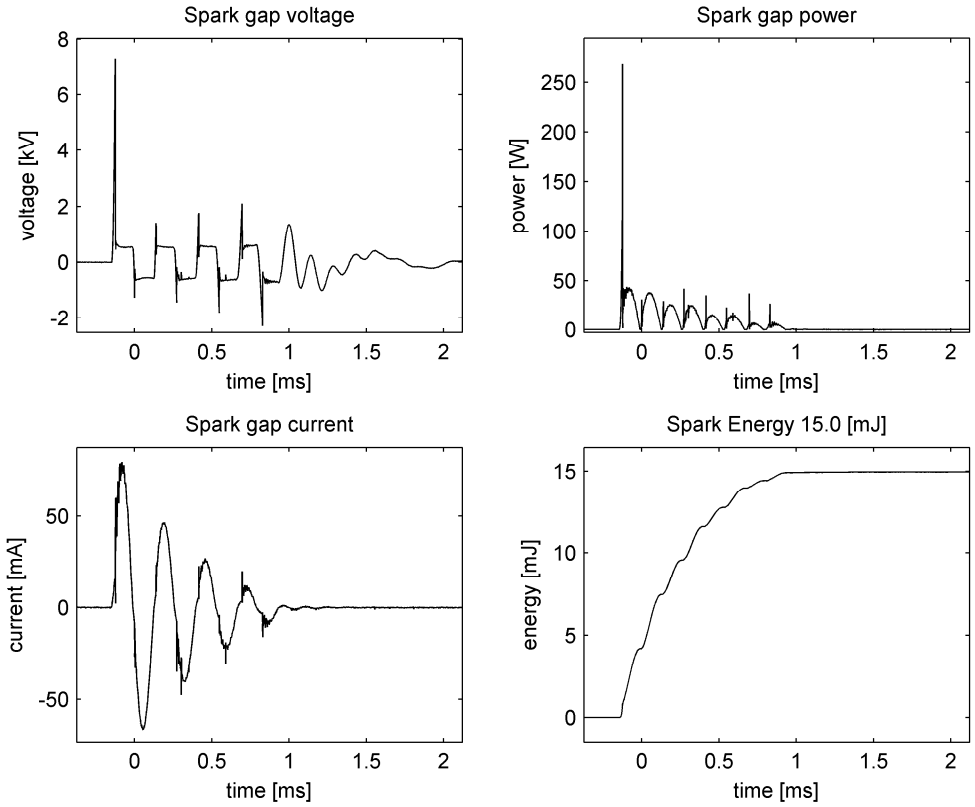

Fig. 73 Spark, successful ignition of 3.8% LPG by volume

Table 41 Test-23 data for 3.8% LPG

Pre Mix Temperature	74.4	ºF
Final Temperature	74.7	ºF
Barometric Pressure	14.02	PSIA
Initial Gauge Pressure	0.00	PSIG
Final Gauge Pressure	0.54	PSIG
Fuel to Air Ratio	0.039	
Mixture Composition	3.8	% by Vol.
Capacitor Value	1.487	µF
Capacitor Voltage	280	V
Capacitor Energy	58.3	mJ
Spark Energy	15.0	mJ
Trigger Count	3	

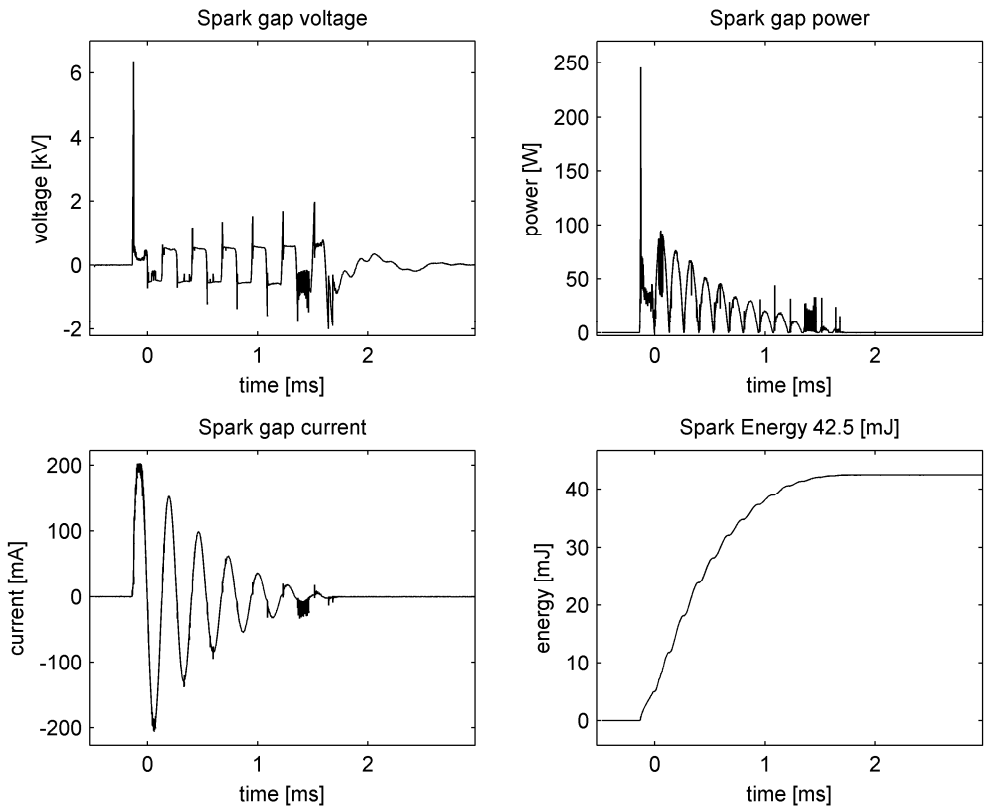

Fig. 74 Spark, unsuccessful attempt of 3.4% LPG by volume

Table 42 Test-24 data for 3.4% LPG

Pre Mix Temperature	75.2	ºF
Final Temperature	75.3	ºF
Barometric Pressure	14.03	PSIA
Initial Gauge Pressure	0.00	PSIG
Final Gauge Pressure	0.50	PSIG
Fuel to Air Ratio	0.036	
Mixture Composition	3.4	% by Vol.
Capacitor Value	1.487	µF
Capacitor Voltage	840	V
Capacitor Energy	524.6	mJ
Spark Energy	42.5	mJ
Trigger Count	10	

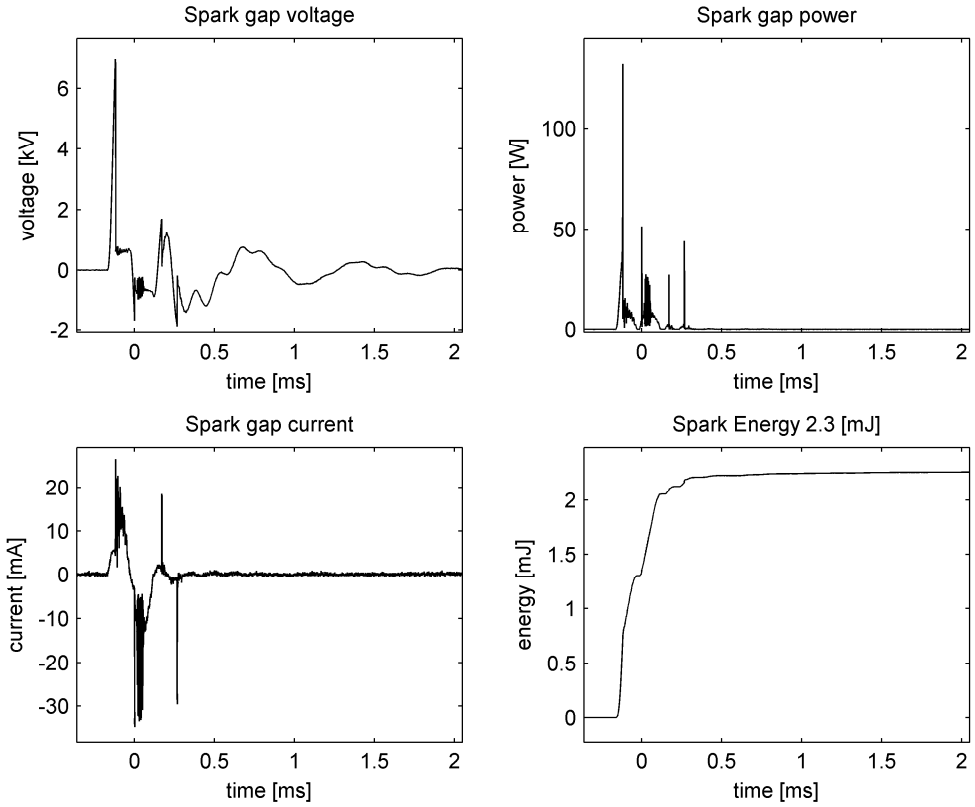

Fig. 75 Spark, successful ignition of 4.2% LPG by volume

Table 43 Test-25 data for 4.2% LPG

Pre Mix Temperature	71.6	ºF
Final Temperature	71.3	ºF
Barometric Pressure	14.06	PSIA
Initial Gauge Pressure	0.00	PSIG
Final Gauge Pressure	0.63	PSIG
Fuel to Air Ratio	0.044	
Mixture Composition	4.2	% by Vol.
Capacitor Value	1.487	µF
Capacitor Voltage	80	V
Capacitor Energy	4.8	mJ
Spark Energy	2.3	mJ
Trigger Count	2	

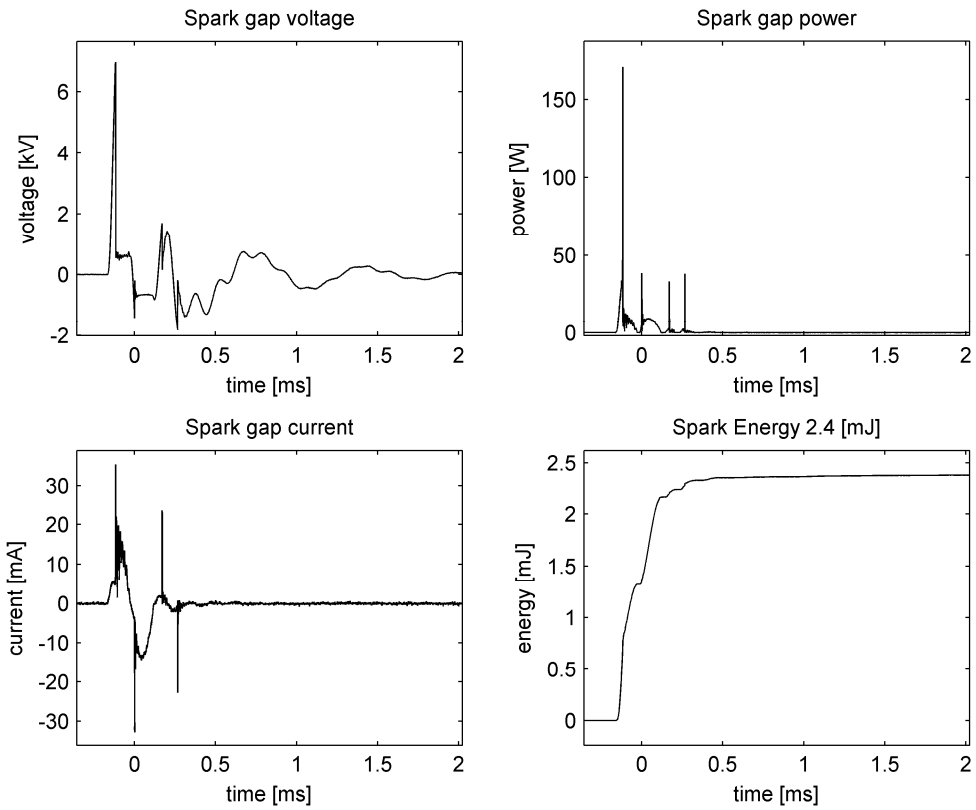

Fig. 76 Spark, successful ignition of 5.4% LPG by volume

Table 44 Test-26 data for 5.4% LPG

Pre Mix Temperature	72.2	ºF
Final Temperature	71.7	ºF
Barometric Pressure	14.05	PSIA
Initial Gauge Pressure	0.00	PSIG
Final Gauge Pressure	0.83	PSIG
Fuel to Air Ratio	0.058	
Mixture Composition	5.4	% by Vol.
Capacitor Value	1.487	µF
Capacitor Voltage	80	V
Capacitor Energy	4.8	mJ
Spark Energy	2.4	mJ
Trigger Count	1	

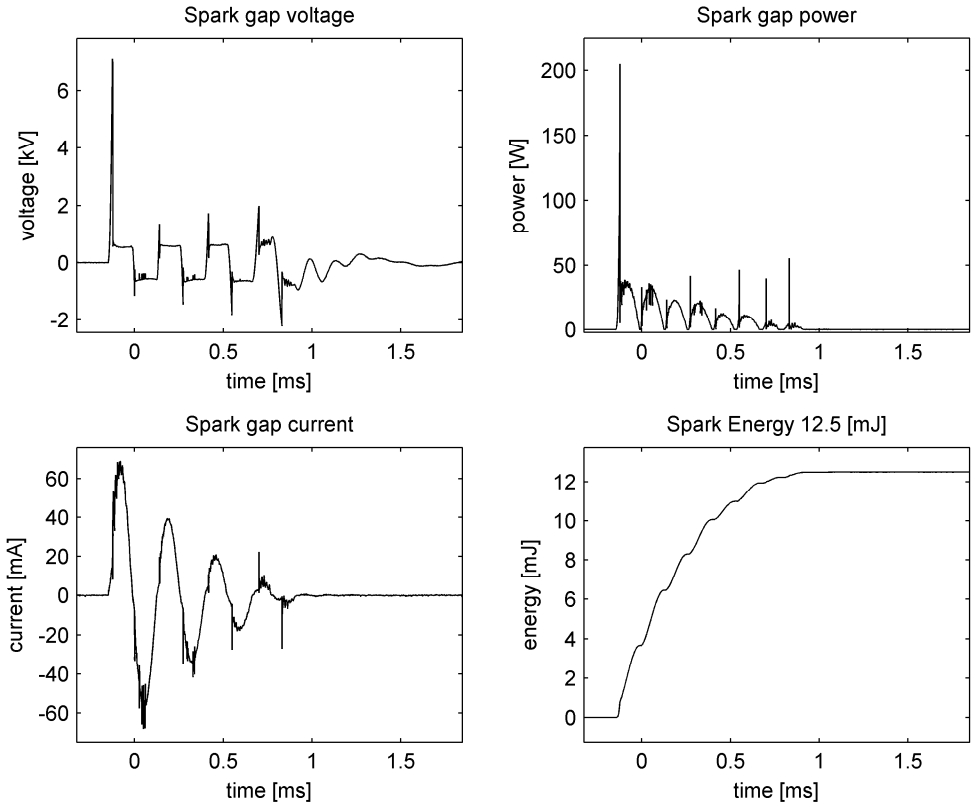

Fig. 77 Spark, successful ignition of 3.7% LPG by volume

Table 45 Test-27 data for 3.7% LPG

Pre Mix Temperature	73.5	ºF
Final Temperature	73.2	ºF
Barometric Pressure	14.05	PSIA
Initial Gauge Pressure	0.00	PSIG
Final Gauge Pressure	0.55	PSIG
Fuel to Air Ratio	0.038	
Mixture Composition	3.7	% by Vol.
Capacitor Value	1.487	µF
Capacitor Voltage	240	V
Capacitor Energy	42.8	mJ
Spark Energy	12.5	mJ
Trigger Count	3	

A.3 RESONATOR QUALITY FACTOR MEASUREMENT

Once assembled the quality factor of the test QWCCR was determined through measurement on a Hewlett Packard™ HP8753D vector network analyzer. The complex reflection coefficient data, S11, was captured and analyzed. A resonance should form a perfect circle on a Smith chart plot, as can be seen in Fig. 78 and Fig. 79. The half power points can be found at a VSWR of 5.83. As the circles on the Smith chart do not encompass the center, the cavity was slightly under coupled. The Q_0 was found from the $VSWR$ at the resonance frequency, f_{res}, and the half power bandwidth, $HPBW$, with

$$Q_0 = \left(1 + \frac{1}{VSWR_{res}}\right)\frac{f_{res}}{HPBW} \tag{64}$$

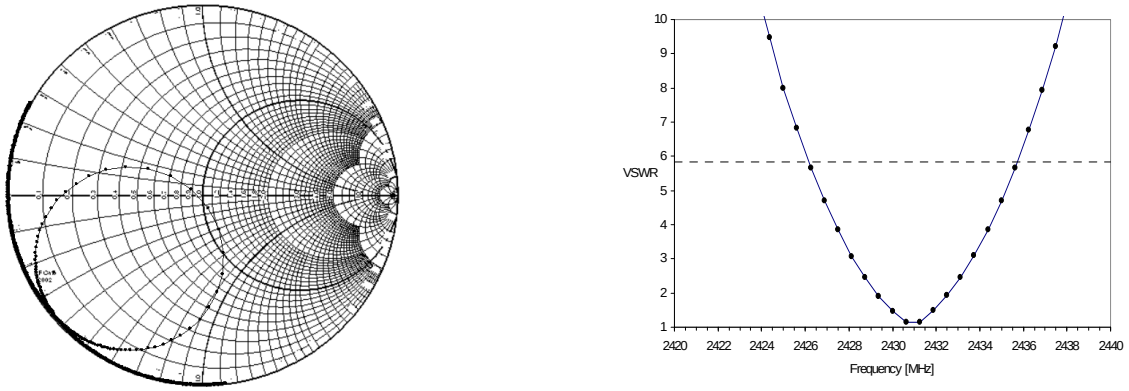

Fig. 78 Impedance data for implemented QWCCR design prior to ignition testing; Q_0.=515

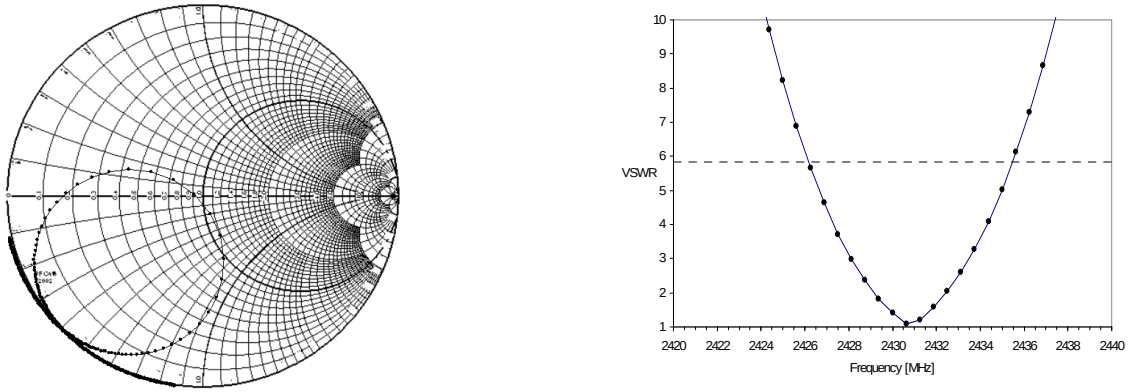

Fig. 79 Impedance data for implemented QWCCR design after ignition testing; Q_0. = 513

A.4 HIGH BANDWIDTH MICROWAVE DETECTOR

The cellular and wireless industry has lead to the development of temperature compensated Schottky diode based detectors on a chip. One such chip is the Linear Technologies LTC5535.

Table 46 LTC5535 detector specifications

Frequency Range	600 MHz – 7 GHz
Supply Voltage	2.7 V to 5.5 V
Sensitivity	500 mV/mW @ -20 dBm
Input Power Range	-32 dBm to 10 dBm
Vout BW (2 k+33 pF load)	12 MHz

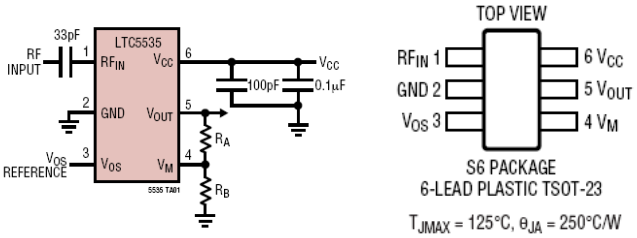

Fig. 80 Basic LTC5535 information

Samples of this chip were obtained from Linear Technologies, and assembled into a microwave detector boards. The art work for the layout of the boards assembled is given below in Fig. 82. Various terminating resistor combinations were experimented. The best VSWR on the RF input was achieved with a 33 Ohm resistor. A schematic of the circuit is given below in Fig. 81. The assembled boards were tested and showed good rise times in response to microwave pulses. Calibration with different microwave input power levels resulted in the calibration curve shown in Fig. 83. As is to be expected for a diode detector, these are quadratic. The detectors response to microwave pulses was investigated with a drain pulsed amplifier. The drain was pulse at 1 MHz. The response of the detector is shown in Fig. 84. There is about an 80 ns delay between the modulation input and the sensor's response.

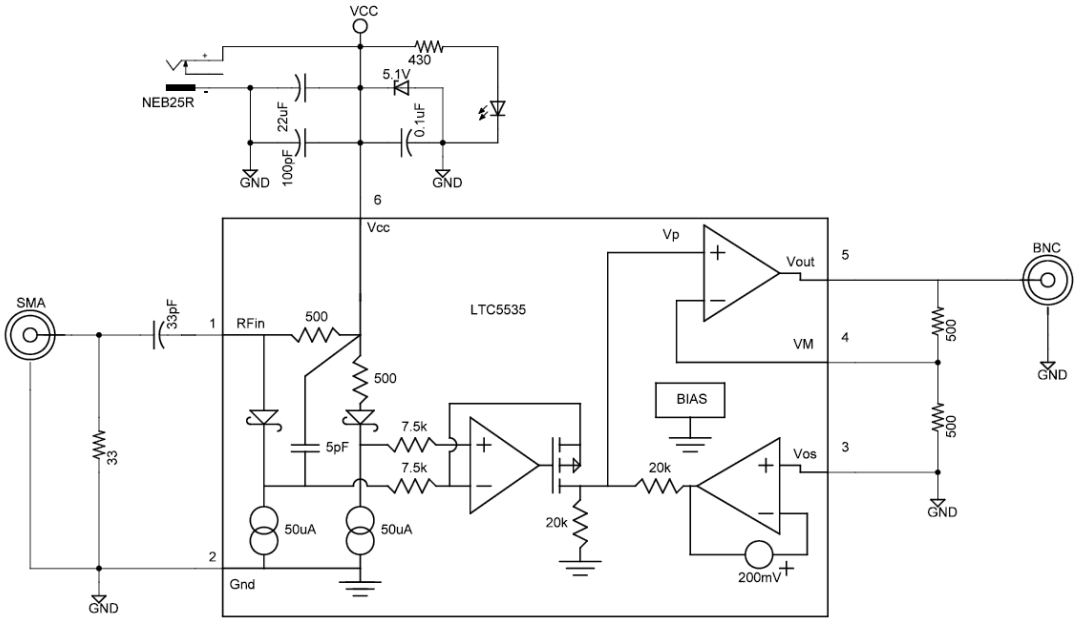

Fig. 81 LTC5535 detector board schematic

.

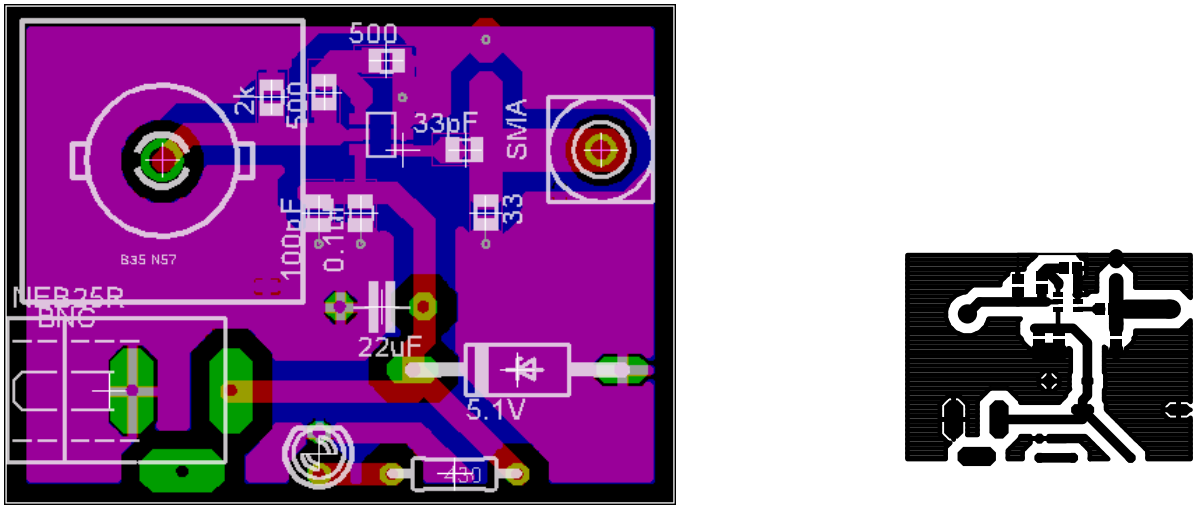

Fig. 82 LTC5535 detector PCB board artwork

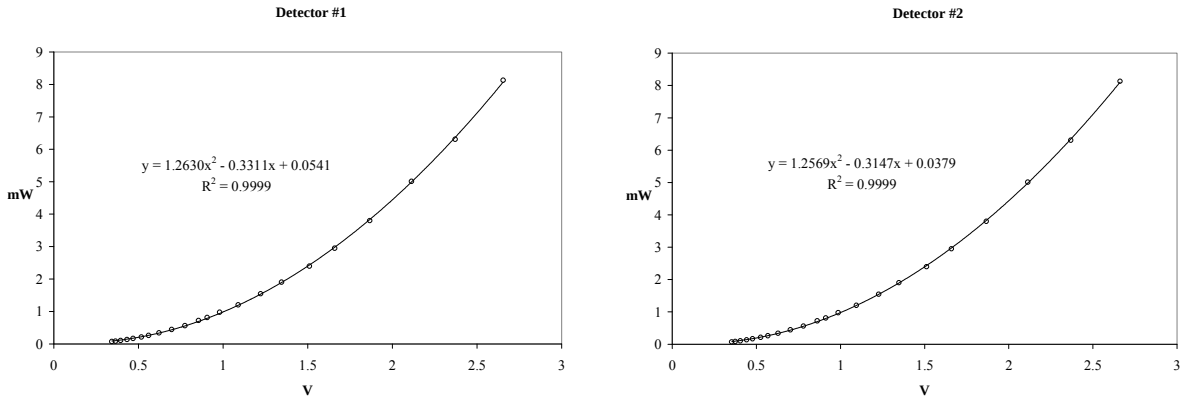

Fig. 83 LTC5535 detector response curve at 2430.73 MHz

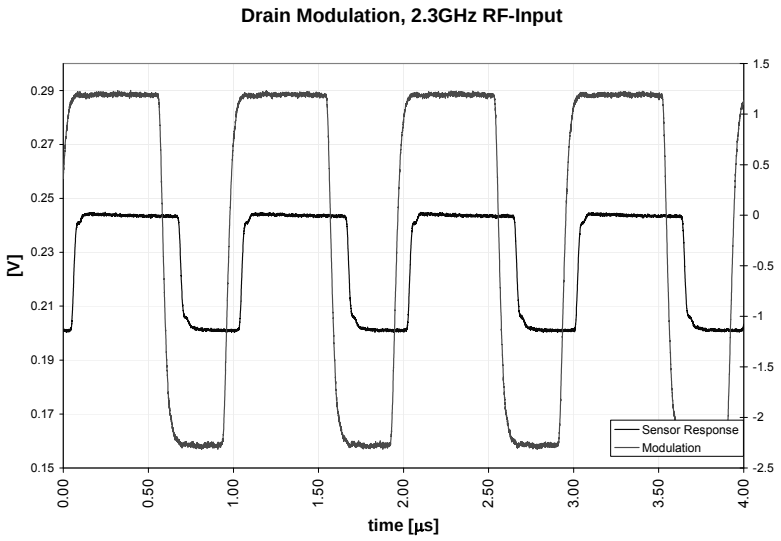

Fig. 84 LTC5535 response at 2.3 GHz to a 1 MHz pulse rate

A.5 PRESSURE SENSORS

Shown below are the pressure sensors used and their calibration curves.

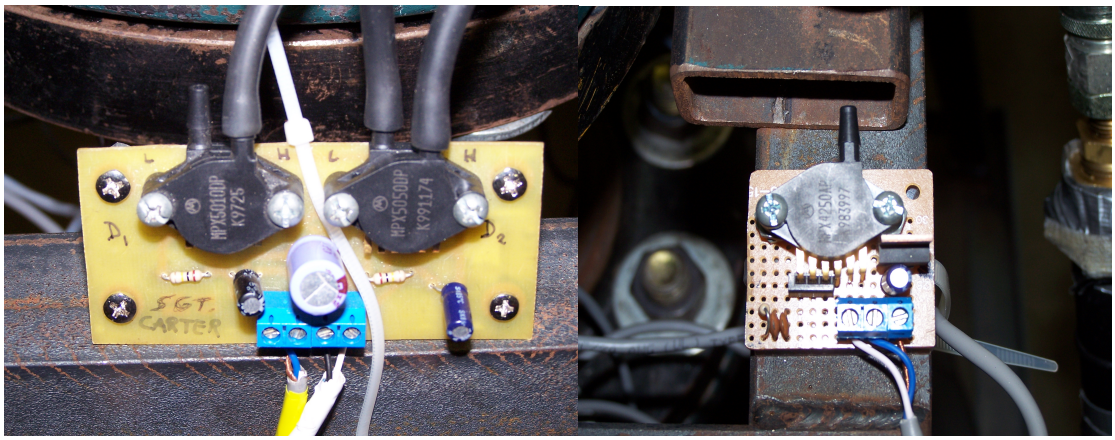

Fig. 85 Pressure sensors (left: MPX5010DP; right MPX4250AP)

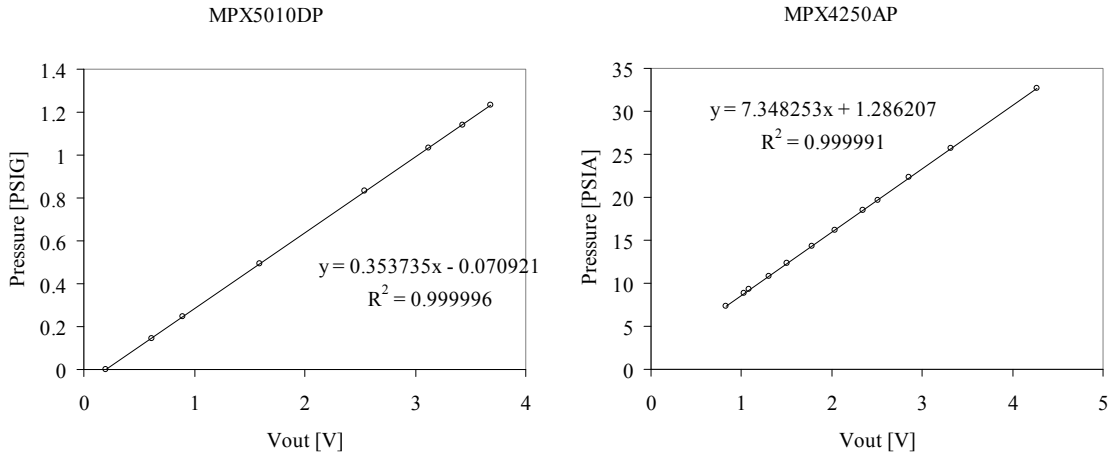

Fig. 86 Pressure sensors calibration curves (left: MPX5010DP; right MPX4250AP)

A.6 FUEL PROPERTIES

A commercial LPG cylinder from AmeriGas™ Propane L.P. was used. The properties of this fuel according to the MSDS data sheet are as follows:

Table 47 Fuel composition and properties

Propane	87.5-100	%
Ethane	0-7	%
Propylene	0-5	%
Butanes	0-2.5	%
Ethyl Mercapant (odorant)	0-50	ppm
Flash Point Temperature	-156	ºF
Autoignition Temperature	842	ºF
Lower Flammability Limit	2.15	% by Vol.
Upper Flammability Limit	9.6	% by Vol.

A.7 IGNITION COIL EFFICIENCY MEASUREMENTS

Note that this data was taken with a smaller gap spark plug than used in the ignition test, but all other components and settings of the ignition system were identical.

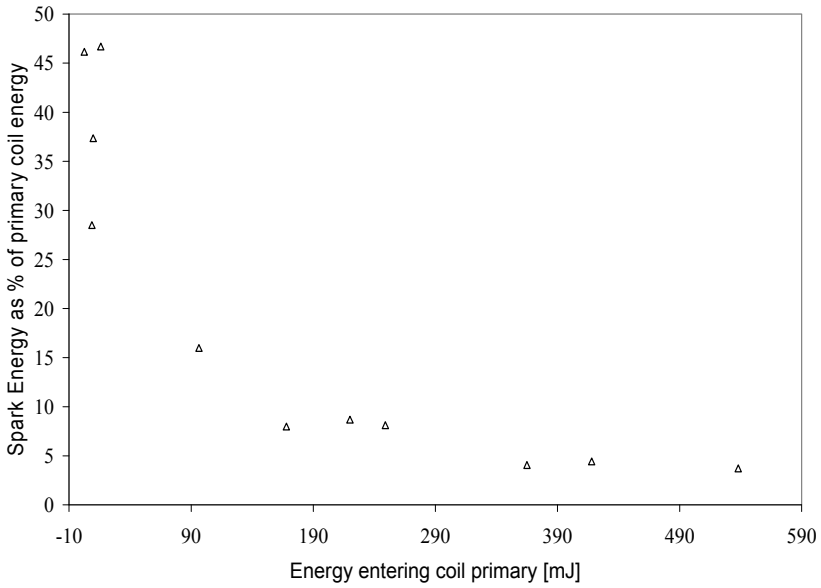

Fig. 87 Ignition coil primary to spark energy transfer efficiency

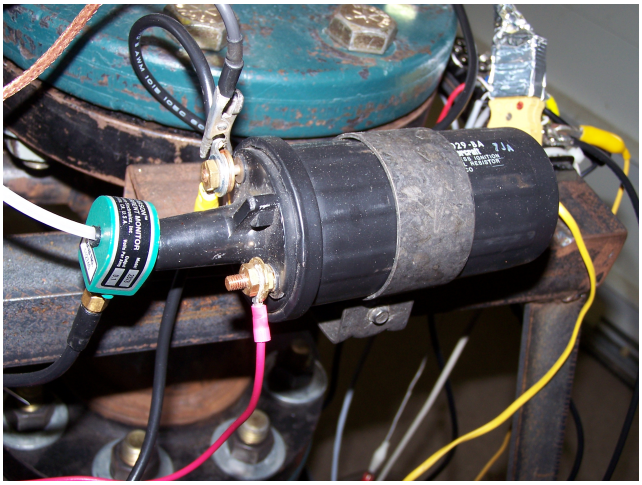

Fig. 88 Ignition coil primary used in experiment

A.8 COMBUSTION VESSEL

Shown in Fig. 89 is a photograph of the instrumented combustion vessel. Dimensions of the vessel are given in Fig. 90.

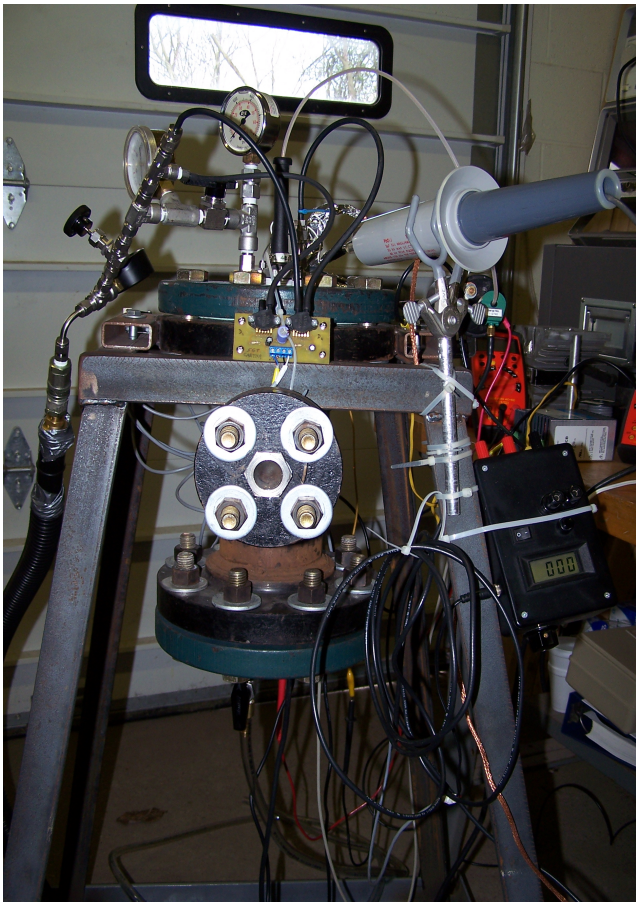

Fig. 89 Instrumented combustion vessel

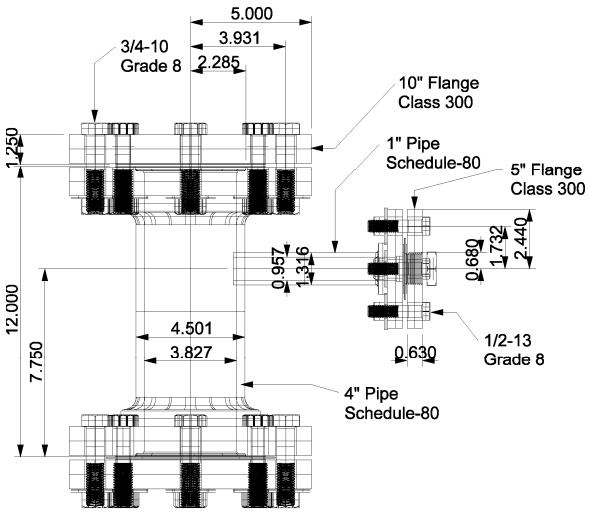

Fig. 90 Combustion vessel dimensions